DIRECT RAY TRACING FOR

LOW ENERGY ELECTRON MICROSCOPY

DING YU

NATIONAL UNIVERSITY OF SINGAPORE

2007

DIRECT RAY TRACING FOR

LOW ENERGY ELECTRON MICROSCOPY

DING YU
(B.Eng.(Hons.), Nanyang Technological University)

A THESIS SUBMITTED

FOR THE DEGREE OF MASTER OF ENGINEERING

DEPARTMENT OF ELECTRICAL & COMPUTER ENGINEERING

NATIONAL UNIVERSITY OF SINGAPORE

2007

Acknowledgements

First of all I would like to express my heartfelt gratitude to my M.Eng supervisor, Assoc. Prof. Anjam Khursheed. He is not only a great scientist with deep vision but also and most importantly a kind person. Without his enthusiasm, inspiration, patience, great efforts and efficient guidance, this work could not be possible.

I also would like thank Dr. Mans JB Osterberg, Mr. Luo Tao and Dr. Karuppiah Nelliyan and all the other people in A/Prof. Khursheed's Bioimaging and Optics group for their kind help, sharing knowledge and research experience with me throughout the period of my master's study. I am also grateful to all the staffs and students in CICFAR for their support.

Most importantly, I would like to thank my parents and my girl friend for their encouragement and love.

Table of contents

List of figures

List of tables

Abstract

This thesis is concerned with the accurate simulation of electron trajectory paths in electron optics. In particular, it investigates the use of a direct ray tracing method that employs the Cash-Karp 5^{th} order Runge-Kutta technique in combination with a Fourier series fit to axial magnetic/electric field distributions. The direct ray tracing method was used successively to improve the design of several electron optical systems. It was used to calculate the aberration probe size of a low voltage scanning electron microscope mixed field objective lens, for which conventional methods of paraxial-perturbation breakdown. It was also used to plot through-the-lens scattered secondary electrons in such systems, simulating their radial current distribution at a rotationally symmetric detector plane. Lastly, the direct ray tracing method was used to redesign the drift-tube in a dynamic chromatic correction scheme for Photoemission Electron Microscopy (PEEM). The performance of this system was simulated in detail, and compared with the alternative aberration correction method based upon the use of a tetrode mirror.

Keywords: Direct ray tracing; Low voltage SEM; Electron spectroscopy; Time-of-flight emission microscope; Dynamic chromatic aberration correction; Drift tube

CHAPTER 1

Introduction

1.1 Low energy electron microscopy and mixed field objective lens

Low voltage electron microscopy is a popular technique that has applications in many areas of research, ranging from microelectronics to biology. Although conventional lenses perform poorly at low landing energies (< 1 keV), the use of immersion lenses is now widespread in low-voltage scanning electron microscopy (LVSEM) [1, 2] as a means of obtaining high image resolution. Amongst the different types of immersion objective lenses possible, the combined electric retarding field and magnetic immersion action (mixed field objective lens) is predicted to give the highest image resolution without aberration correction [3].

This thesis aims to carry out accurate direct ray tracing of electron trajectory paths in some applications where mixed field objective lenses are used, in order to better understand their optical and spectral properties.

1.2 Direct Ray Tracing

An accurate direct ray tracing program is crucial for producing reliable simulation results. The standard method of paraxial trajectory perturbation using 4^{th} order Runge Kutta method with fixed step size in distance is not reliable when tracing electron trajectory paths in fast changing fields, e.g. mixed field objective lens, due to its assumption of the electrons being near the optical axis and their angles being relatively small. Direct ray tracing is much more general, it can simulate electrons that go far off-axis, however, it must be performed accurately. The method to be used in this thesis is the 5^{th} order Runge Kutta with Cash Karp coefficients to integrate the equations of motion, combined with a Fourier fit to axial field distributions to derive smooth electric/magnetic field values. The 5^{th} order Runge Kutta with Cash Karp coefficients tiptoes through regions of high field intensity, automatically adjusting the step size in time accordingly. The Fourier-fit method to the axial field distribution ensures that smooth higher derivatives can be calculated in a series expansion method in order to obtain off-axis field values [4]. These methods are expected to provide more accurate ray tracing for both on-axis and off-axis simulation, and with higher efficiency. Other important information, like time of flight, can also be extracted. In this work, the simulation program was written in FORTRAN 77, and run on a personal computer with Pentium IV 1.6G processor and 512M memory.

1.3 Low voltage scanning electron microscopy

Direct ray tracing is needed for very low primary beam landing energies, down to say less than 100 eV, in these cases, conventional simulation methods break down. Also, the trajectory paths of scattered electrons back through a mixed field lens need to be plotted accurately, in order to understand how to obtain energy spectral information [5]. So far, little work has been done to adequately understand secondary image and spectrum formation in mixed field immersion lenses for low energy electron microscopy system.

1.4 Time of flight electron emission microscope and drift tube design

All forms of electron emission microscopy involve irradiating a specimen with energy, thereby creating secondary electrons that can be used to provide a topographic image of the specimen surface. When UV or X-ray photons are used as the source, the technique is known as PEEM or XPEEM [6], which is rapidly becoming an important technique in the study of chemical properties of materials. However, several problems prevent it from operating in the nanometer range. The dominant one is chromatic aberration. This is because the energies of the secondary photoelectrons excited by X-rays at the sample can range from several to tens of eV. Over the last four years, proposals for time-of-flight electron emission microscopes (TOFEEMs) have been made, both with and without methods to dynamically correct

for chromatic aberration [7-9]. Correction of aberrations in time is an important alternative to the more widely discussed tetrode mirror method [10, 11]. This is because the tetrode mirror method has a relatively complicated column design, where its photoelectrons are designed to trace trajectory paths around a multiply curved axis, requiring the use of special alignment strategies for its beam separator [12]. The TOFEEM column in comparison, is relatively simple, it has a single straight electron optical axis where photoelectrons are successively focused and magnified using standard projection principles.

In this thesis, the TOFEEM proposal will be simulated through accurate ray tracing. The degree to which chromatic aberration can be corrected will be examined in detail, and the expected improvement in image resolution as a function of percentage transmission will be calculated. Several drift-tube designs in the TOFEEM column will be investigated, in order to optimize its performance.

CHAPTER 2

Accurate trajectory plotting

2.1 Cash Karp Runge-Kutta

The Runge-Kutta method is one of the most important algorithms to solve initial value ordinary differential equations numerically. In the context of direct ray tracing of charged particles in electrostatic and magnetic fields, the electron's or ion's motion follows Newton-Lorentz law:

$$m\mathbf{a} = q(\mathbf{E} + \mathbf{v} \times \mathbf{B}) \tag{2.1}$$

where m is the particle's mass, q is particle's charge, **v** is the particle's velocity, **E** is the electrostatic field, **B** is the magnetic flux density, and $\mathbf{a} = \frac{d\mathbf{v}}{dt}$ is the resulting acceleration of the particle. To solve this equation numerically, in the non-relativistic 3D case, it is expressed as six first-order equations, the dependent variables being the particle's coordinates (x, y, z) and velocity components (v_x, v_y, v_z):

$$\begin{aligned} \frac{dx}{dt} &= v_x, \\ \frac{dv_x}{dt} &= \frac{q}{m}\left(E_x + v_y B_z - v_z B_y\right), \end{aligned} \tag{2.2a}$$

$$\frac{dy}{dt} = v_y,$$
$$\frac{dv_y}{dt} = \frac{q}{m}\left(E_y + v_z B_x - v_x B_z\right), \qquad (2.2b)$$

$$\frac{dz}{dt} = v_z,$$
$$\frac{dv_z}{dt} = \frac{q}{m}\left(E_z + v_x B_y - v_y B_x\right) \qquad (2.2c)$$

where the electric field components (E_x, E_y, E_z).and magnetic flux density components (B_x, B_y, B_z) at any required point (x, y, z) are obtained from formulae for the lens fields, which will be discussed in the next section. Standard fourth-order Runge-Kutta formula, with fixed step size, is the simplest way to solve the above equations [13], however, it has significant limitations. In particular, it is unsuitable where there are sharp changes either in field values or kinetic energy of the charged particle. Fifth-order Runge-Kutta formula, with Cash-Karp parameters [14] allows for fine steps in regions where the field has abrupt variations, while automatically increasing the step size by tens or even hundreds of times for regions where the field changes linearly or smoothly. These features lead to both higher accuracy and better efficiency. The algorithm for solving a differential equation of the form $dy/dt = f(t,y)$, starts by calculating the constants k_1 to k_6 as follows.

$$\begin{aligned} k_1 &= hf\left(t_n, y_n\right) \\ k_2 &= hf\left(t_n + a_2 h, y_n + b_{21} k_1\right) \\ &\cdots \\ k_6 &= hf\left(t_n + a_6 h, y_n + b_{61} k_1 + \ldots + b_{65} k_5\right) \end{aligned} \qquad (2.3)$$

where h is the time step, a_2-a_6, b_{21}-b_{65} are constants. Then the value of y at time t_{n+1} is computed with the fifth-order formula (with a truncation error proportional to h^6):

$$y_{n+1} = y_n + c_1 k_1 + c_2 k_2 + c_3 k_3 + c_4 k_4 + c_5 k_5 + c_6 k_6 + O\left(h^6\right) \tag{2.4}$$

where c_1-c_6 are constants. And also with the embedded fourth-order formula (with a truncation error proportional to h^5):

$$y^*_{n+1} = y_n + c^*_1 k_1 + c^*_2 k_2 + c^*_3 k_3 + c^*_4 k_4 + c^*_5 k_5 + c^*_6 k_6 + O\left(h^5\right) \tag{2.5}$$

where c_1^*-c_6^* are constants. An estimate of the local truncation error Δ, which can be used to rescale the step size is given by,

$$\Delta = y_{n+1} - y^*_{n+1} = \sum_{i=1}^{6} \left(c_i - c^*_i\right) k_i \tag{2.6}$$

The particular values of a_i, b_{ij}, c_i, and c_i^* in the above formulae, which can give favorably low values of the truncation error, were originally derived by Cash and Karp [14] as shown in Table 2.1.

i	a_i	b_{ij}					c_i	c_i^*
1							$\frac{37}{378}$	$\frac{2825}{27648}$
2	$\frac{1}{5}$	$\frac{1}{5}$					0	0
3	$\frac{3}{10}$	$\frac{3}{40}$	$\frac{9}{40}$				$\frac{250}{621}$	$\frac{18575}{48384}$
4	$\frac{3}{5}$	$\frac{3}{10}$	$-\frac{9}{10}$	$\frac{6}{5}$			$\frac{125}{594}$	$\frac{13525}{55296}$
5	1	$-\frac{11}{54}$	$\frac{5}{2}$	$-\frac{70}{27}$	$\frac{35}{27}$		0	$\frac{277}{14336}$
6	$\frac{7}{8}$	$\frac{1631}{55296}$	$\frac{175}{512}$	$\frac{575}{13824}$	$\frac{44275}{110592}$	$\frac{253}{4096}$	$\frac{512}{1771}$	$\frac{1}{4}$
j =		1	2	3	4	5		

Table 2.1: Cash-Karp Parameters for Embedded 5th order Runga-Kutta Method

Let us denote Δ_0 as the desired accuracy. If we take a step h_1, we find it produces an error Δ_1. Press et al [15] found a reliable way to determine the step h_0 that gives a value close to truncation error Δ_0 by

$$h_0 = \begin{cases} Sh_1 \left| \frac{\Delta_0}{\Delta_1} \right|^{0.20} & \Delta_0 \geq \Delta_1 \\ Sh_1 \left| \frac{\Delta_0}{\Delta_1} \right|^{0.25} & \Delta_0 < \Delta_1 \end{cases} \qquad (2.7)$$

where S is a safety factor fraction. The equation (2.7) works in two ways: if Δ_1 is larger than Δ_0 in magnitude, the equation tells how much to decrease the step size when we retry the present step. If Δ_1 is equal or smaller than Δ_0, on the other hand, then the equation tells how much we can safely increase the step size for the next trajectory step. Because estimates of the error are not exact, but only accurate to the leading order in *h*, a safety factor *S*, which is a few percent smaller than unity (like 0.9), is used.

Use of an appropriate Δ_0 for a given desired accuracy is a subtle question, and it depends on exactly what the application is [15]. The conventional way of doing it is to take a fractional accuracy (like one part in 10^6) on the values of *y* or more stringently on their increments at each step, which is *dy/dt* in our case. But the author found that fractional accuracy could not be adopted for our direct ray tracing program. For direct ray tracing in charged particle optics, nanometer or even sub-nanometer accuracy is required. The fractional accuracy approach therefore is too inaccurate for electrons far away from the axis (like in the tens of millimeter range). On the other hand, if the electron is very near to the axis, like in the sub micron meter range, 10^{-6} accuracy gives less than a 10^{-12} meter step, which makes the program inefficient. In order to control the global truncation error to be in the nanometer range and minimize the degradation of program's efficiency, an absolute desired accuracy, typically 10^{-4} nanometers or less, for the local truncation error at each step was found to give reliable results. It was also necessary to set a maximum permissible step-size, which

will prevent the step size to be enlarged too much especially in a discontinuous field. It is set to be 10^{-3} of the entire length of the field in this case.

The performances of the Cash Karp Runge-Kutta and the fixed step conventional 4^{th} order Runge-Kutta method were compared for a combined electric retarding field and magnetic immersion objective lens [16] (also called mixed field immersion lens), which gives the highest possible image resolution without aberration correction [3]. The fixed step 4^{th} order Runge-Kutta subroutine in the program ABAXIS2, part of the KEOS package [17] was substituted by the Cash Karp Runge-Kutta subroutine written by the author, which is attached in the appendix. This program implements integration of the standard paraxial equation and calculates on-axis aberrations and first order focal properties. The new trajectory integration program is given a new name, ABAXIS3. Figure 2.1 shows the configuration and axial field distributions for the mixed field immersion objective lens test example.

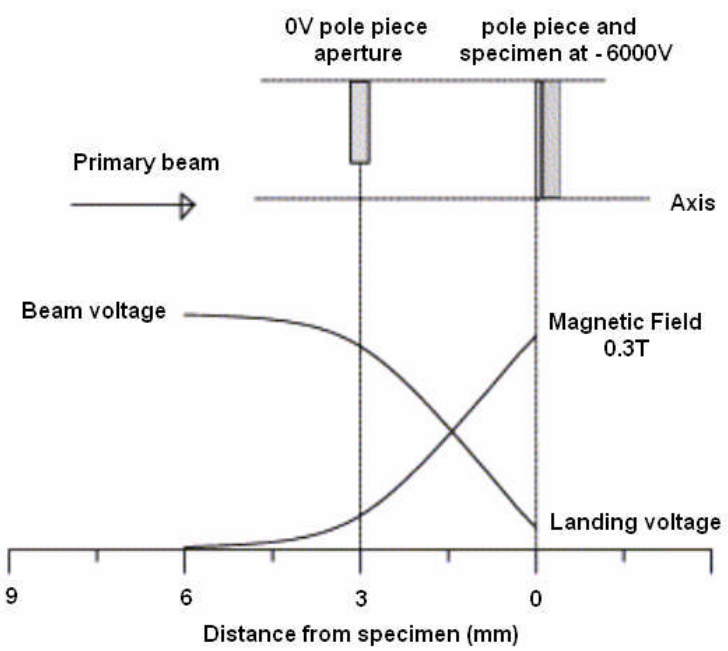

Figure 2.1: Configuration and axial field distributions for the mixed field immersion objective lens test example.

The primary beam voltage will drop 6000V from a distance of just 6mm before the specimen, and at the same time the magnetic field will focus the beam onto the specimen. The comparison was done for a parallel primary beam, where its landing energy varied from 500eV to 10eV. The aperture radius is 25μm. As an example Figure 2.2 shows the focal length vs. landing energies for the two Runge-Kutta methods.

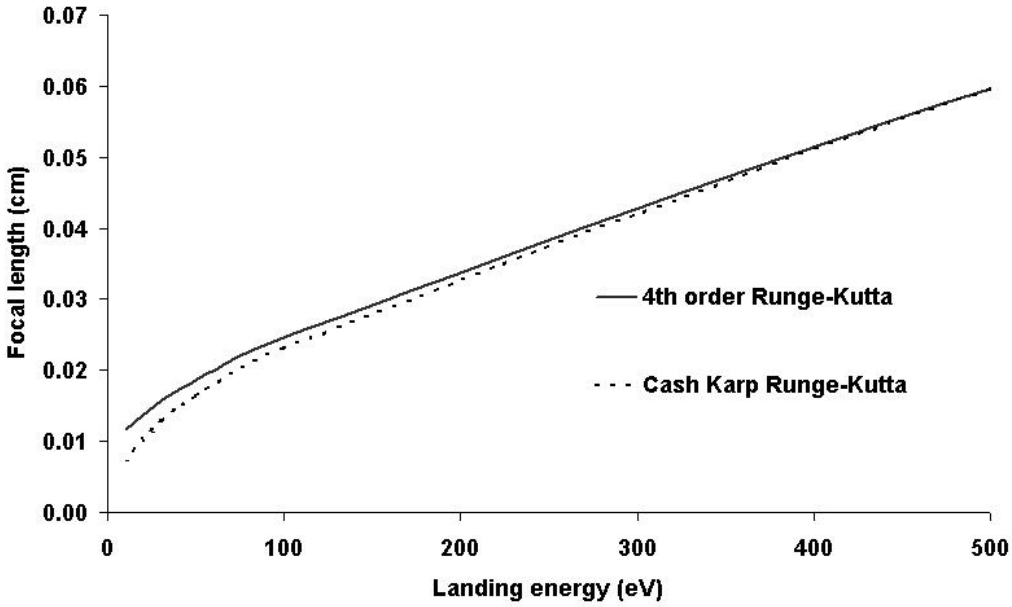

Figure 2.2: Focal length of the mixed field immersion objective lens as a function of the landing energy for 4th order and Cash Karp Runge-Kutta method

The values calculated from the two methods agree with each other very well for higher landing energies, but the difference between them becomes larger and larger as the landing energies decrease. In order to have a better understanding of this deviation, the electron trajectories in the lens are plotted for the two Runge-Kutta methods as shown in Figure 2.3a and 2.3b.

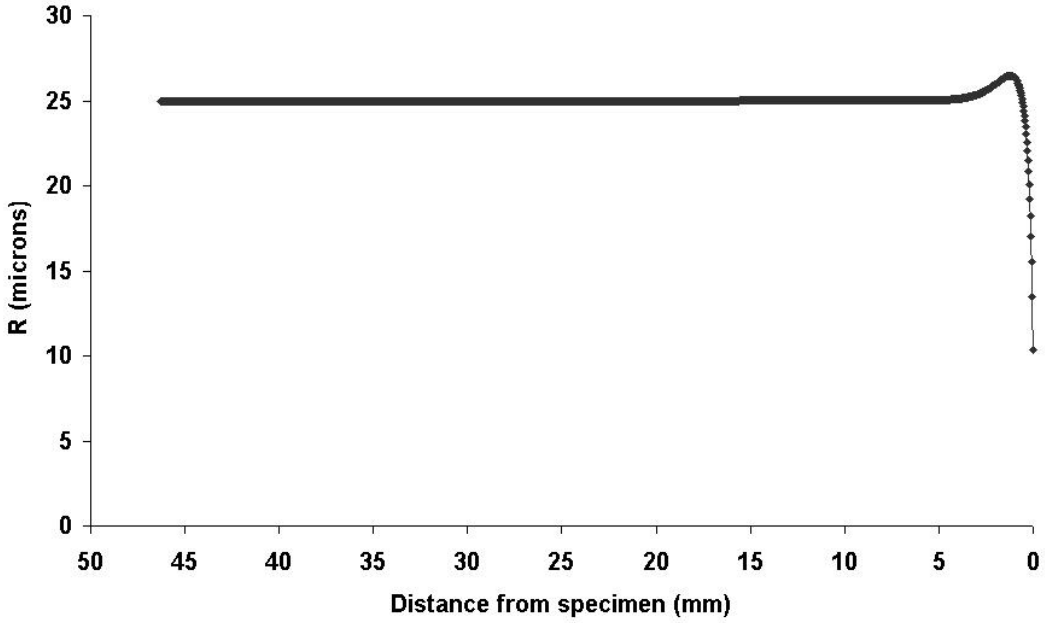

(a)

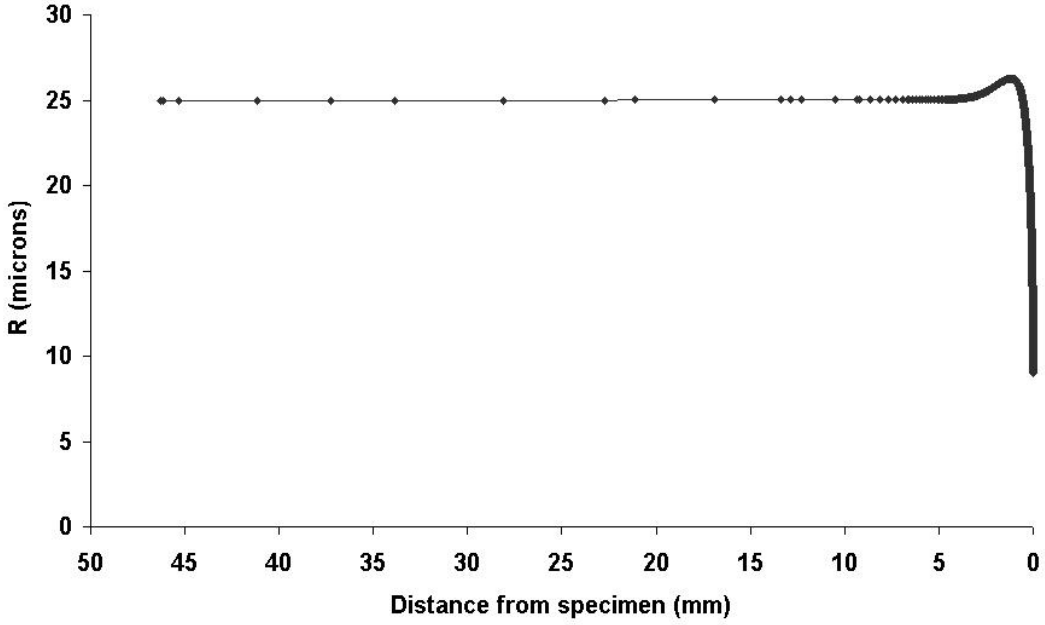

(b)

Figure 2.3: Electron trajectory paths through the mixed field lens test example
(a) Fixed step standard 4th-order Runge-Kutta
(b) Cash Karp Runge-Kutta

We can see from Figure 2.3 that before around 10mm from the specimen, where both the electric and magnetic fields are equal to zero, step sizes for the Cash Karp Runge-Kutta method are increased to the several mm level, which makes the program much more efficient. When both field distributions start to change sharply (within 10mm from the specimen), the step sizes of the Cash Karp Runge-Kutta are adjusted automatically to the level of several tenths of one mm to tiptoe through the fast changing field and control the errors within the tolerance level, which increases the accuracy of the program. The fixed step size for the 4^{th} order Runge-Kutta method is, in comparison, more inaccurate and less efficient.

2.2 Axial Fourier series expansions

A reliable direct ray tracing program needs high accuracy for both the trajectory integrating method and also for the field solving algorithm, which calculates the field value for any given point. To solve the field in the first place, a finite element program [18] , which is part of the KEOS package [17], simulates the real lens and calculates the axial electric potential $\phi(z)$ and axial magnetic field distribution *B(z)*. A Fourier fit to the axial field distributions is then made, so that smooth higher derivatives can be calculated in a series expansion method to obtain off-axis field values [4]. The detailed procedure of representing the axial field distributions as Fourier series will be outlined in the rest of this chapter and the Fortran 77 source code is attached in the appendix.

The overall length of the axial flux density function is defined as L, with a starting point at $z = 0$ and ending at $z = L$. We are going to fit the axial functions $\phi(z)$ and $B(z)$, which are computed at discrete points on the z-axis, with a Fourier series of the general form:

$$B(z) = \sum_{m=1}^{M} C_m \sin\left(\frac{m\pi z}{L}\right) + az + b$$
$$\phi(z) = \sum_{m=1}^{M} D_m \sin\left(\frac{m\pi z}{L}\right) + az + b \qquad (2.8)$$

where M is the number of terms, a and b are constants, C_m and D_m are series coefficients. The linear terms $az+b$ have been included since in the case of the mixed field immersion objective lens [3], both axial electric potential and magnetic field distributions have non-zero values at their boundaries. In order to have a zero value at the boundaries, which is required by the fast *sine* transform [15], the axial functions $\phi(z)$ and $B(z)$ are firstly subtracted by a linear function $y=az+b$, which is determined by the two points at the boundaries. Then the obtained functions are fitted with a natural quintic spline interpolation curve, whose coefficients are calculated according to the algorithm in reference [19]. For given function values y_i of $f(x_i)$ over n discrete points,

$$f(x_i) = y_i \qquad i = 1,2,\ldots,n. \qquad (2.9a)$$

in each interval (x_i, x_{i+1}), the spline function $f(x)$ is a polynomial of 5^{th} degree:

$$f(x) = ((((F_i \times P + E_i) \times P + D_i) \times P + C_i) \times P + B_i) \times P + y_i \qquad (2.9b)$$

where $P = x - x_i$, and B_i , C_i , D_i , E_i , F_i in (2.9*b*) are computed spline coefficients:

$$\begin{aligned} B_i &= f'(x_i) \\ C_i &= f''(x_i)/2 \\ D_i &= f'''(x_i)/6 \\ E_i &= f''''(x_i)/24 \\ F_i &= f'''''(x_i)/120 \end{aligned} \qquad (2.9c)$$

The different polynomials are pieced together so that *f(x)* and its derivatives up to f'''' are continuous.

2^n (n=15 is used in our program) equally spaced points are interpolated on the quintic spline. Then the Fourier coefficients (C_m) are calculated by the fast *sine* transform [15]. The axial derivatives of *B(z)* can be computed analytically from Eq. (2.8):

$$B'(z) = \sum_{m=1}^{M} C_m \left(\frac{m\pi}{a}\right) \cos\left(\frac{m\pi z}{a}\right) + a, \qquad B''(z) = -\sum_{m=1}^{M} C_m \left(\frac{m\pi}{a}\right)^2 \sin\left(\frac{m\pi z}{a}\right), \qquad etc. \qquad (2.10)$$

The Fourier series (2.8) is then truncated after a finite number of terms M. For a typical electrostatic or magnetic lens, M = 64 is usually adequate [4]. But it was

found that on some occasions, at least M = 128 must be used in order to reduce spurious oscillations of the high order derivatives. A test example electric lens, whose axial potential distribution is shown in Figure 2.4, can be used to illustrate the effectiveness of the Fourier Series Expansion Method. The higher derivatives of the electric potential, 2^{nd} to the 5^{th} for this lens, are shown in Figures 2.5a-e for M = 64, and Figures 2.6a-e for M = 128. The numerical values on these graphs have been omitted for clarity.

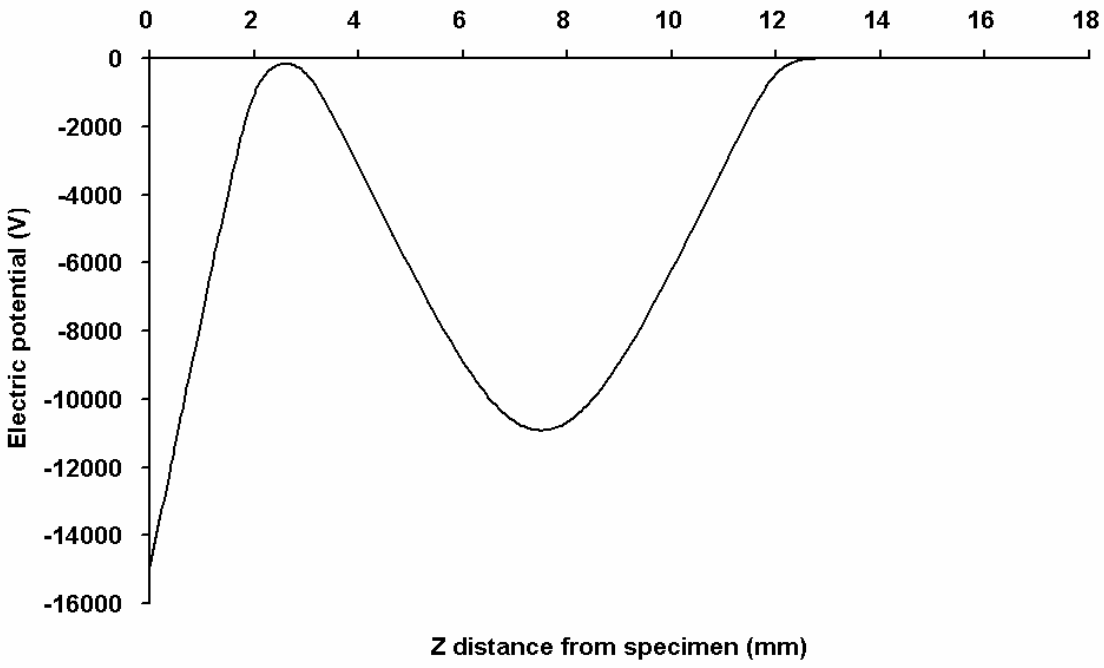

Figure 2.4: Axial electric potential distribution of a test electric lens

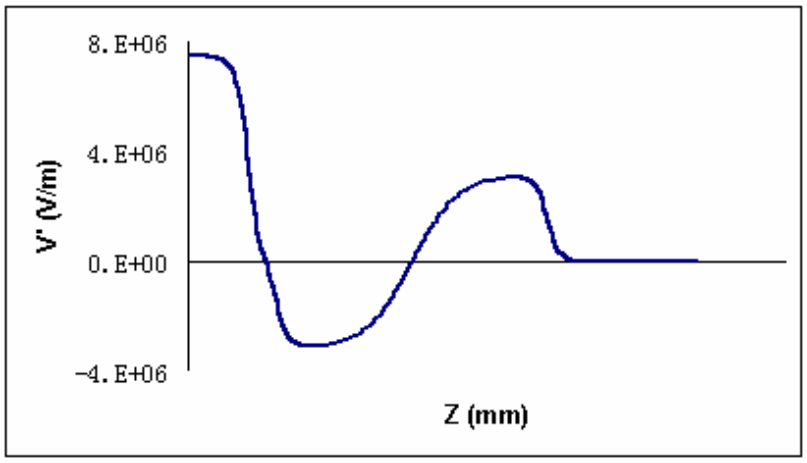
8.E+06
4.E+06
0.E+00
-4.E+06
V' (V/m)
Z (mm)

(a)

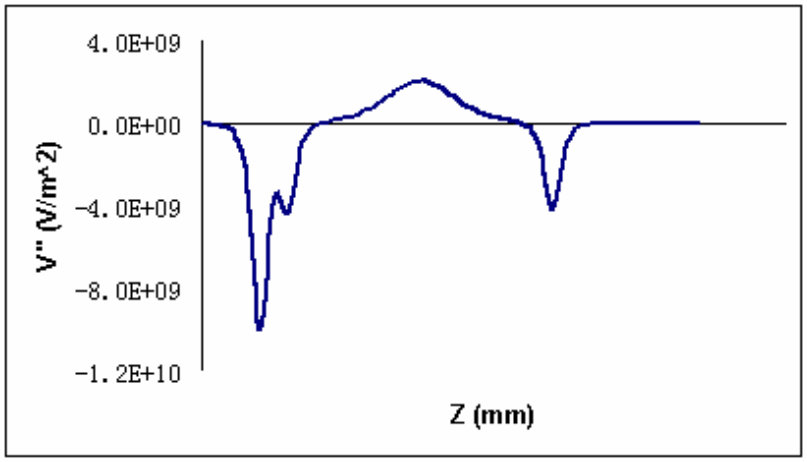
4.0E+09
0.0E+00
-4.0E+09
-8.0E+09
-1.2E+10
V'' (V/m^2)
Z (mm)

(b)

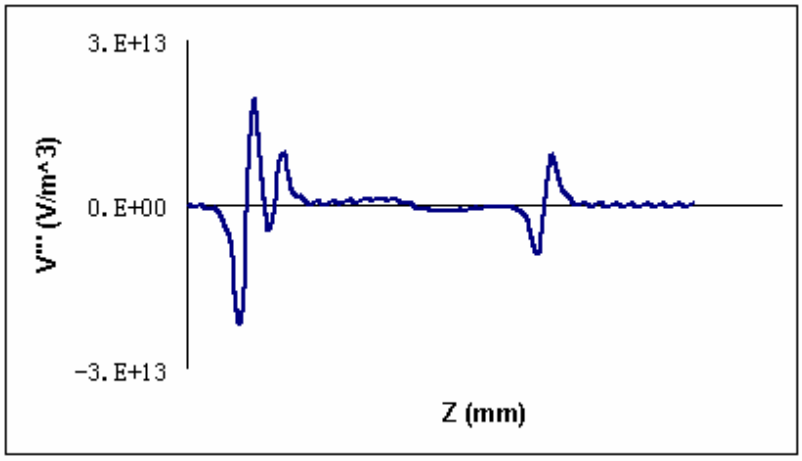
3.E+13
0.E+00
-3.E+13
V''' (V/m^3)
Z (mm)

(c)

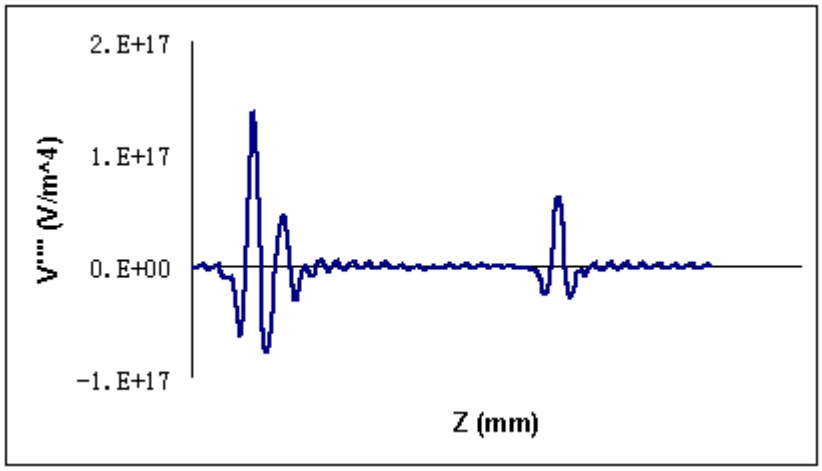

(d)

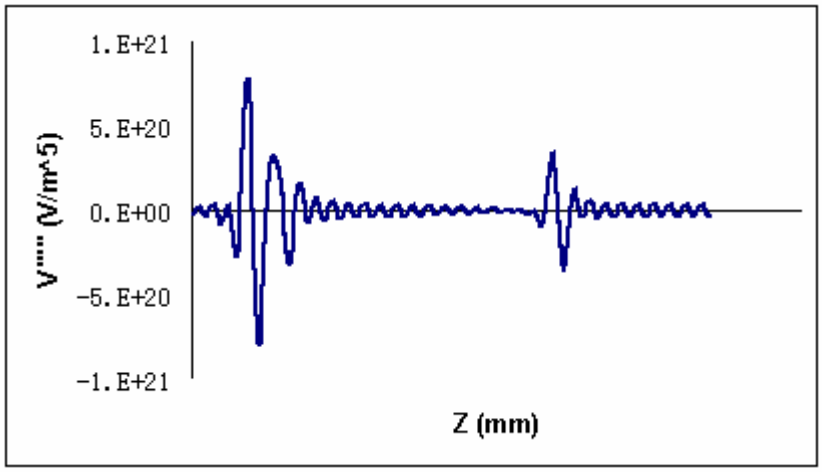

(e)

Figure 2.5: Higher derivatives of a test electric lens calculated by the Fourier Series Expansion method for M=64
(a) 1st derivative
(b) 2nd derivative
(c) 3rd derivative
(d) 4th derivative
(e) 5th derivative

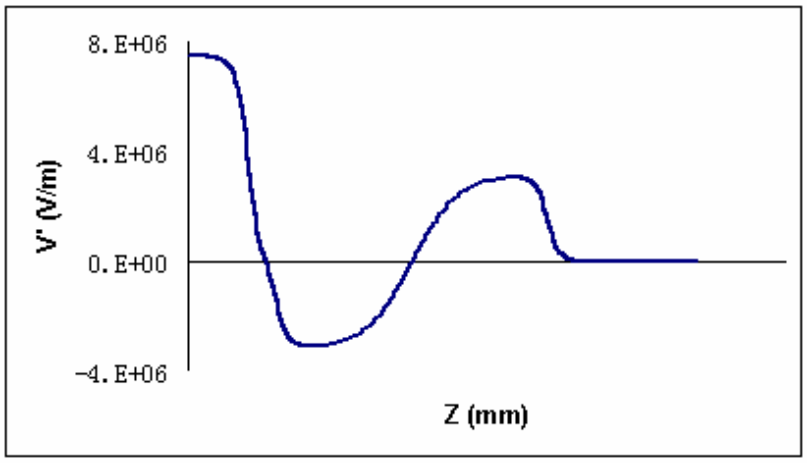
8.E+06
4.E+06
0.E+00
-4.E+06
V' (V/m)
Z (mm)

(a)

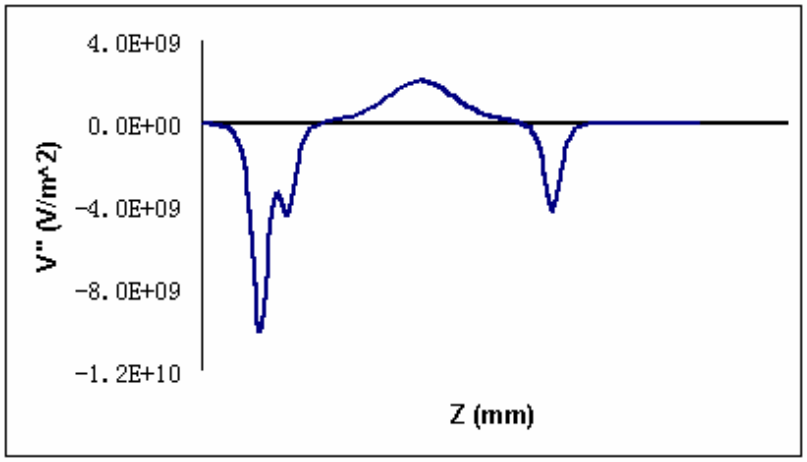
4.0E+09
0.0E+00
-4.0E+09
-8.0E+09
-1.2E+10
V'' (V/m^2)
Z (mm)

(b)

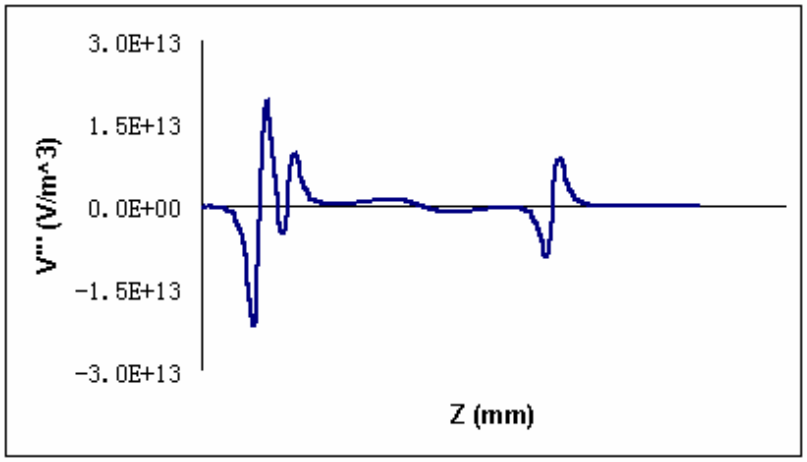
3.0E+13
1.5E+13
0.0E+00
-1.5E+13
-3.0E+13
V''' (V/m^3)
Z (mm)

(c)

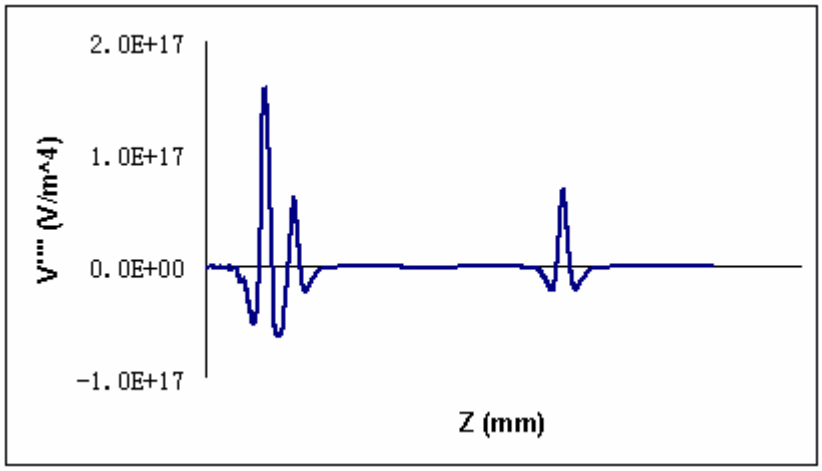

(d)

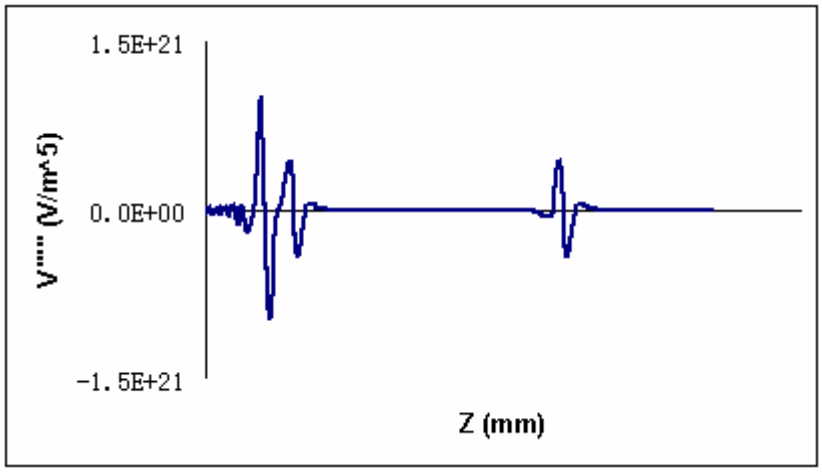

(e)

Figure 2.6: Higher derivatives of a test electric lens calculated by the Fourier Series Expansion method for M=128
(a) 1st derivative
(b) 2nd derivative
(c) 3rd derivative
(d) 4th derivative
(e) 5th derivative

From the original axis electric potential distribution, we can see that the specimen is at -15kV, electrons with energy less than 1 eV emitted from the specimen by either UV or laser beam excitation are extracted out and then focused to a point located at

around 7.5 mm from the specimen. For M=64 and M=128 the original axis potential function and its 1st and 2nd order derivatives are exactly the same, but for 3rd order derivatives and above, obvious oscillations appears for M=64, but on the other hand for M=128, these oscillations have been significantly reduced.

After the correct value of M is determined, the axial and radial field components can be obtained from the power series expansions [4]. Similar to Eq. (2.10) the axial derivatives of $\phi(z)$ can be obtained analytically from Eq. (2.8) and then E_z and E_r are computed using:

$$E_z(z,r) = -\phi'(z) + \frac{1}{4}\phi''(z)r^2 - \frac{1}{64}\phi''''(z)r^4 + \frac{1}{2304}\phi''''''(z)r^6 + \ldots \qquad (2.11a)$$

$$E_r(z,r) = \frac{1}{2}\phi''(z)r - \frac{1}{16}\phi'''(z)r^3 + \frac{1}{384}\phi'''''(z)r^5 + \ldots \qquad (2.11b)$$

and B_z and B_r are calculated by:

$$B_z(z,r) = B(z) - \frac{1}{4}B''(z)r^2 + \frac{1}{64}B''''(z)r^4 - \frac{1}{2304}B''''''(z)r^6 + \ldots \qquad (2.12a)$$

$$B_r(z,r) = -\frac{1}{2}B'(z)r + \frac{1}{16}B'''(z)r^3 - \frac{1}{384}B'''''(z)r^5 + \ldots \qquad (2.12b)$$

The expressions (2.11) and (2.12) are then used in the direct ray-tracing algorithm together with the Cash Karp Runge-Kutta method described in the beginning of this chapter.

In cylindrical *(z,r)* coordinates, the electric fields *(E_z, E_r)* are given by Eqs.(2.11) and the magnetic fields *(B_z, B_r)* by Eqs.(2.12). For solving the equations of motion (2.2), we need the fields to be expressed in Cartesian *(x, y, z)* coordinates. The Cartesian components of the electric field *(E_x, E_y, E_z)* and magnetic flux density *(B_x, B_y, B_z)* at any required point *(x, y, z)* are obtained from the cylindrical components in the round lenses, which are rotationally symmetric, with the aid of simple formulae:

$$E_x = E_r \frac{x}{r}, \qquad E_y = E_r \frac{y}{r}, \qquad E_z = E_z, \qquad B_x = B_r \frac{x}{r}, \qquad B_y = B_r \frac{y}{r}, \qquad B_z = B_z \tag{2.13}$$

2.3 Tests on accuracy

A direct ray tracing program was developed which uses both the subroutines of the Cash Karp Runge-Kutta method and Fourier series expansion for the axial field distribution. The program plots a series of trajectories in order to calculate first-order lens properties and on-axis aberrations.

For the on-axis spherical aberration, the energy of the incoming beam E_i is fixed, and the input semi angle α_i is varied from a value near to zero to a certain value in a number of equally spaced steps. All the values of output or image semi angles α_o and the focal positions P_o are stored. Linear extrapolation is used to calculate the zero input semi angle's focal position, which is subtracted by all the focal positions of other input semi angles to obtain the corresponding differences in the focal positions

Δz. The aberration spot radius Δr is calculated by multiplying the output or image semi angle α_o with its Δz. Then either 3rd order or 5th order spherical aberration coefficients, C_{S3} and C_{S5} respectively, can be readily calculated with α_o and Δr by

$$\Delta r = \alpha_o^3 C_{S3} + \alpha_o^5 C_{S5} \qquad (2.14)$$

The chromatic aberration calculation is very similar to that of the spherical aberration except the input semi angle α_i is fixed, and the input energy is varied over a certain energy spread ΔE around a certain input energy value E_i. The chromatic aberration, C_C, is the coefficient of the linear function of the input energy differences ΔE and the resulting aberration radius Δr, given by

$$\Delta r = \alpha_o \left(\frac{\Delta E}{E_i} \right) C_C \qquad (2.15)$$

An auto-focus feature was developed, where the magnetic field strength is successively scaled in order to focus the trajectory path at a desired location (specimen position). A scaling factor is chosen, α_1, and the distance between the resulting focal position and the specimen d_1 is used to calculate the next scale factor α_2 by the following equation $\alpha_2 = \alpha_1 - (d_1/r)$, where $r = (d_1 - d_0)/(\alpha_1 - \alpha_0)$, and d_0, α_0 are the values for the trial before d_1, α_1. In the very first trial d_0 is calculated for $\alpha_0 = 1$. Auto focus will automatically stop until the focal point falls into the desired range (normally less than 1nm) near the specimen.

The direct ray tracing program was tested and cross checked with existing known programs in the KEOS package [17]. It was compared to ABAXIS2/ABAXIS3, programs that use perturbation methods on the paraxial equation in order to derive on-axis aberration coefficients [20] The mixed field immersion objective [3] lens similar to the one given in Chapter 2.1 (Figure 2.1) is used as a test example here. The results calculated by the three programs are shown in the tables below:

50eV landing energy	Aperture (μm)	Angle	Magnetic field Scale Factor	Focal Length (cm)	Spherical Aberration(cm)
ABAXIS2	20	Parallel	1.23571	2.000030E-02	1.234495E-03
ABAXIS3	20	Parallel	1.24166	1.431650E-02	1.211547E-03
Direct ray tracing	20	Parallel	1.23387	1.431520E-02	1.285250E-03

Table 2.2a: Results calculated for 50eV landing energy electron beam in the mixed field immersion objective lens by three different trajectory integration programs

20eV landing energy	Aperture (μm)	Angle	Magnetic field Scale Factor	Focal Length (cm)	Spherical Aberration(cm)
ABAXIS2	20	Parallel	1.19738	1.667612E-02	2.822196E-04
ABAXIS3	20	Parallel	1.20449	9.568849E-03	5.809939E-04
Direct ray tracing	20	Parallel	1.19342	9.162170E-03	5.405141E-04

Table 2.3b: Results calculated for 20eV landing energy electron beam in the mixed field immersion objective lens by three different trajectory integration programs

From the data above we can see that the results calculated from direct ray tracing program give good agreement with those from ABAXIS3, which has been discussed earlier to be more accurate than ABAXIS2, especially for low landing-energy electron beams. Since the on-axis aberrations in ABAXIS2 and ABAXIS3 are calculated from perturbations of a 1^{st}- order trajectory equation (paraxial equation), comparison with the direct ray tracing method provides a good check on the effectiveness of both the Cash Karp Runge Kutta subroutine and the Fourier series expansion method to ensure smooth high-order derivatives of the axial field distributions. The fact that the two methods give good agreement shows that the direct ray tracing method is accurate enough to calculate on-axis aberration such as the 3^{rd}-order spherical aberration. The advantage of the direct ray tracing method is that it can calculate trajectories further from the axis than the perturbation method, in effect, calculating high-order effects.

CHAPTER 3

Low voltage SEM with mixed field objective lens

3.1 Primary beam optics

In reference [21], secondary electron images at low landing energies (below 50 eV) are presented by a portable field emission scanning electron microscope. The results show that nano-scale images of resolution better than 20 nm can be obtained on a nylon-fibre specimen at landing energies as low as 1 eV.

To gain a better understanding of the very low landing energy experimental results, simulations of the objective lens, which uses a combined electric retarding field and magnetic immersion action [3], were carried out. At very low energies, the narrow angle approximations and relative small energy variations in the paraxial equation/perturbation approach are no longer valid, and the more general method of direct ray tracing is required. Finite element programs [18] were used to calculate the axial potential and magnetic field distributions of the lens, while direct ray tracing of the primary beam provided an estimate of the probe radius at the specimen due to chromatic and spherical aberration. Direct ray tracing employed the Cash-Karp 5^{th} order Runge-Kutta technique in combination with a Fourier fit to the axial field distribution so that smooth higher derivatives could be calculated in a series expansion method to obtain off-axis field values [4], which was discussed in the

previous chapter. The simulated axial potential and magnetic field distribution above the specimen is shown in Figure 3.1. The graph depicts a 6 keV primary beam being decelerated down to an energy of 50 eV at the specimen.

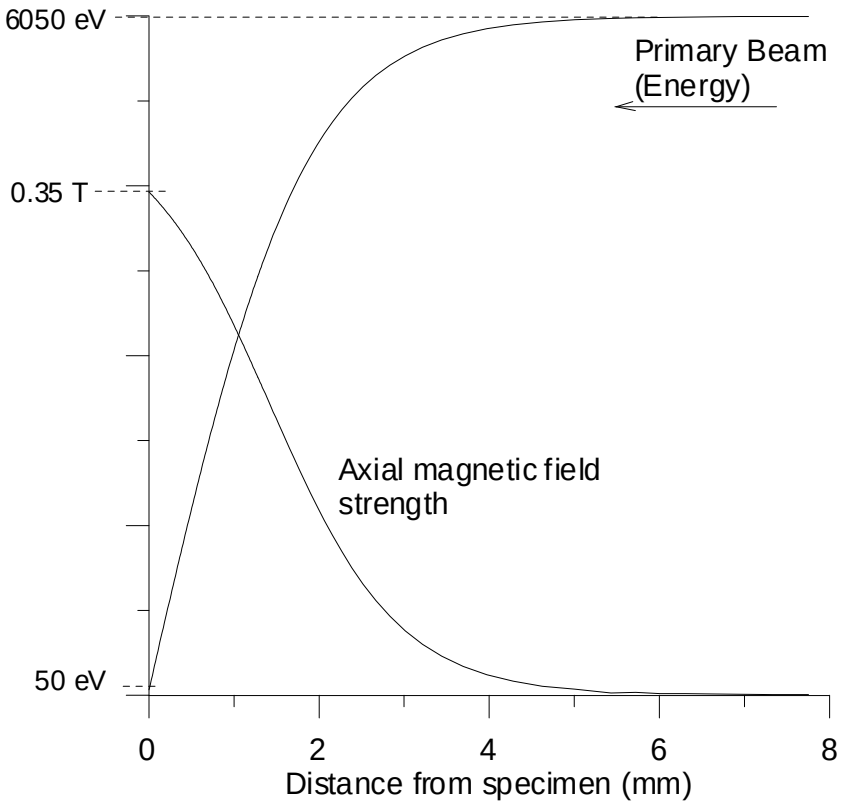

Figure 3.1: Simulated axial potential and magnetic field distributions for the objective lens

Only incoming parallel rays were simulated. Due to the low beam current, the coulomb interactions between electrons are insignificant and will be neglected in this work. The magnetic field strength was automatically scaled to focus the primary beam on to the specimen for different landing energies. At a primary beam energy of 6 keV, shifts of the focal position between landing energies of 1 to 50 eV were relatively small, and roughly equivalent to the kind of small specimen height adjustments used to achieve focusing (a permanent magnet objective lens is used in

this case). The aperture radius was varied up to 25 microns, and the beam energy spread of 0.5 eV was assumed (corresponding to a Schottky field emitter source). In order to estimate the on-axis third-order spherical aberration coefficient, C_s, ten parallel trajectories were plotted for radii varying up to 2.5 microns, and the subsequent focal positions and image semi-angles were noted. To estimate the on-axis chromatic aberration coefficient, C_c, different initial energies were used. Figure 3.2 shows the variation of the simulated on-axis aberration coefficients with landing energy. As a cross-check on these values, they were compared with the standard method of paraxial trajectory perturbation for 10, 20 and 50 eV landing energies. The values agreed to within 4% for 50 eV, and around 10% for 20 and 10 eV.

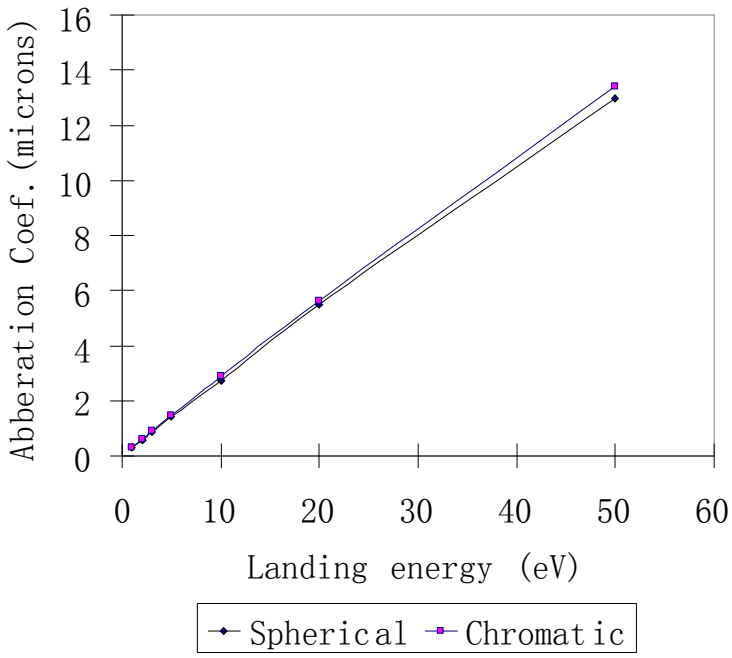

Figure 3.2: Variation of on-axis aberration coefficients with landing energy

Figure 3.2 shows that C_c and C_s fall linearly with landing energy and are approximately of the same magnitude. In addition to this variation, it is important to

analyze the increase in image semi-angle, which rises sharply as the landing energy decreases. This variation is depicted in Figure 3.3 for aperture radii of 10 and 25 microns. The large non-linear rise in semi-angle also clearly indicates why direct ray tracing is more suited to analyzing the objective lens characteristics for very low landing energies, as opposed to using paraxial trajectories, which are only valid for relatively small apertures (less than 2.5 microns).

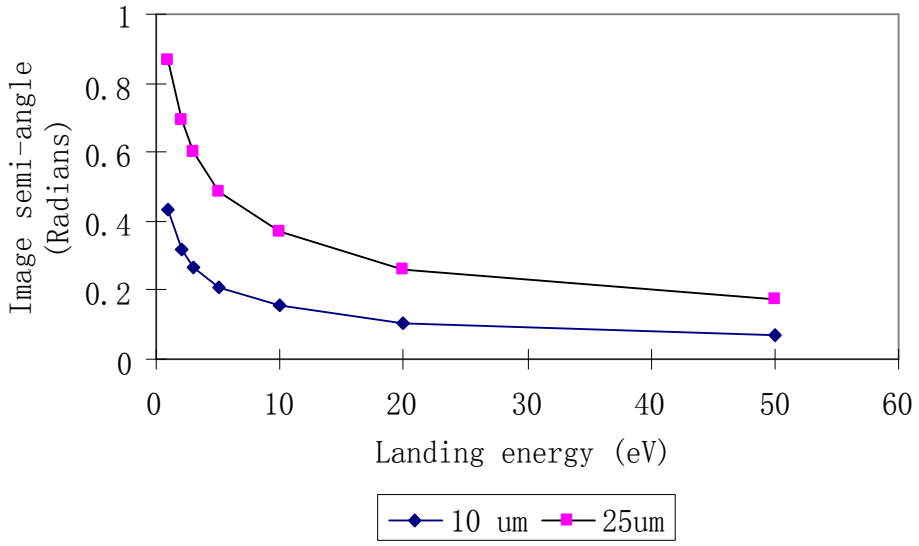

Figure 3.3: Simulated variation of image semi-angle with landing energy

Despite the falling aberration coefficients trend shown in Figure 3.2, the sharp rise in semi-angle, over 45 degrees at 1 eV for the 25 micron aperture, naturally leads to a rise in the effect of spherical aberration on the image probe size. The chromatic aberration effect is also expected to increase, since in addition to the rise in image semi-angle, the relative energy spread also increases. These effects can be seen in the simulated aberration radii shown in Figure 3.3, calculated for 10 and 25 micron

apertures. The spherical aberration spot clearly rises more steeply than the chromatic one, and there is a significant improvement as the aperture size is decreased.

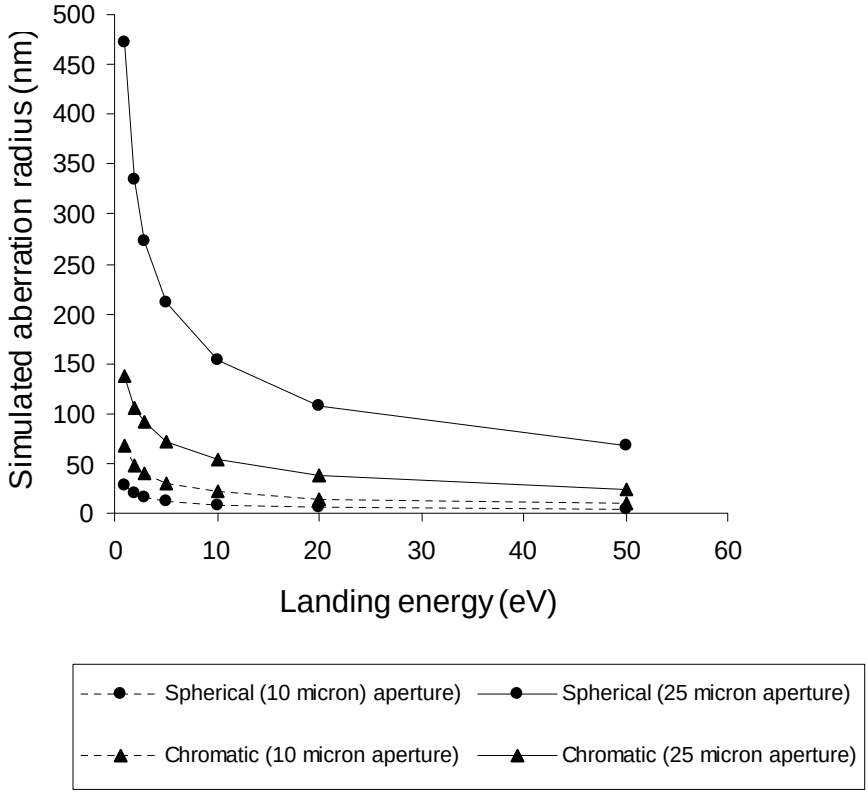

Figure 3.4: Simulated aberration radius at the specimen as a function of landing energy

The aberration predictions on the final probe size shown in Figure 3.4 are significantly higher than the experimental resolution results, which are under 20 nm for a 1 eV landing energy. There are several important factors that may account for this difference. Firstly, the correct effect of a given aperture size can only be made when the source position, as well as the effect of the gun lens is taken into account. The gun lens magnetic field is likely to collimate the electrons, effectively shifting the current distribution closer to the axis; this means the effect of the aperture in the

present simulations may be overestimated. Secondly, the nylon specimen used for resolution estimates may have been charging positively. Thirdly, electron-electron interaction effects may become significant as the primary beam slows down to very low energies above the specimen; these effects may reduce the image semi-angle in practice. Fourthly, the relatively poor vacuum in the SEM specimen chamber, typically between 10^{-6} to 10^{-5} Torr, causes a thin carbon film to be deposited on the surface, and this contamination layer is quite likely charging positively.

In the present context, it is sufficient to note that the experimental resolution estimate is much better than that predicted by simulation, and that there is thus much more analysis required to adequately understand secondary image formation at very low landing energies by a field emission SEM.

3.2 Scattered electron distribution

Direct ray tracing through a mixed field objective lens is also required for the design of a spectroscopic SEM [5]. In this case, it is the accurate plotting of scattered electron trajectory paths that is needed, those that are emitted and reflected back from the specimen after the primary beam strikes it.

Figure 3.5a shows a schematic diagram of the transfer and objective lenses used for finite-element modeling. Figures 3.5b and 3.5c depict the subsequent calculated field distributions suitable for focusing a 7 kV primary beam on to a specimen that is biased to −6 kV (providing a landing voltage of 1 kV).

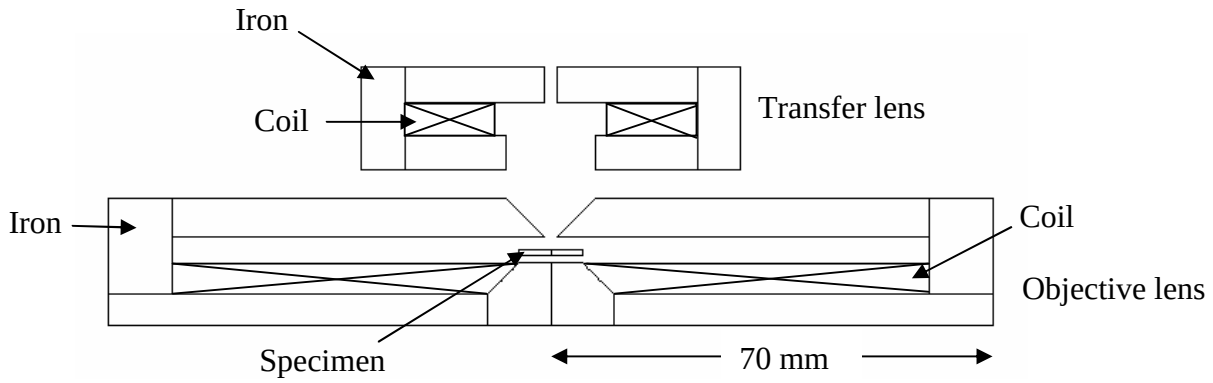

(a)

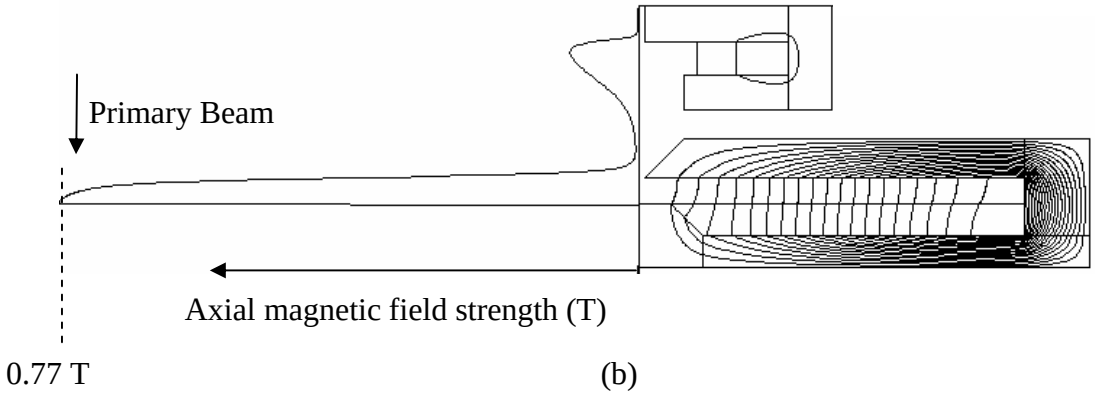

(b)

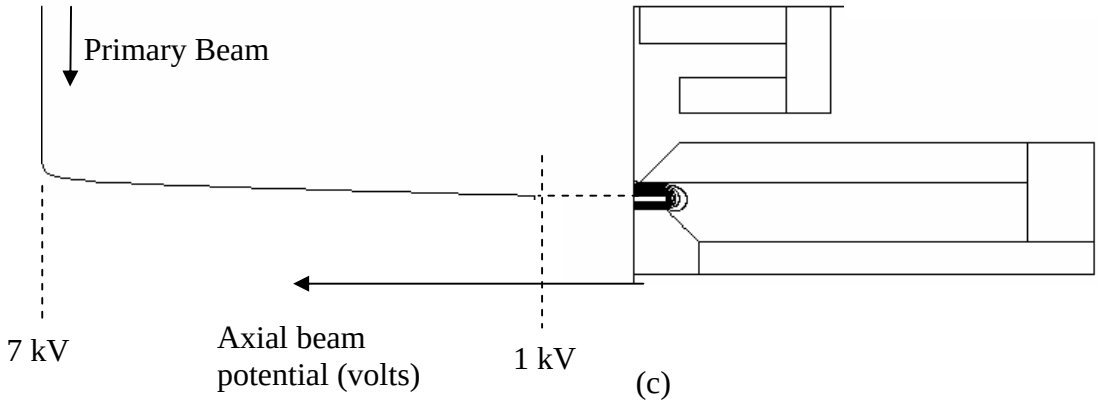

(c)

Figure 3.5: Simulation of the transfer lens and objective lens field distributions
(a) Overall layout
(b) Flux distribution and the axial magnetic field strength
(c) Equipotential lines and axial beam potential

To investigate the behavior of scattered electrons in the proposed spectroscopic SEM, the direct ray tracing program discussed in chapter 2 was used to trace the trajectory paths of low energy secondaries and backscattered electrons through both the objective lens and transfer lens.

It is instructive to first examine the ray paths above the specimen, as they make their way through the objective lens bore. These ray paths are shown in Figure 3.6 at emission energies 1, 3, 5, 200 eV and 1 keV for emission angles up to 1 rad (primary beam at 7 kV and specimen voltage at −6 kV).

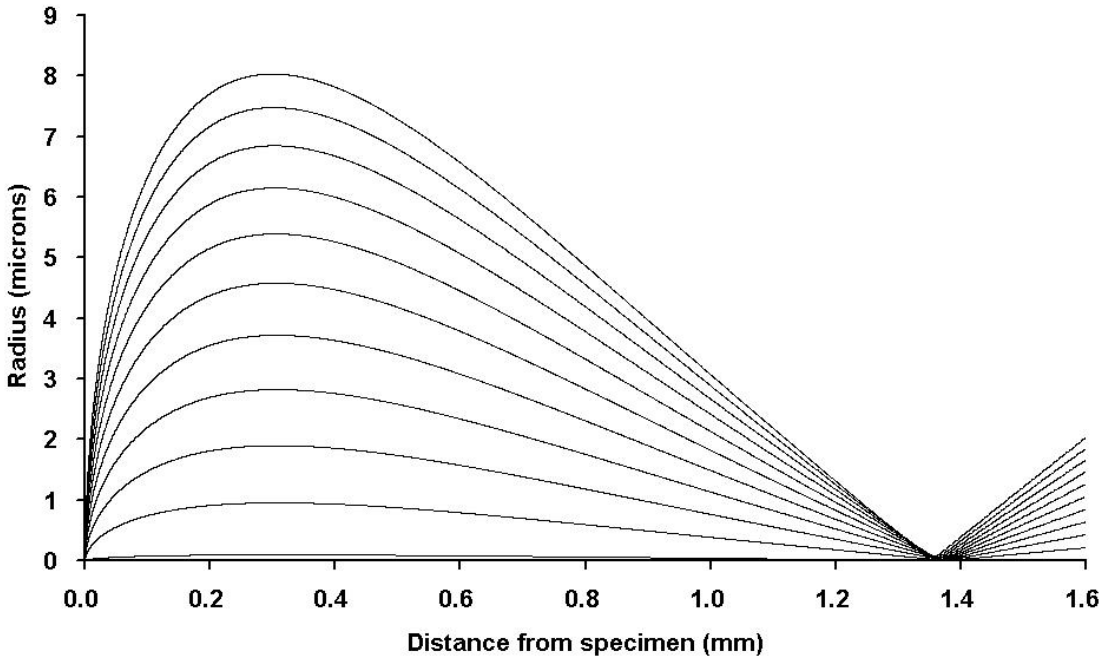
Radius (microns)
0
1
2
3
4
5
6
7
8
9
0.0
0.2
0.4
0.6
0.8
1.0
1.2
1.4
1.6
Distance from specimen (mm)

(a)

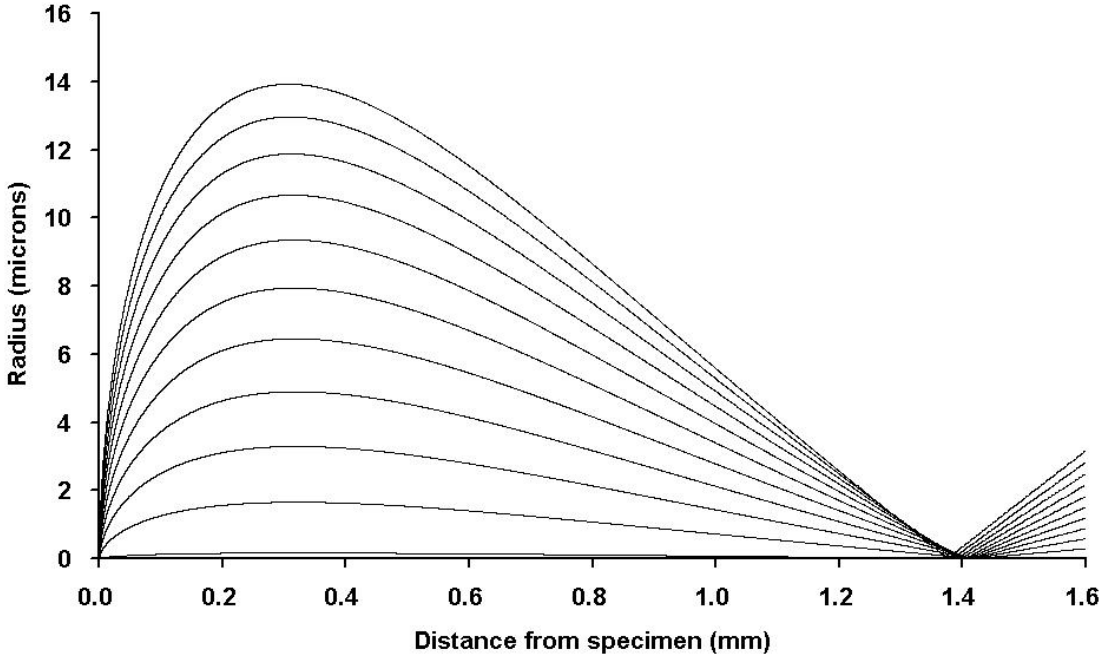
Radius (microns)
0
2
4
6
8
10
12
14
16
0.0
0.2
0.4
0.6
0.8
1.0
1.2
1.4
1.6
Distance from specimen (mm)

(b)

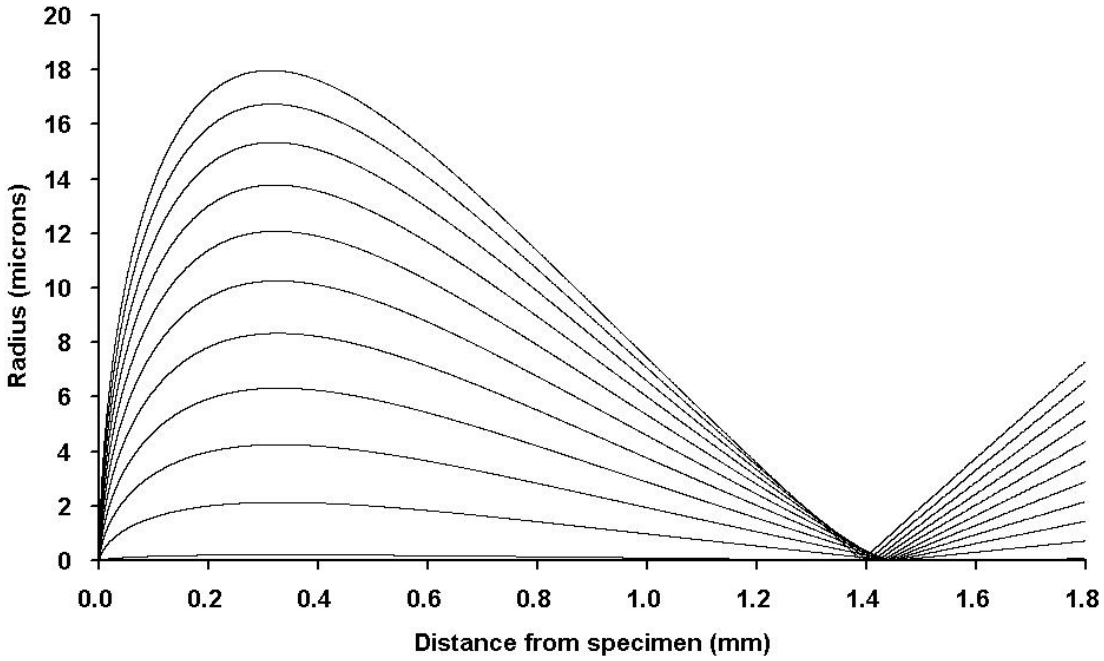
Radius (microns)
20
18
16
14
12
10
8
6
4
2
0
0.0
0.2
0.4
0.6
0.8
1.0
1.2
1.4
1.6
1.8
Distance from specimen (mm)

(c)

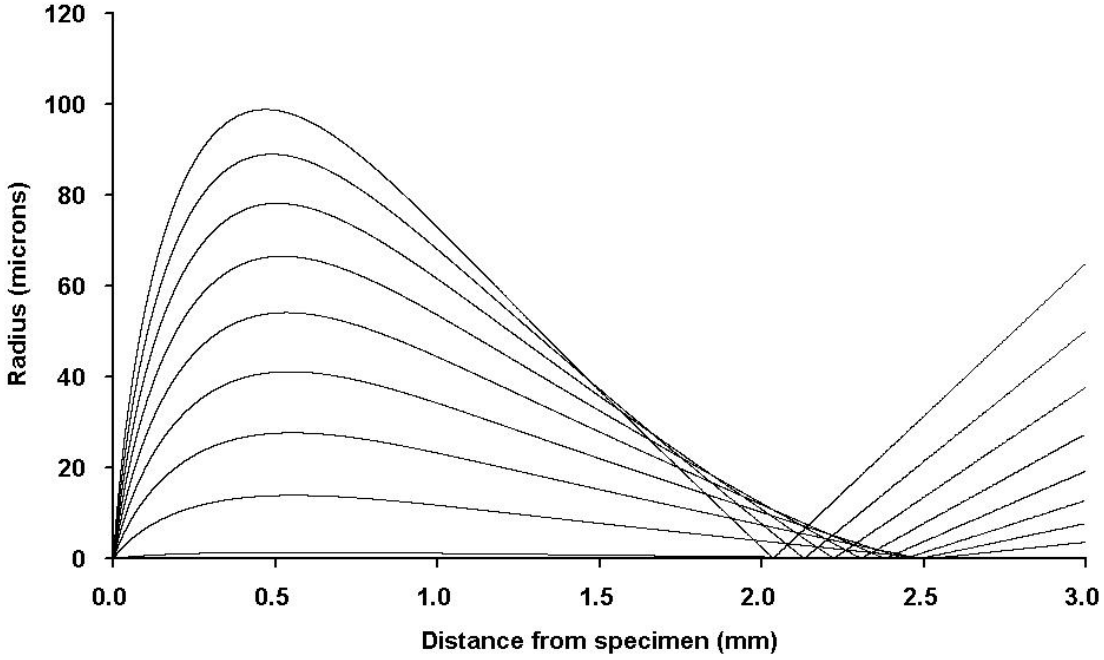
Radius (microns)
120
100
80
60
40
20
0
0.0
0.5
1.0
1.5
2.0
2.5
3.0
Distance from specimen (mm)

(d)

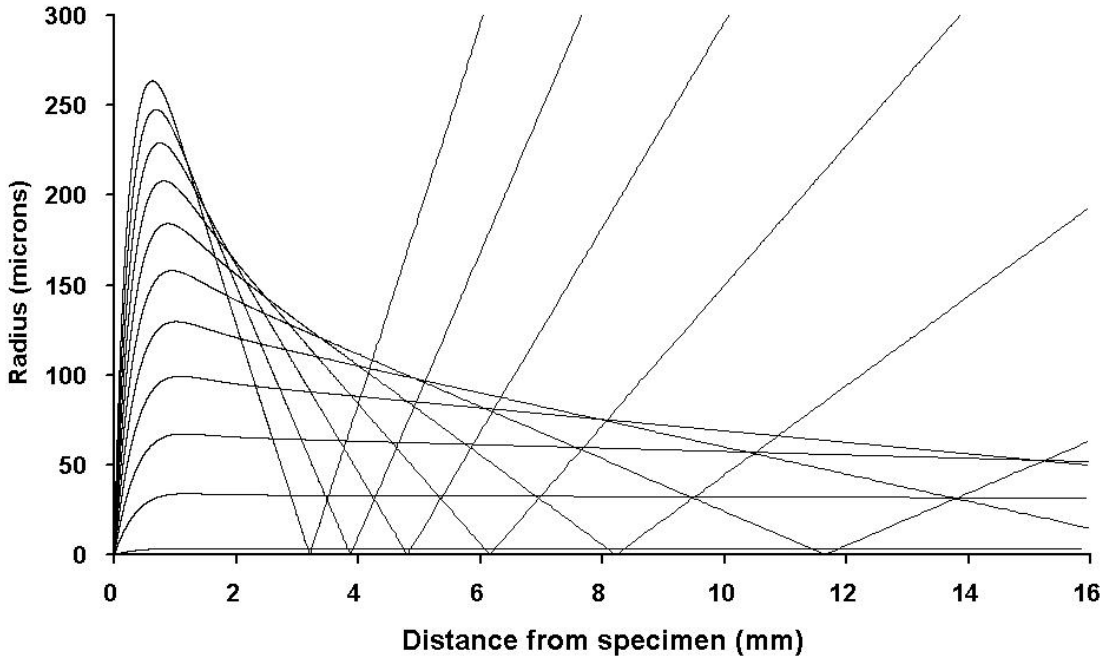

(e)

Figure 3.6: Simulated trajectory paths of scattered electrons through the objective lens (primary beam of 7 keV and specimen voltage – 6 kV)
Scattered electrons' emission energy:
(a) 1 eV
(b) 3 eV
(c) 5 eV
(d) 200 eV
(e) 1 keV

Figure 3.6a shows that the 1 eV secondaries cross the axis at 1.4 mm above the specimen, defining the position of their virtual source, that is, the position where they subsequently appear to come from. It is 0.6 mm away from the objective lens upper pole-piece bore (the specimen has a working distance of 2 mm). The wider angle 3 eV secondaries cross the axis further up the z-axis and this effect becomes more pronounced as the secondary energy increases, as shown in Figure 3.6c for the 5 eV electrons. At 200 eV, all scattered electrons cross the axis with a much larger spread

and they subsequently appear to emanate from points located between 2.0 and 2.5 mm above the specimen (for emission angles up to 1 rad). For the backscattered electrons (1 keV energy), the situation is quite different, as expected. The lower emission angles are parallel (same as the primary beam as it approaches the specimen), as shown in Figure 3.6e, however, above 0.3 rad, higher-order aberrations in the lens cause the wider angle backscattered electrons to cross the axis. The backscattered electrons appear to emanate from a wide variety of different virtual source positions as they exit the objective lens.

From the simulation results depicted in Figure 3.6, it is clear that spherical aberration effects on the scattered electrons become dominant for higher emission energies. For the lower energies, chromatic effects dominate, and scattered electrons appear to exit the objective lens as if they emanate from a definite point. This gives rise to the possibility of obtaining spectral effects for the low-energy electrons (since spherical aberration effects for them are relatively small). Figure 3.7 shows how simulated exit angles from the objective lens for secondary electron energies up to 5 eV vary as a function of initial emission angle.

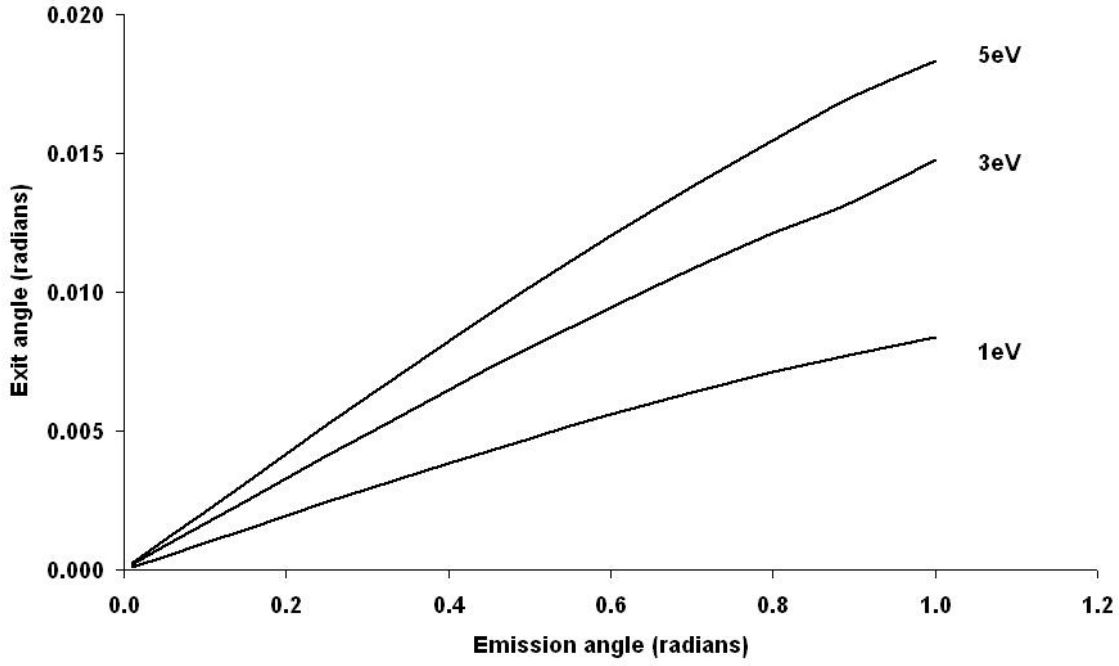

Figure 3.7: Simulated objective lens exit angles of low-energy secondary electrons as a function of emission angle.

The exit angle variation will naturally be translated into radial variations as the secondary electrons travel beyond the objective lens bore. If a cosine angular distribution on the emission angle is used, *cos(θ)*, where θ is the emission angle, then the relative number of secondaries as a function of radius can be obtained. The relative number of secondaries N, is then proportional to *sin(2θ)* (due to the rotational symmetry of emission) and also related to the work function ϕ of the specimen, which by the Chung-Everhart formula [22] in terms of emission energy E_0 and specimen biasing voltage V is given by

$$N = \frac{\sin(2\theta)\times\left[6(E_0 - V)\times\phi^2\right]}{(E_0 - V + \phi)^4}$$

In order to investigate the radial distribution of the secondary electrons, the relative number of electrons with emission energy from 0eV to 10eV (step size 0.5eV) are calculated first as a function of radius at a certain distance from the specimen (66mm in this case). Then the entire radial spread is divided into *n* segments (*n* = 11 for this case), and all the relative numbers falling into each segment are added up to obtain the total relative number for that segment.

The resulting radial distribution of the secondary electrons at a distance of 66 mm above the specimen (for no transfer lens present) for an aluminum sample (work function is 4.28 eV) at different biasing voltages is shown in Figure 3.8a. Similar results for samples with the same biasing voltage (-6 kV) but made by different materials are shown in Figure 3.8b.

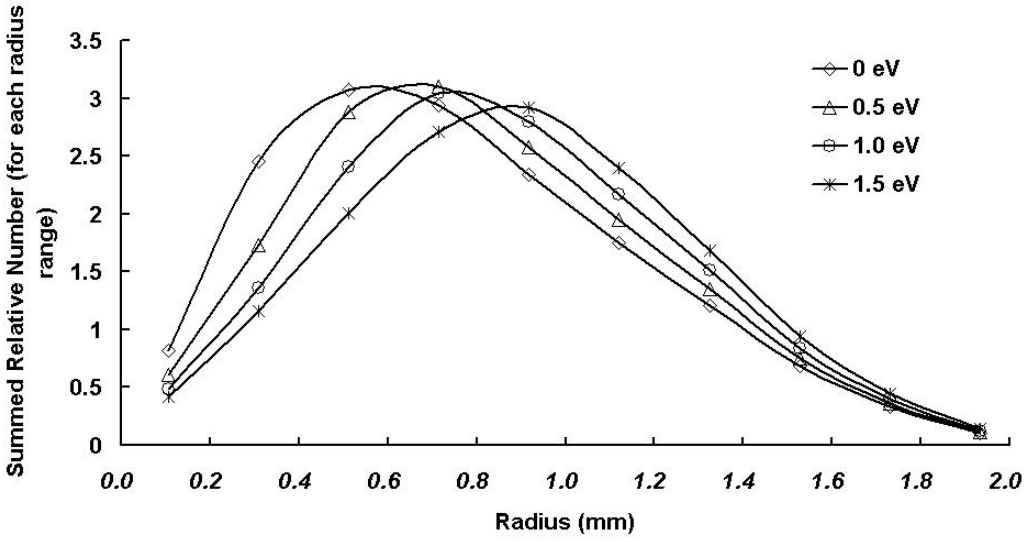

(a)

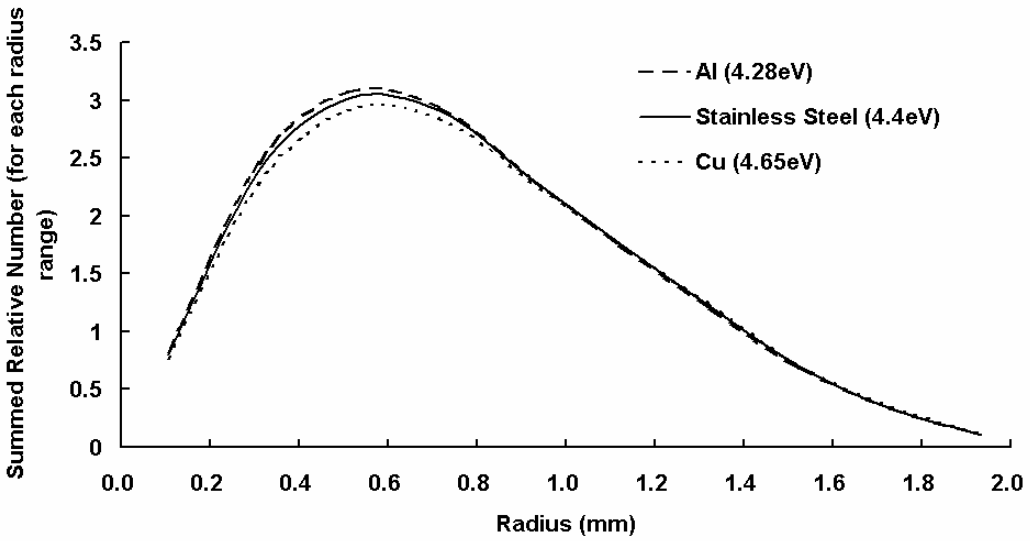

(b)

Figure 3.8: Simulated radial distribution of secondary electrons at 66 mm above specimen with no transfer lens present. Sample bias is -6 kV.
(a) Aluminum sample at different biasing voltages (0V, 0.5V, 1V, 1.5V) above -6 kV
(b) Samples at -6 kV made by different materials (aluminum, stainless steel and copper)

Figure 3.8 shows considerable contrast for the low-energy spectrum. If a small annular multi-channel detector were to be placed above the objective lens, at a suitable height and having a small hole at its centre (say less than 200 μm radius if placed at 66 mm above the specimen), then the simulation results depicted in Figure 3.8a and 3.8b predict that a signal related to the secondary energy spectrum can in principle be captured, which can either been used to tell the sample's biasing voltage and/or identify the material type of the sample.

The simulation results presented here are only meant to indicate the possibility of obtaining the energy spectrum of the lower energy secondaries with the type of

objective lens shown in Figure 3.5 (without the presence of the transfer lens). These results show for instance, that a small aperture suitably placed above the objective lens would produce significant voltage contrast. Similar predictions have been made by Khursheed A. et al [5]. Since the retarding field magnetic immersion lens considered here has low aberrations, particularly at low landing energies, the possibility of forming a secondary electron energy spectrometer by simply mounting an annular multi-channel detector above the objective lens may be significant for applications such as electron beam testing (quantitative voltage contrast).

CHAPTER 4

Conventional PEEM objective lens and mixed field lens for Time-Of-Flight Electron Emission Microscope

A PEEM (photoemission electron microscope) is one type of electron microscope, whereby electrons emitted from the surface of a sample by photoemission are used to image the surface. The emitted electrons are focused by electron lenses onto a screen, where a magnified image of the surface is visible. A conventional electrostatic objective lens design is shown in Figure 4.1, where the specimen is biased to a negative voltage, typically -15 kV. A focusing electrode is set to -13.3 kV, adjusting the focal plane to which the photoelectrons are focused. The field distribution shown in Figure 4.1b was obtained by running Finite Element programs written by A. Khursheed and are reported in detail elsewhere [18].

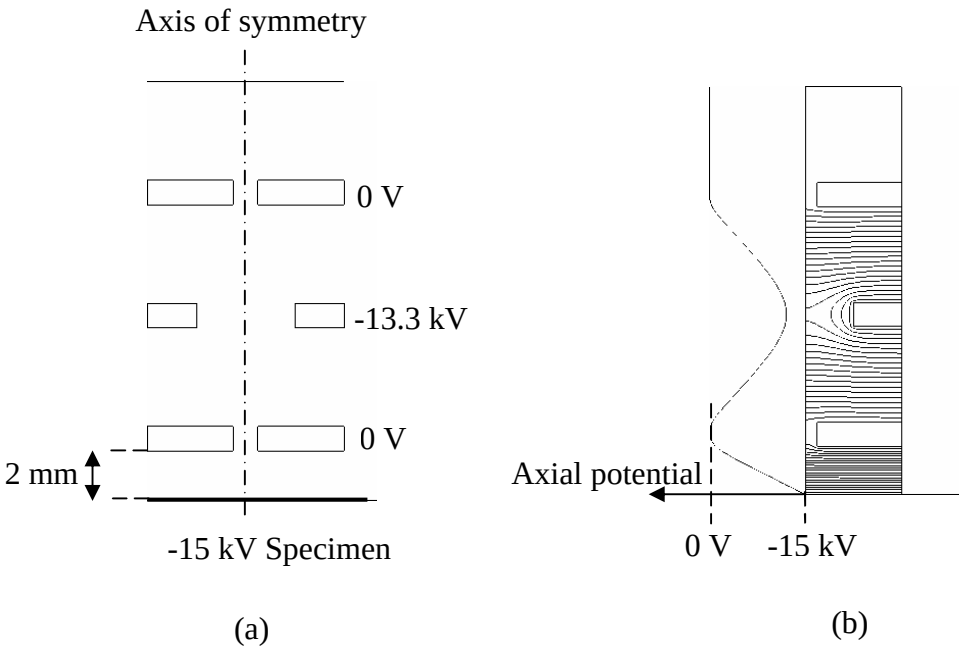

Figure 4.1: Simulation model of objective lens
(a) Electrode layout
(b) Equipotential lines and axial potential distribution

Direct ray tracing of electrons through finite element field solutions is carried out through the use of a field expansion technique involving the axial electric potential/magnetic field distributions and their derivatives up to 7^{th}-order, as reported by E. Munro [9], which has already been discussed in Chapter 2. Due to the relatively low yield of photoelectrons, Coulomb interactions are neglected in this work. Here the axial potential and field distributions are fitted with a Fourier-series technique in order to facilitate high-order differentiation. More than 128 terms were required in the Fourier-series to ensure smooth higher-order derivatives. A 5^{th}-order Runge-Kutta method with Cash-Karp parameters is used to numerically integrate the equations of motion. To ensure high accuracy, up to 12,000 steps in each trajectory were used.

Example trajectory paths for the electric objective lens are shown in Figure 4.2, where 0.5 eV photoelectrons leave the specimen over angles ranging from 0 to 0.6 radians with respect to the optical axis in steps of 0.1 radians. The focusing electrode at a voltage of -13.3 kV projects the first intermediate focal plane to a distance of 23 cm from the specimen, giving an image magnification of 17. A contrast aperture is placed in the back focal plane of the lens, which measures a distance of 2.87 cm from the specimen. This aperture is used to reduce the energy and angular spread of the photoelectrons that make up the final image.

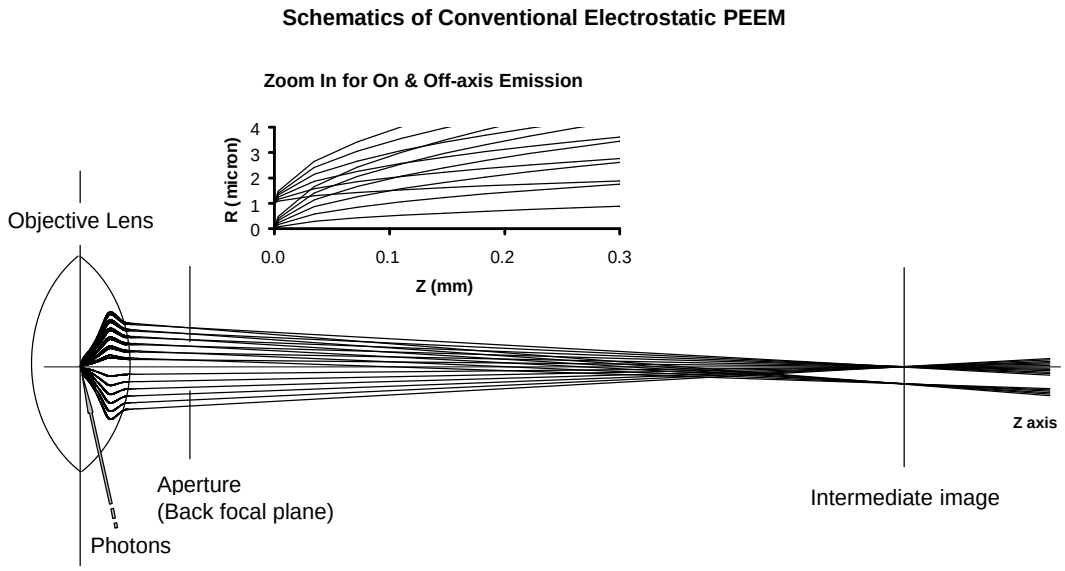

Figure 4.2: Direct ray trace of photoelectrons through objective lens with an emission energy of 0.5 eV and emission angles ranging from 0 to 0.6 radians

Figure 4.3 shows the simulated objective lens aberration spot radii as a function of emission angle for different emission energies (neglecting diffraction aberration). It indicates that if the final aberration spot size is to be kept relatively small, below say

50 nm, emission energies of less than say 1.5 eV and emission angles of less than 0.4 rad should be used. Filtering of the higher emission energies and angles is achieved through the use of a small contrast aperture. In the present context, it will be assumed that only photoelectron emission energies of 1 eV or below reach the final image.

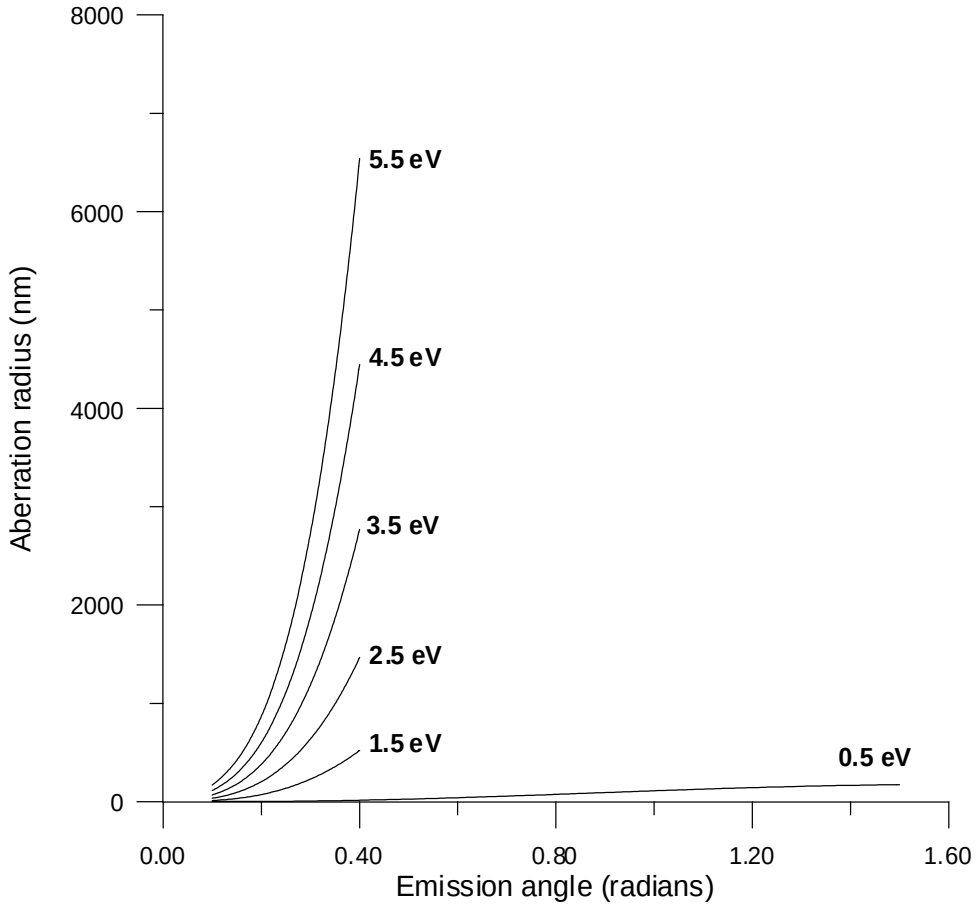

Figure 4.3: Simulated aberration spot sizes for objective lens as a function of emission angle and different emission energies

Figure 4.4 predicts how the relative transmission is reduced by variation of the aperture size. The relative numbers are calculated by the Chung-Everhart approximation of secondary electron emission [22]. The filtering effect of the aperture can be seen clearly in the figure, as the aperture reduces, narrow angle and

higher energy electrons are able to go through the aperture and contribute to the final image. Reducing the aperture size at the back focal plane is one of the most effective and simple ways to reduce image aberrations.

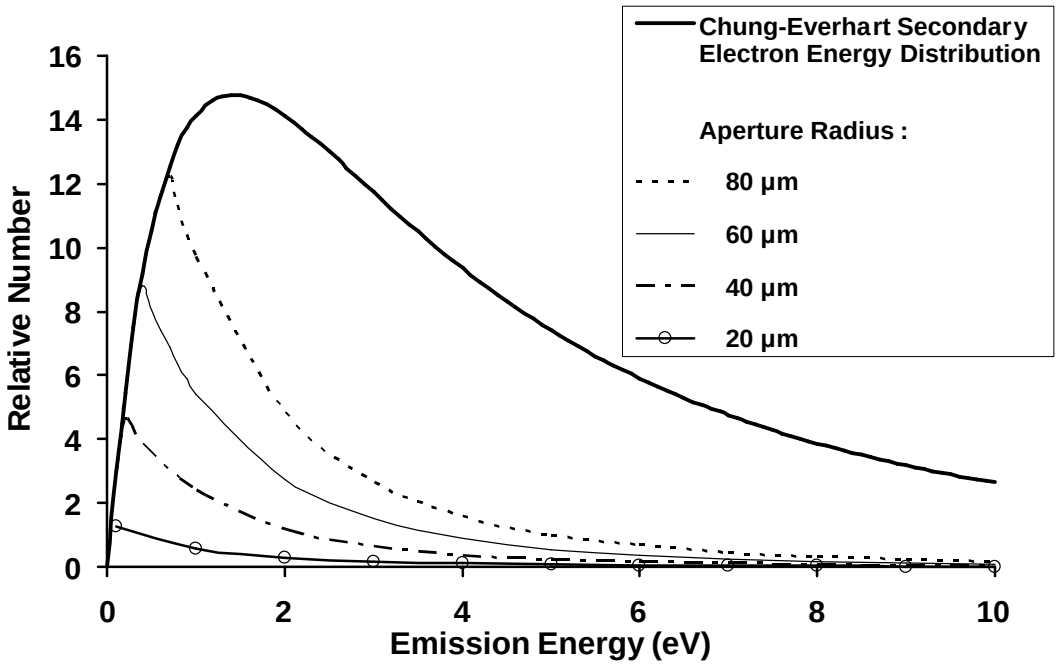

Figure 4.4: Relative transmission through contrast of varying aperture sizes

To further reduce the aberration radius, A. Khursheed has proposed to dynamically correct for chromatic aberration [9, 23], which involves the use of a drift tube to slow down a pulsed beam of electrons so that their inherent energy spread separates them, both in space and time. Once separated, either a form of energy inversion is advocated [8], or focal strength modulation of lenses within the imaging optics of the microscope is proposed [9, 23]. The general principle of this latter approach for photoemission electron microscopes (PEEMs) is illustrated in Figure 4.5.

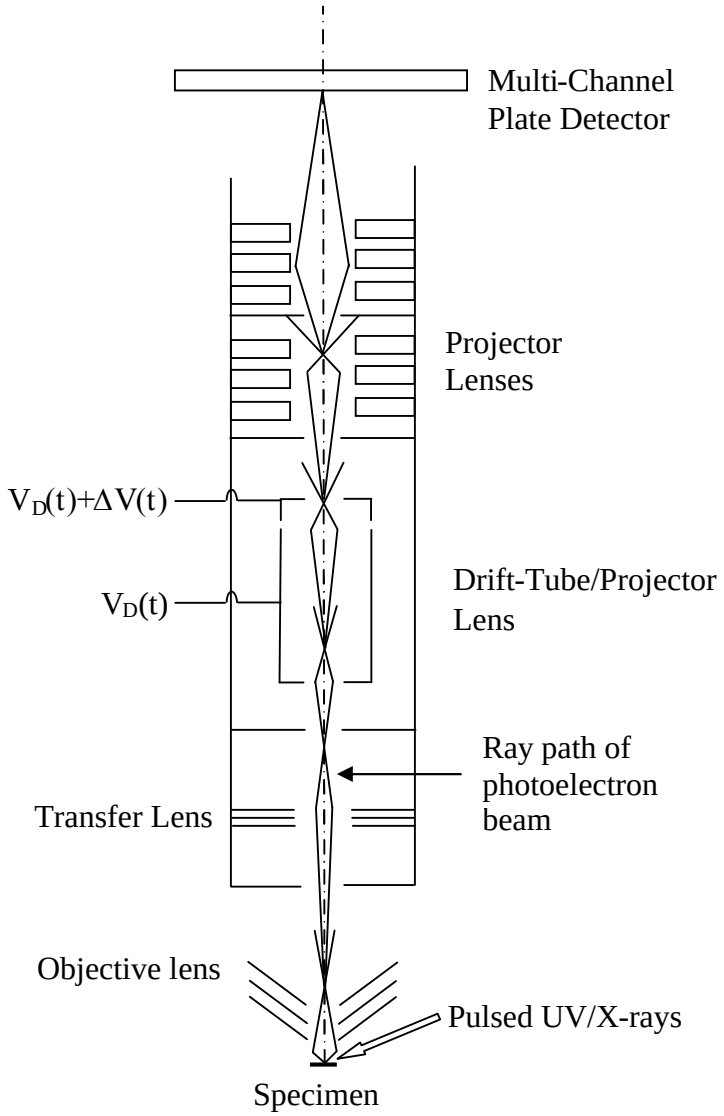

Figure 4.5: Schematic of TOFEEM chromatic aberration correction principle

The sample is irradiated with sub-nanosecond pulsed photons, and electrons emitted from the sample are focused by an objective lens, usually electrostatic. As with other PEEM systems, the photoelectron beam subsequently goes through a series of projector lenses which cast a magnified image of the specimen's surface on to an electron detector. In the chromatic aberration corrected TOFEEM shown in Figure 4.5, a transfer lens and drift-tube unit is placed after the objective lens. By varying the

voltage of an electrode suitably placed after the main part of the drift-tube, photoelectrons of differing energies can in principle be projected on to the same point, correcting for the effect of chromatic aberrations in the final image.

A time of flight PEEM system has many advantages over the conventional PEEM, even in the absence of a technique for chromatic aberration correction [7]. This is because it naturally produces the energy spectrum at its output, where images at different energies can be separated. Energy filtering in order to improve the spatial resolution is therefore easily achieved, and is much more effective than the conventional approach of using a contrast aperture in the back focal plane of the objective lens.

Before discussing the design of the drift tube, which is in the next chapter, the time-of-flight performance of the conventional PEEM objective lens and a mixed field objective lens are firstly examined assuming that chromatic aberration can be corrected for and that the aberrations of the drift tube are negligible. This assumption will be shown to be correct in the next chapter. In figure 4.6 the schematic diagram of a mixed field lens is shown. This lens is expected to have better imaging properties than the conventional PEEM.

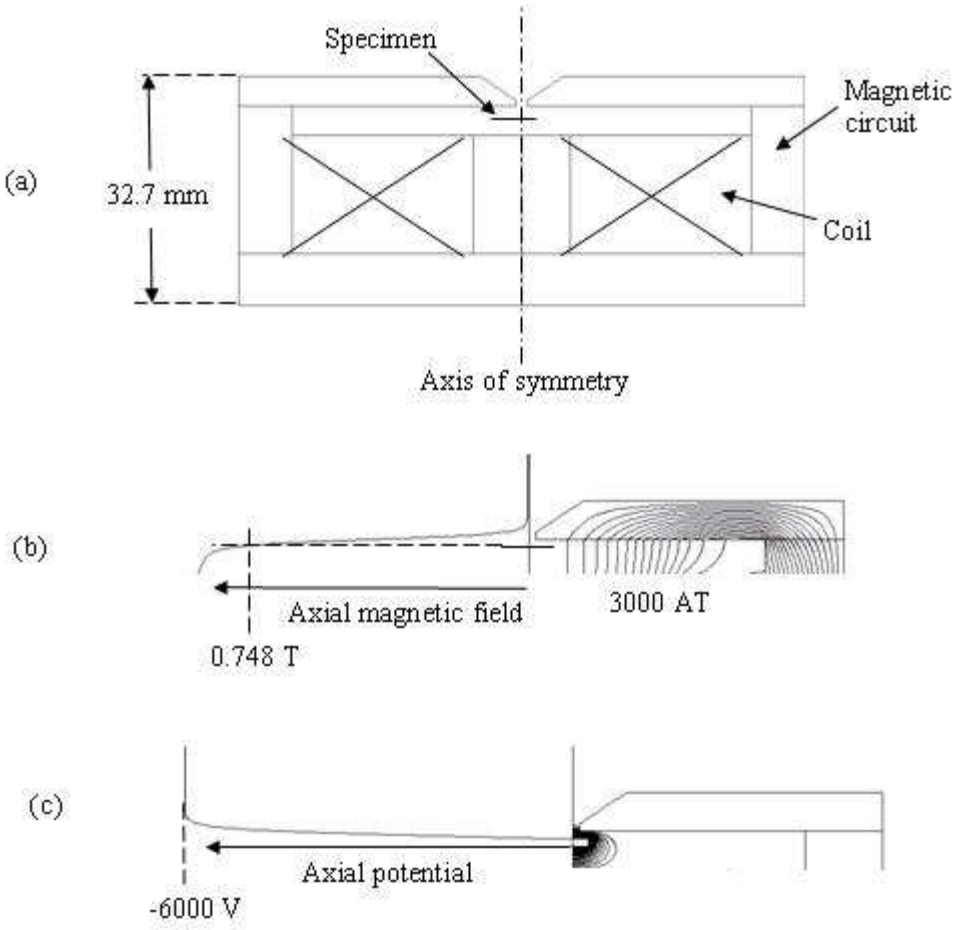

Figure 4.6: Simulated flux lines and equipotentials of a mixed field objective PEEM lens

The sample is biased at -6000V and the magnetic field there is 0.748T. The calculated magnification is 1.4 for this mixed field objective lens design. Since the focal length is very short for the mixed field lens, making it physically difficult to place an aperture near the bore, a magnetic projection lens is placed behind the mixed field objective lens as shown in Figure 4.7. This magnetic projection lens is excited so that it produces a magnetic field in the opposite direction to the objective lens, in order to reduce the presence of image rotation effects.

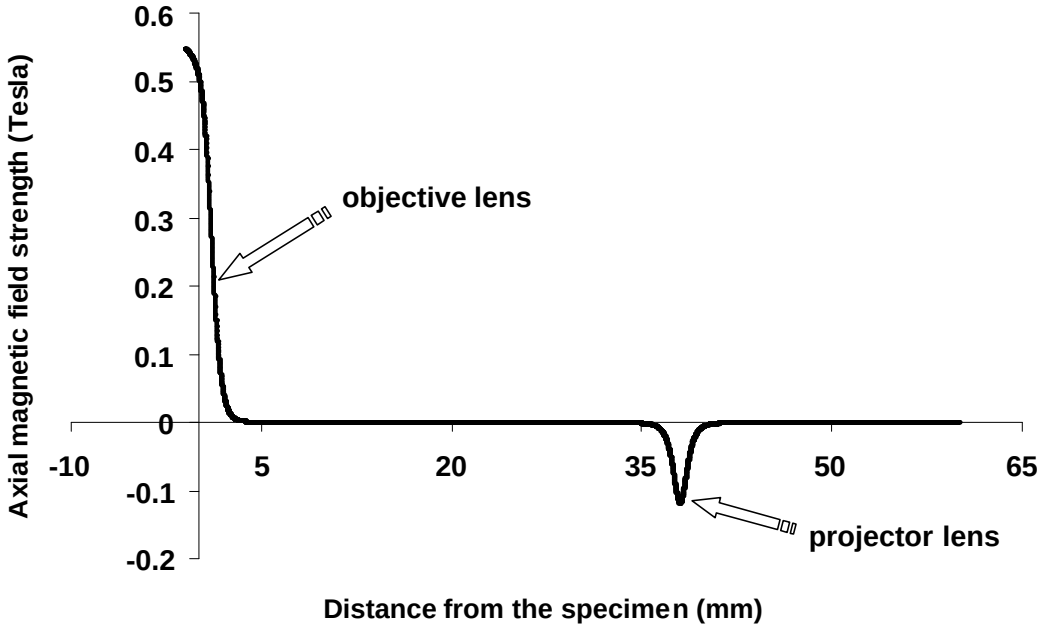

Figure 4.7: Axial magnetic field distribution for mixed field objective lens with an assumed projector lens

The projector lens was modeled by a Glaser distribution [24], a simple widely used analytical approximation to axial lens field distributions. The projector lens is designed in such way that the overall magnification for the mixed field objective lens + projector lens is 17, which is the same as the conventional electric lens. The trajectories of 0.5 eV photoelectrons leaving specimen with emission angles ranging from 0 to 0.6 radians through the mixed field are shown in Figure 4.8.

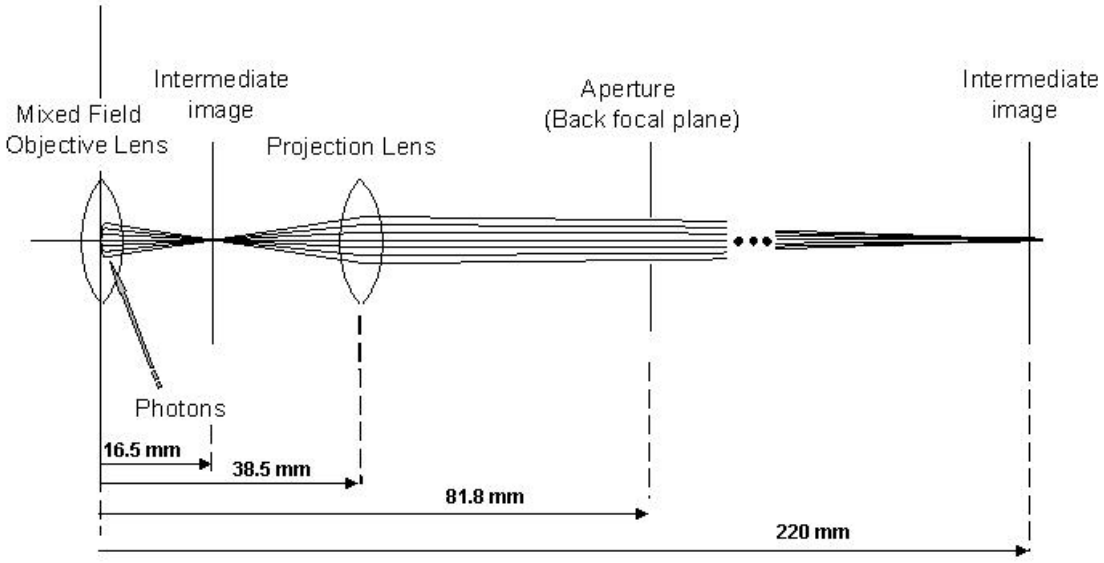

Figure 4.8: Direct ray trace through mixed field objective lens for 0.5 eV photoelectrons leaving specimen with emission angles ranging from 0 to 0.6 radians

An intermediate image is formed at 16.5mm above the specimen, which is further magnified by the negative magnetic projector lens located at 38.5mm. An aperture is placed at the back focal plane of the projector lens around 81.8mm. The final image with magnification of 17 times is formed 220mm from the specimen. The emission angle and energy filtering effect of the aperture are shown in Figure 4.9.

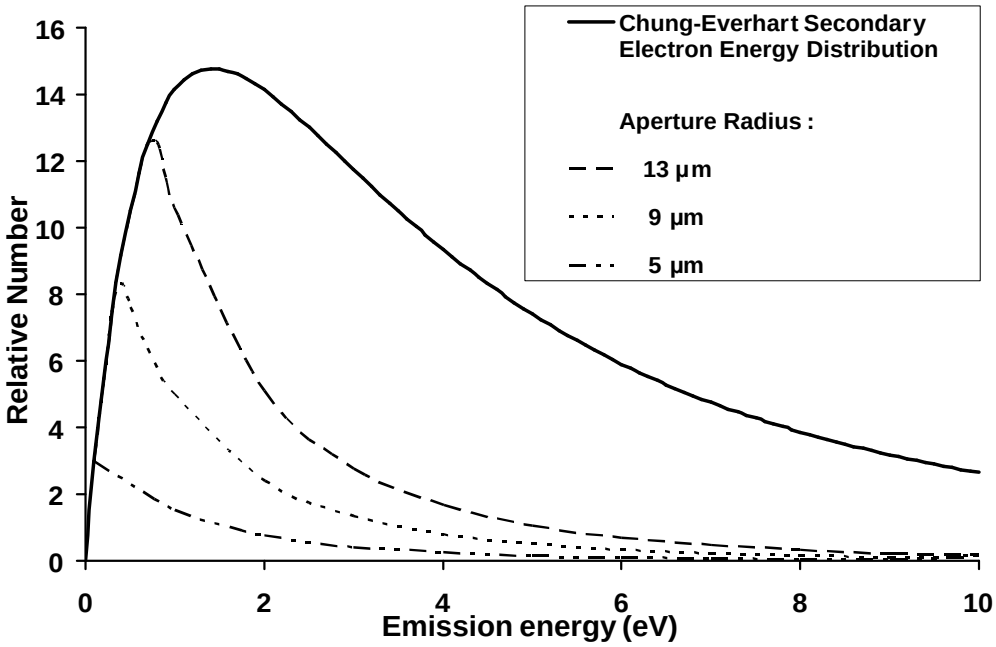

Figure 4.9: Relative transmission through contrast of varying aperture sizes for mixed field objective lens

Similar to that of the conventional electric lens, both angular and energy filtering effects are observed for smaller aperture radius, which will reduce both spherical and chromatic aberrations.

In the mixed field objective lens, the magnetic field will cause the electrons to spiral around the z-axis, which may degrade the resolution of the final image if it is dependent on emission energy. As already stated, the projector magnetic field is made negative, deliberately to reduce image rotation effect; this is indicated by simulations as shown in Figure 4.10.

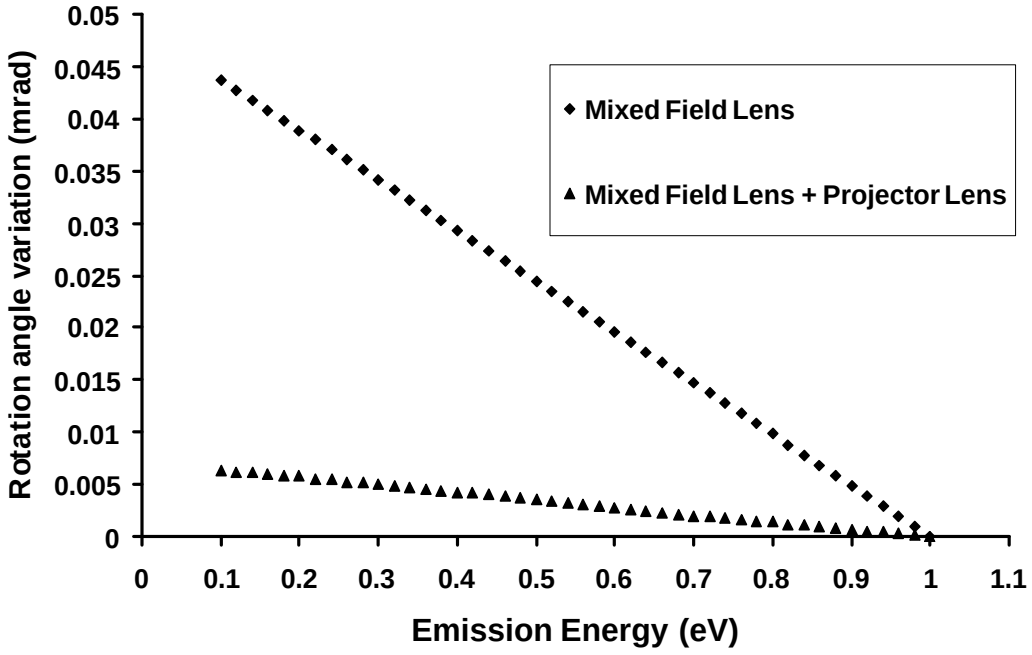

Figure 4.10: Image rotation spread for parallel one micron off-axis trajectories, relative to 1 eV trajectory

The image blur due to rotation is typically less 1 μm × 0.006 mrad = 0.006 nm for mixed field lens + projector lens, which can be ignored, and it is less than 0.045 nm for the mixed field lens alone. The reason for it being low despite having a magnetic field is that the photoelectrons are strongly accelerated from the specimen.

In TOFEEM, images formed by electrons with different emission energies ranging from 0.1eV to 0.2eV in width, will be added up to get the final image using image processing software. The predicted aberration spot diameter as a function of the aperture radius is shown in figure 4.11.

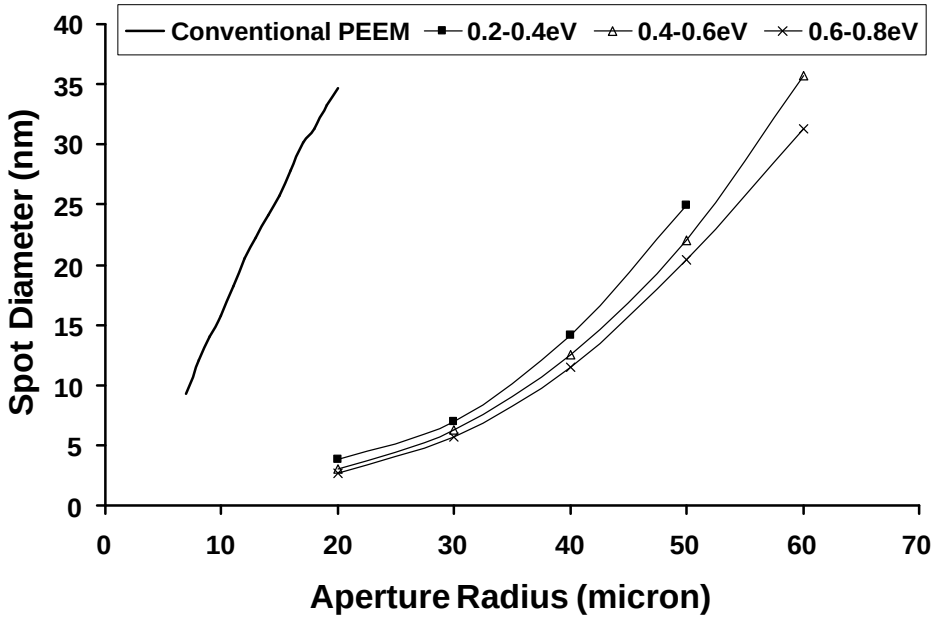

(a)

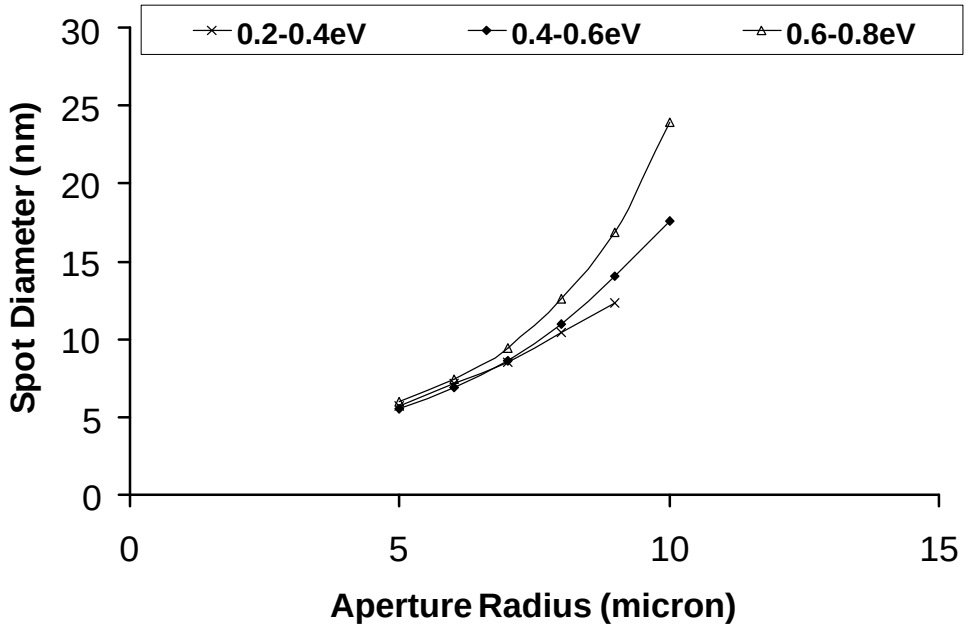

Figure 4.11: Simulated aberration probe sizes as a function of contrast aperture radius

(a) Conventional PEEM electric objective lens

(b) Mixed field objective lens

The simulation results shown in figure 4.11 were calculated by 15,500 trajectories ranging from 0 to 10 eV emission energies and 0 to 1.5 radian emission angles. Due to the shorter focal length of the mixed field lens, it requires smaller aperture sizes. As expected, smaller apertures provide greater angular and energy filtering, reducing aberrations, but it comes at the price of reducing transmission (output signal-to-noise). The aberration spot diameter as a function of the transmission rate for both lenses is shown on figure 4.12. It is assumed that the final image can be formed from different emission energy ranges, which can also be summed together to increase the total collected current.

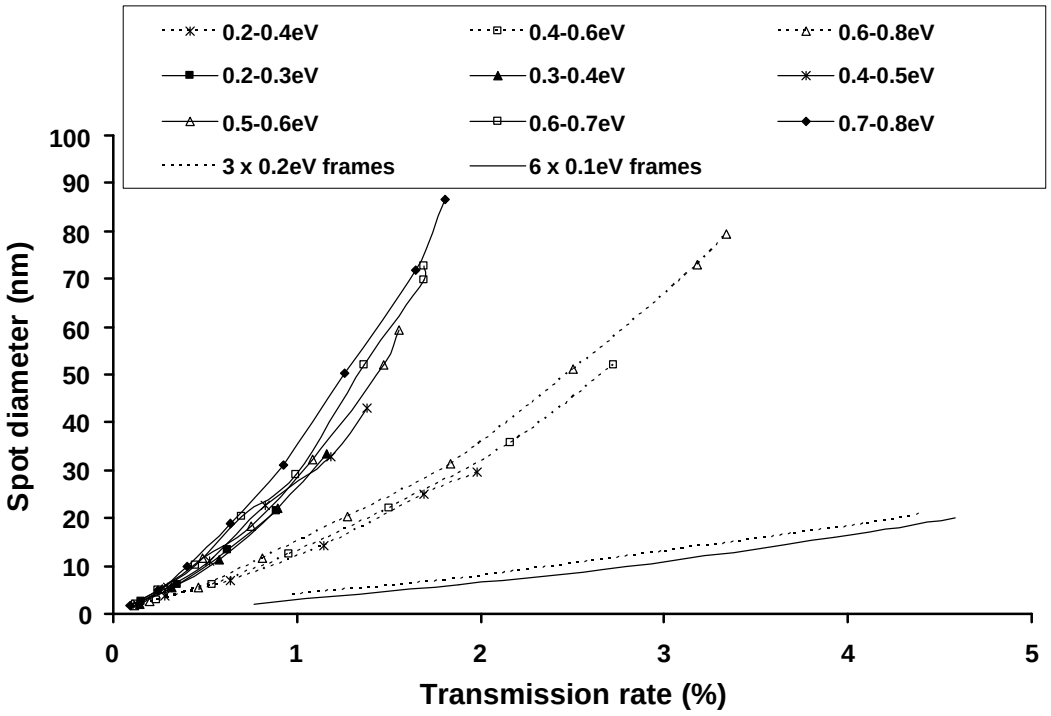

(a)

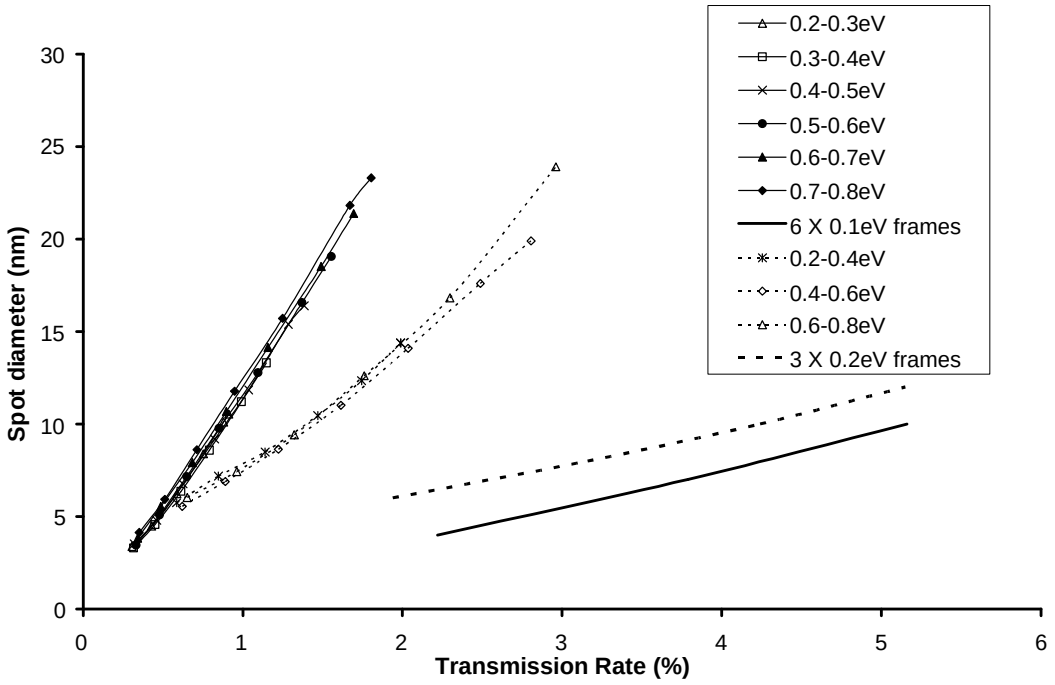

(b)

Figure 4.12: Simulated aberration spot as a function of percentage transmission for PEEM objective lens as energy width is varied from 0.2 to 0.1 eV
(a) Conventional electric lens
(b) Mixed field lens

It is assumed here that the final image can be separately focused within each energy range and that the images can be then added together, corresponding to the action of correcting for chromatic aberration. Figure 4.12a shows that for conventional lens, there is little difference between the energy widths of 0.1 and 0.2 eV, so wider energy widths can be used, requiring less precision in signal correction. On the other hand, there is around 20-30% improvement in the predicted aberration spot size for the mixed field objective lens by using 0.1eV widths instead of 0.2eV widths.

The foregoing simulation assumes that a pulsed source is especially designed to have the same average current as continuous sources; such sources have been proposed for electron microscopy [25].

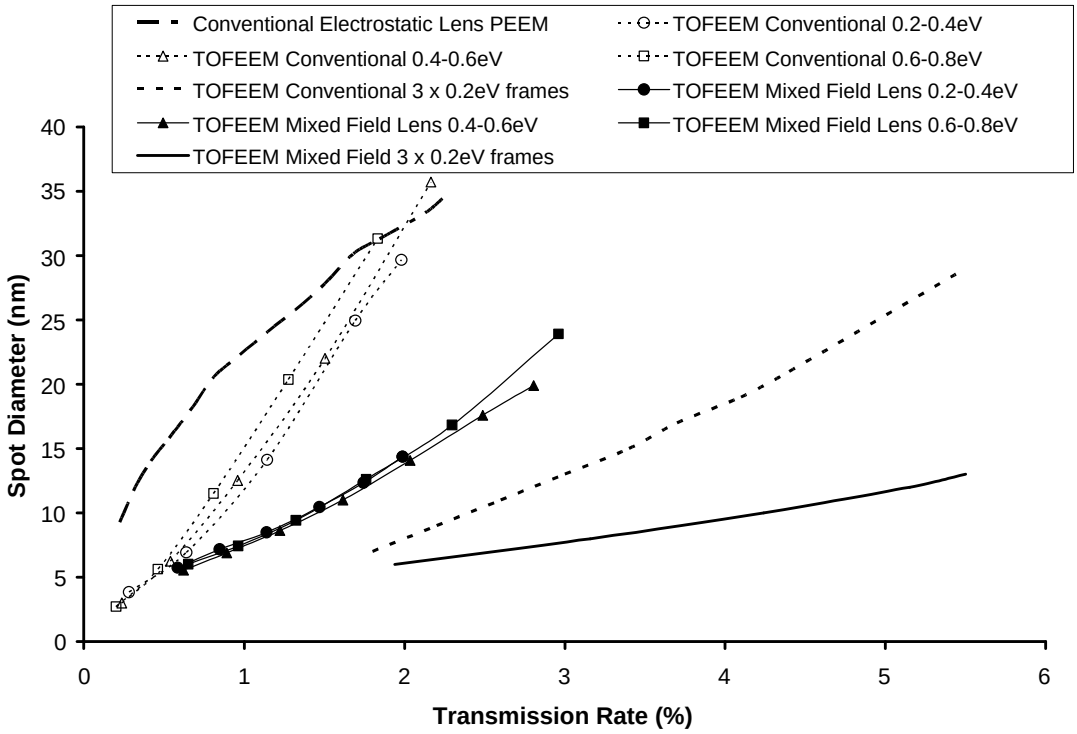

Figure 4.13: Simulated aberration spot as a function of percentage transmission

We can see in figure 4.13 that the performance of TOFEEM is better than conventional PEEM. With aberration correction for the mixed field lens, around 4 nm spot diameter is predicted at 2% transmission rate, similar to the estimated prediction by Wan et al for that of a tetrode mirror method [11]. Note this improvement is for an assumed effective energy width of 200 meV, much larger than the effective energy widths predicted after aberration correction (less than 50 meV).

For the mixed field objective lens, it is application is limited for non-ferromagnetic samples only, for this reason we will design the drift tube to correct the chromatic aberration dynamically for the conventional electric lens. In the present context, we note that the mixed field lens is predicted to provide a significantly better image resolution than the conventional electric field lens.

CHAPTER 5

Drift tube design for chromatic aberration correction

Dynamic correction for chromatic aberration TOFEEM proposed by A.Khursheed [9, 23] has already been described in chapter 4 and the most recent TOFEEM design was shown in figure 4.5. In a previous TOFEEM design, a separate corrector lens placed after the drift-tube was proposed. The correction lens chromatic aberrations were calculated as a function of the potential on its central electrode, and conditions for canceling the objective lens chromatic aberrations were found [26]. In this chapter, a simpler approach is proposed. The exit part of the drift-tube is detached from its main body, and a small correction voltage ΔV is applied to it, as shown in Figure 4.5. In this way, large changes in the exit focal position can be made via relatively small correction voltages. This chapter demonstrates how such a drift-tube design can be used to correct for chromatic aberration in the TOFEEM. In the drift-tube, Coulomb interactions may be important since the photoelectrons travel very slowly, on the other hand, they are quite dispersed and density is low. Future work needs to be carried out to determine how important they are. In the present work, they are neglected.

5.1 Simulation of on-axis aberrations

A conventional electrostatic objective lens design is used as shown in Figure 4.1, since it is able to image the surface of both ferromagnetic and non-ferromagnetic samples. Figure 5.1 depicts equipotential lines for the drift-tube.

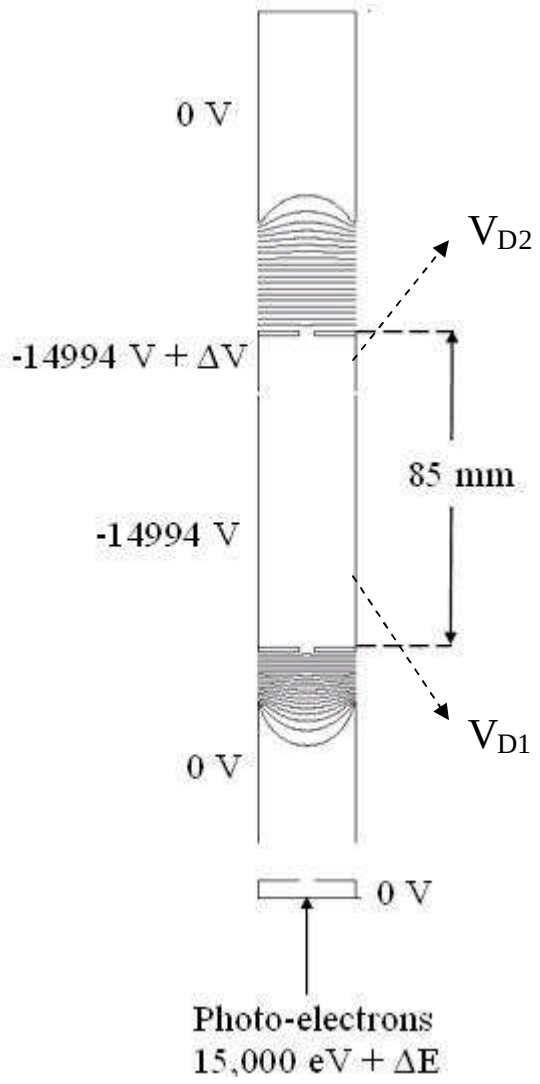

Figure 5.1: Equipotential lines for drift-tube electric field solution

The drift-tube has 10 mm diameter holes at its ends, and is biased to allow for a 6 eV pass energy. The chromatic effect of ΔE, the emission energy, is directly corrected for by changing an electrode voltage ΔV at the top of the drift-tube. The drift-tube acts as a combination of two lenses, a retarding field lens at its entrance, and an accelerating lens at its exit. The projected focal point into the drift-tube is carefully selected so that angular dispersion on the low emission energies is minimized. Figure 5.2a shows direct ray tracing of photoelectrons through the drift-tube that leave the specimen with an emission energy of 0.1 eV and emission angles ranging from 0 to 0.2 radians (for an objective lens magnification of 17). The projected focal point into the drift-tube as they enter it is 60 mm, which gives a demagnification factor of around 2.36, leaving an overall magnification factor of 7.2 at the drift-tube exit. In Figure 5.2b, 5.2c, 5.2d and 5.2e, trajectory paths for 0.5, 0.9, 3, and 5 eV emission photoelectrons are traced through the drift tube for emission angles 0 to 0.2 radians. They undergo more demagnification than the 0.1 eV emitted photoelectrons when the emission energy increases. The overall magnification will reach unity for 5 eV emission photoelectrons. Variation of the magnification with emission energy has already been reported for TOFEEM [8], and since a series of images are captured in time, where each image is formed over a different emission energy range, they can be stored in software form and suitably resized before being added together.

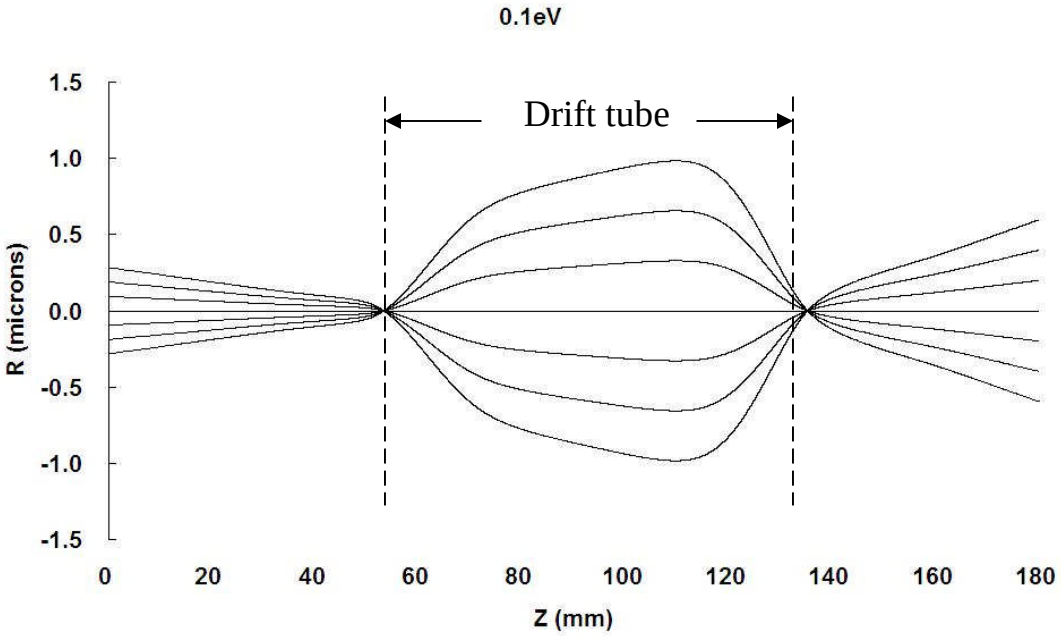
0.1eV
Drift tube
R (microns)
Z (mm)
1.5
1.0
0.5
0.0
-0.5
-1.0
-1.5
0
20
40
60
80
100
120
140
160
180

(a)

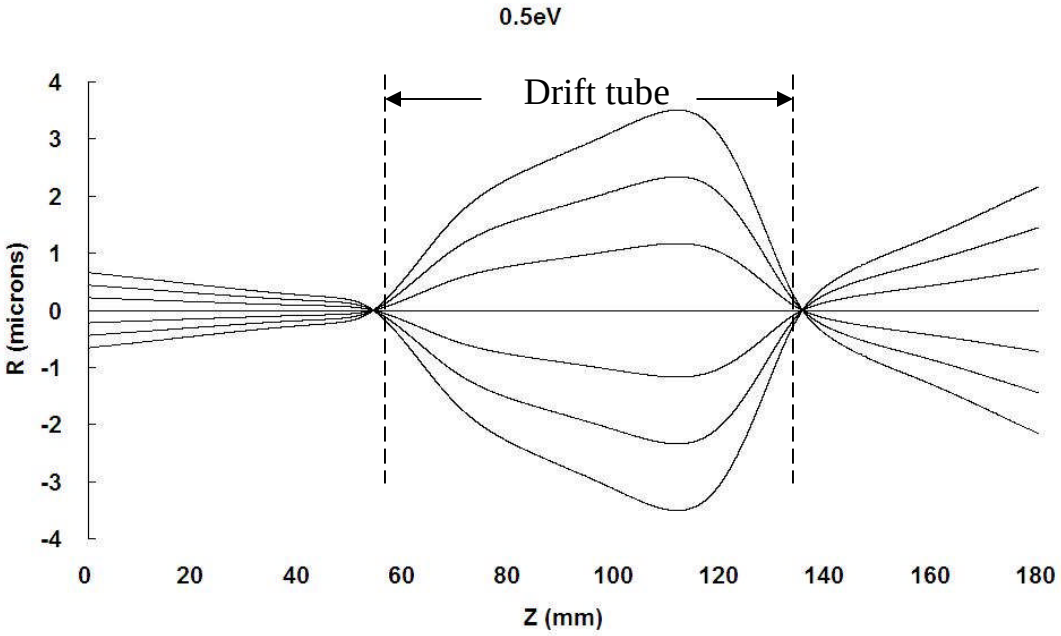
0.5eV
Drift tube
R (microns)
Z (mm)
4
3
2
1
0
-1
-2
-3
-4
0
20
40
60
80
100
120
140
160
180

(b)

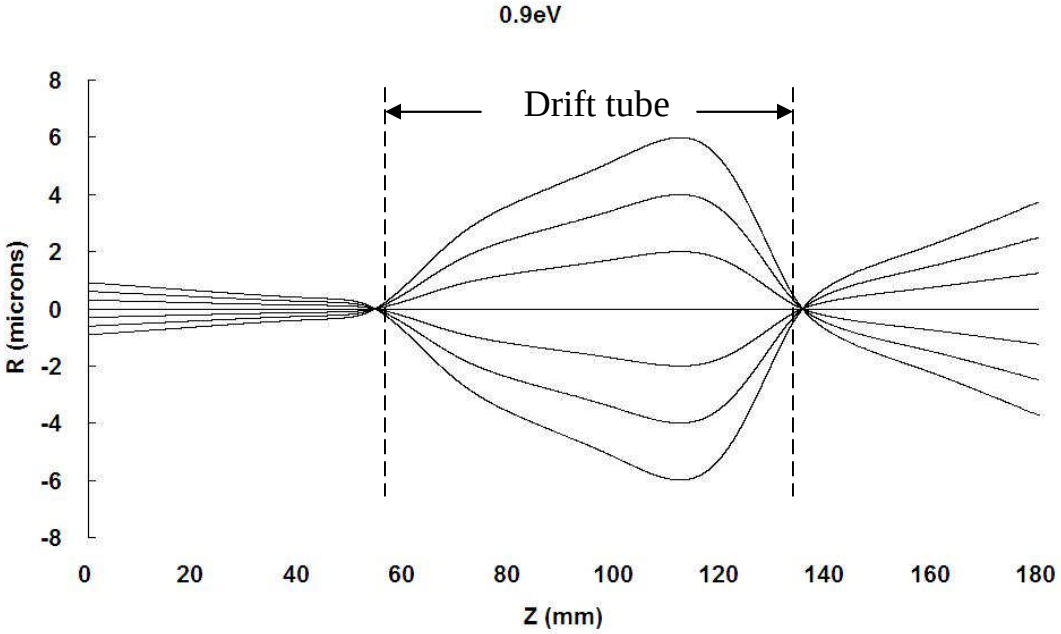
0.9eV
Drift tube
R (microns)
Z (mm)
8
6
4
2
0
-2
-4
-6
-8
0
20
40
60
80
100
120
140
160
180

(c)

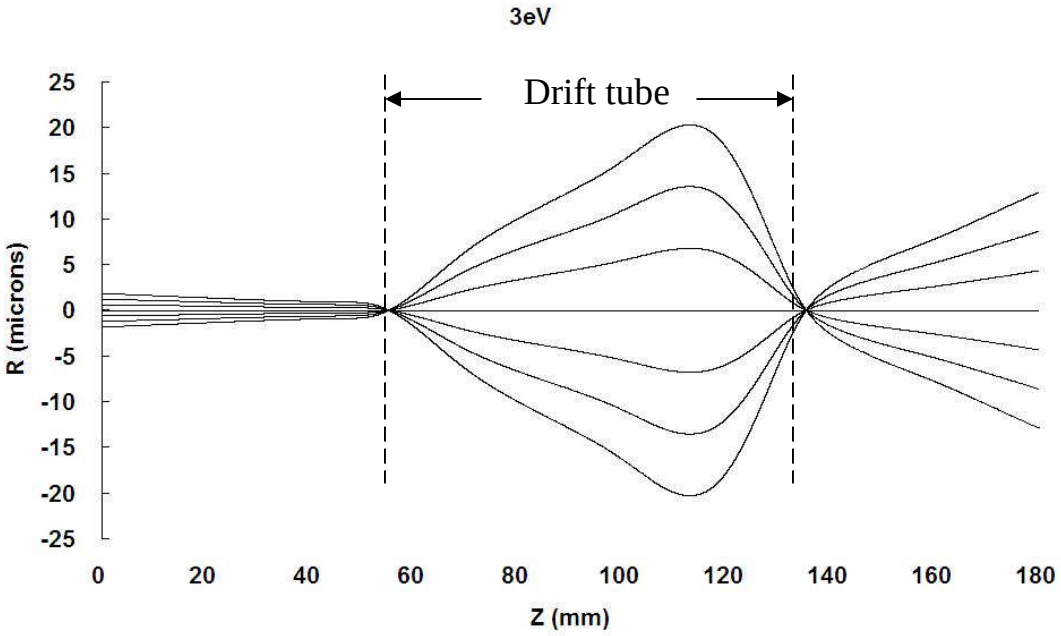
3eV
Drift tube
R (microns)
Z (mm)
25
20
15
10
5
0
-5
-10
-15
-20
-25
0
20
40
60
80
100
120
140
160
180

(d)

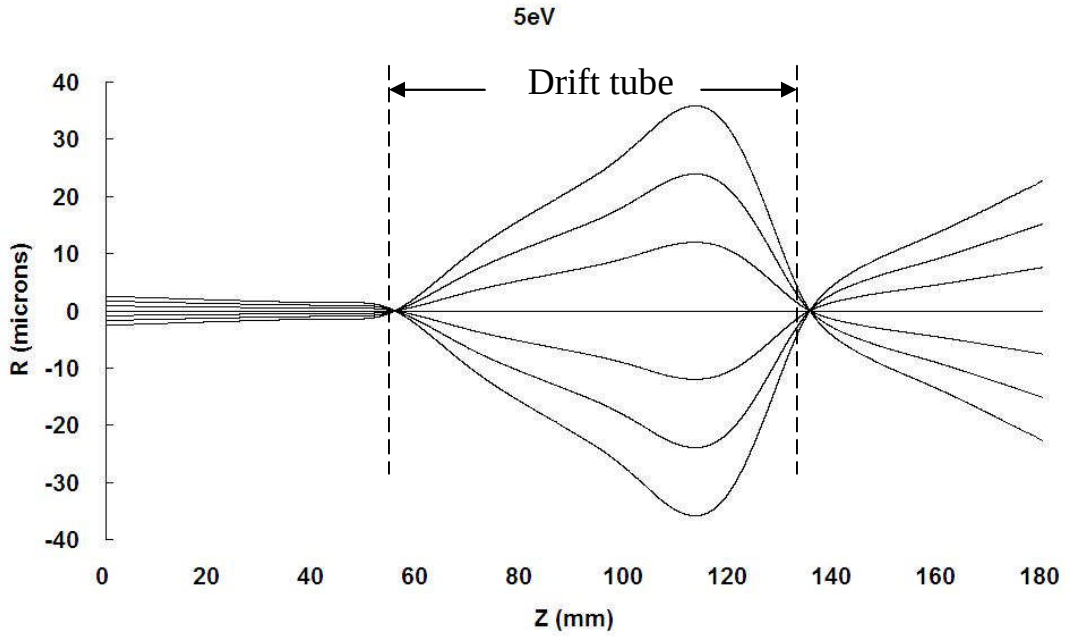

(e)

Figure 5.2: Direct ray tracing of photoelectrons through drift-tube that leave the specimen with emission angles ranging from 0 to 0.2 radians
(a) Emission energy of 0.1 eV and $\Delta V = 0$
(b) Emission energy of 0.5 eV and $\Delta V = =1$ V
(c) Emission energy of 0.9 eV and $\Delta V = =1.6$ V
(d) Emission energy of 3 eV and $\Delta V = =4$ V
(e) Emission energy of 5 eV and $\Delta V = =6.2$ V

Figure 5.3 shows the variation in drift-tube exit focal position as a function of emission energy and correction voltage ΔV for an emission angle of 0.1 radians. It illustrates how changes in ΔV can be used to compensate for the combined chromatic aberration of objective and drift-tube lenses. For instance, to keep the focal exit position constant as the emission energy changes from 0.1 to 0.5 eV, ΔV must change from 0 to -1 V.

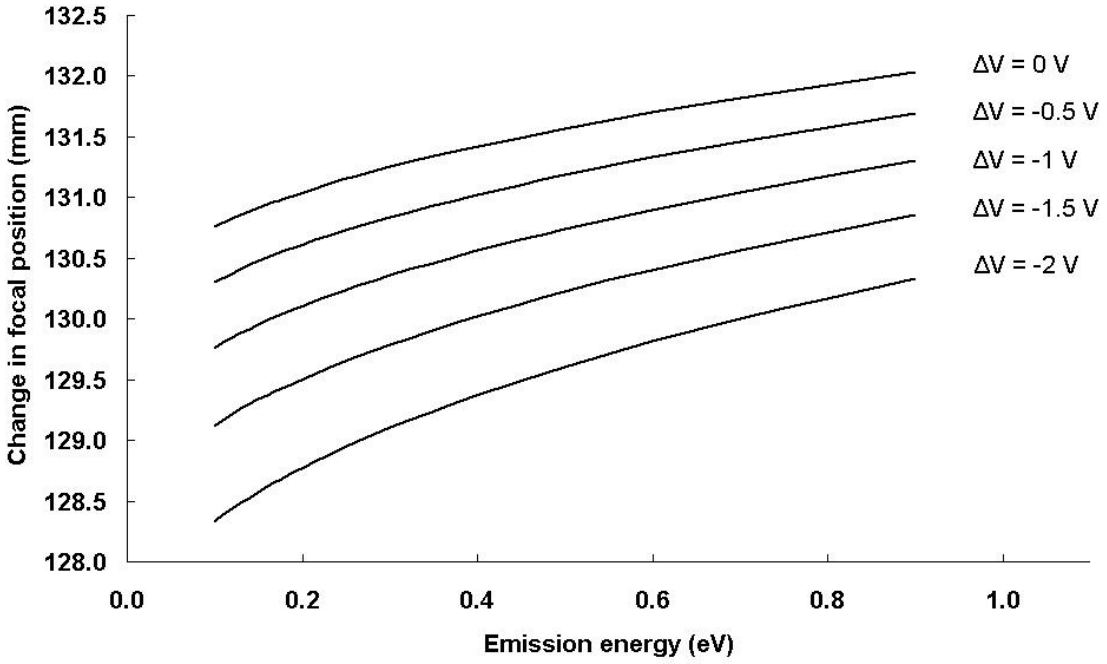

Figure 5.3: Simulated drift-tube exit focal point variation as a function of emission energy and changes in ΔV

Figure 5.4 shows the simulated time dispersion characteristics of the drift-tube: photoelectrons emitted with energies of 0.1 eV arrive at the top of the drift-tube 0.5 ns earlier than the 0.5 eV ones. This means that ΔV must change by -1 V in 0.5 ns in order to compensate for the chromatic aberration of the 0.5 eV photo-electrons (relative to the 0.1 eV photo-electrons), a rate quite achievable by standard signal generators. Figure 5.4 also shows that the correction signal can be well approximated by a triangular ramp waveform. Note that the time-dispersion related to ΔV changing from 0 to -1 V is relatively small compared to the dispersion generated within the main body of the drift-tube and can be readily taken into account when generating the required correction signal.

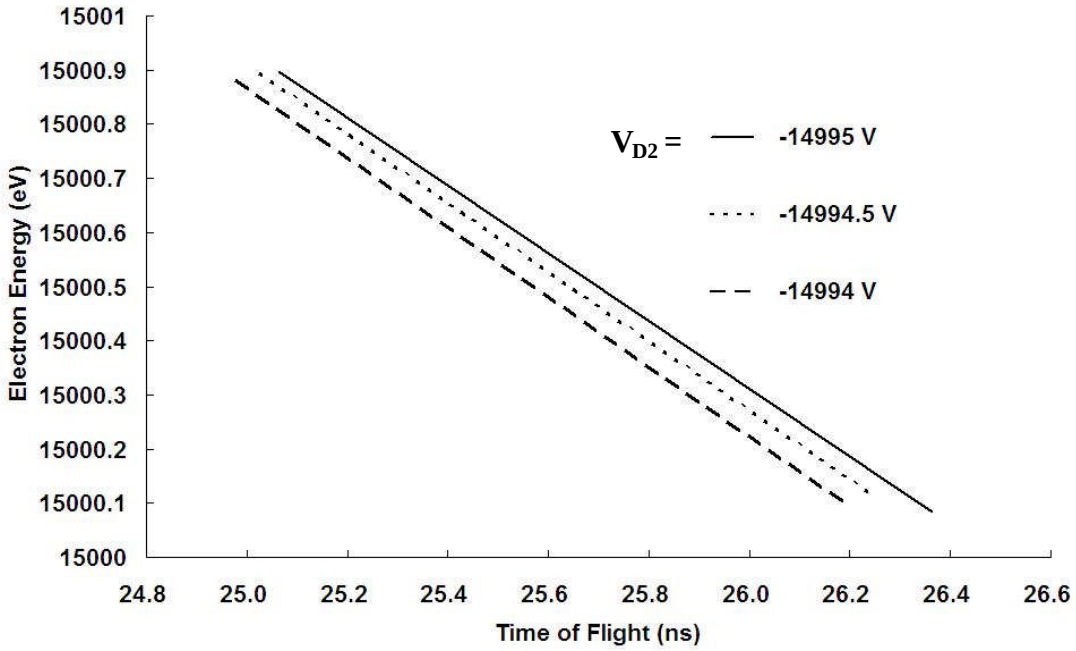

Figure 5.4: Simulated time-dispersion characteristics of the drift-tube as a function of input kinetic energy

Figure 5.5 shows the correction voltage of the second portion of the drift tube as a function of the time of flight of the photoelectrons in the drift tube until the end of the first portion of the drift tube. It is a linear variation with slope of 2V/ns.

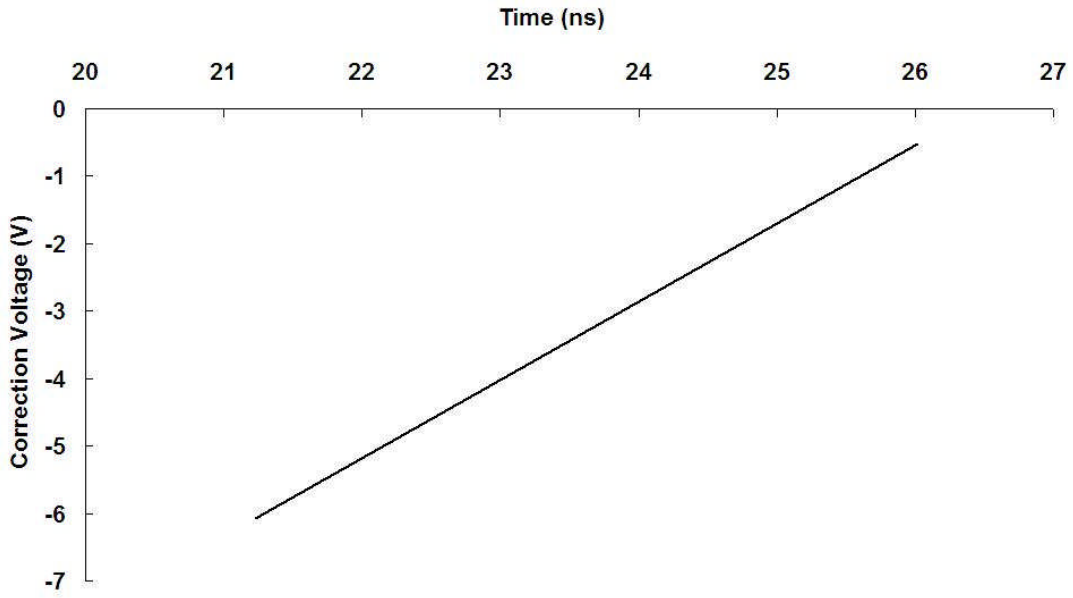

Figure 5.5: Simulated correction voltage of the drift-tube as a function of time of flight of the photoelectrons

The spherical aberration of the drift-tube on the final image is expected to be small since photoelectrons travel through it with relatively small angles (less than 1 mrad). Wide-angle photoelectrons can be filtered out by using a small contrast aperture. Figures 5.6a to 5.6e present simulated spherical aberration spot radii for the combined objective lens and drift-tube at emission energies of 0.1 to 5 eV. They show that for emission energies of 0.1 eV, 0.5 eV and 0.9 eV, there is very little additional influence of the drift-tube. For the 3 and 5 eV emission energy, although the drift-tube aberrations have a greater effect, they are still relatively small, particularly as the wider-angle photoelectrons will be eliminated by the contrast aperture.

ΔE = 0.1 eV, V_{D2} = -14994 V

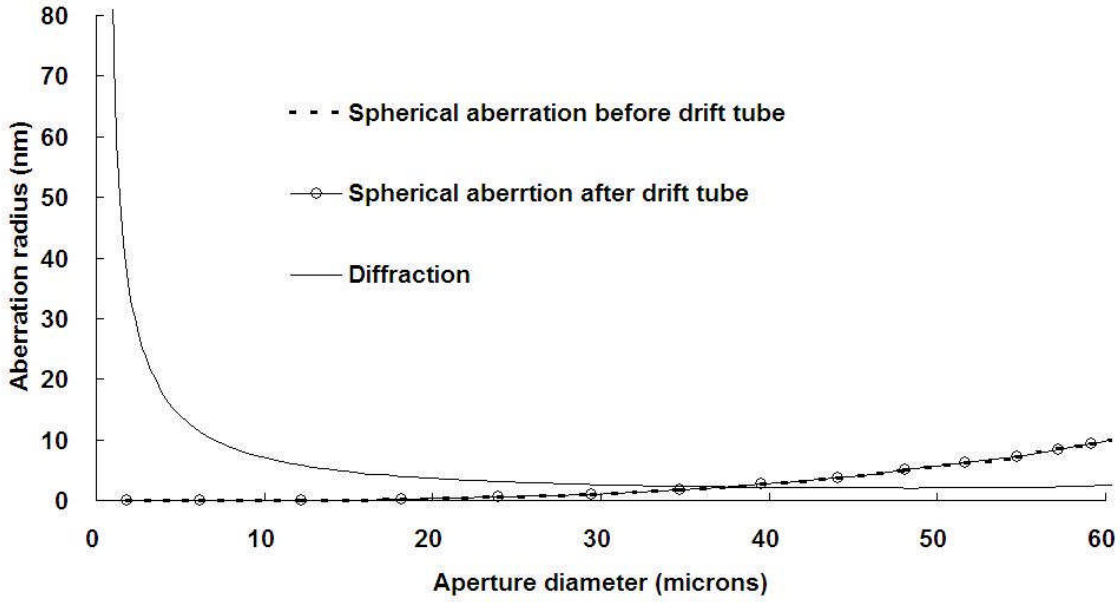

(a)

ΔE = 0.5 eV, V_{D2} = -14995 V

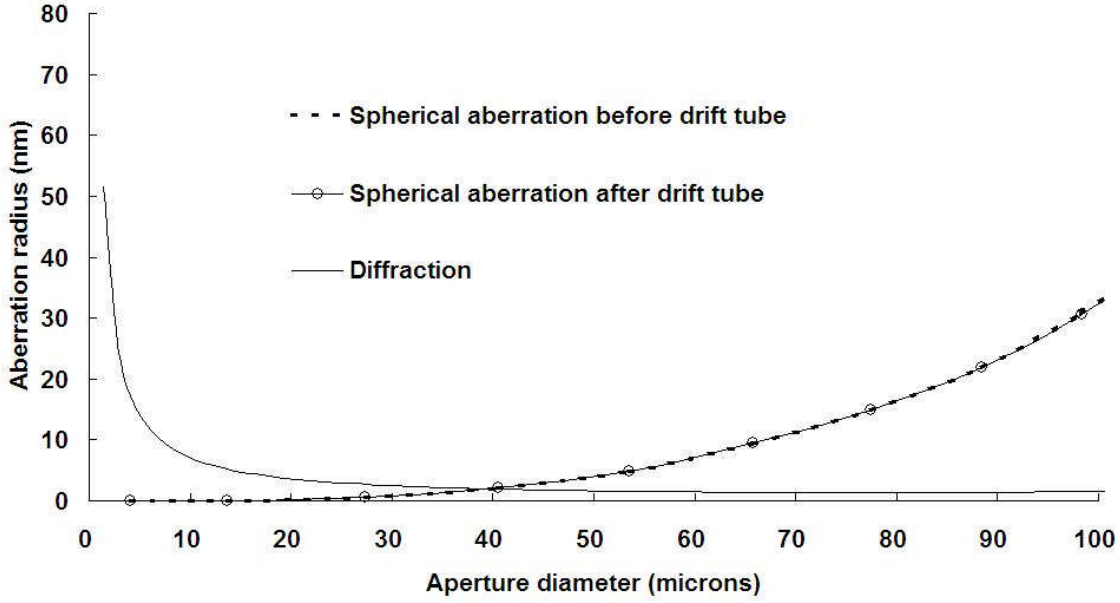

(b)

ΔE = 0.9 eV, V_{D2} = -14995.6 V

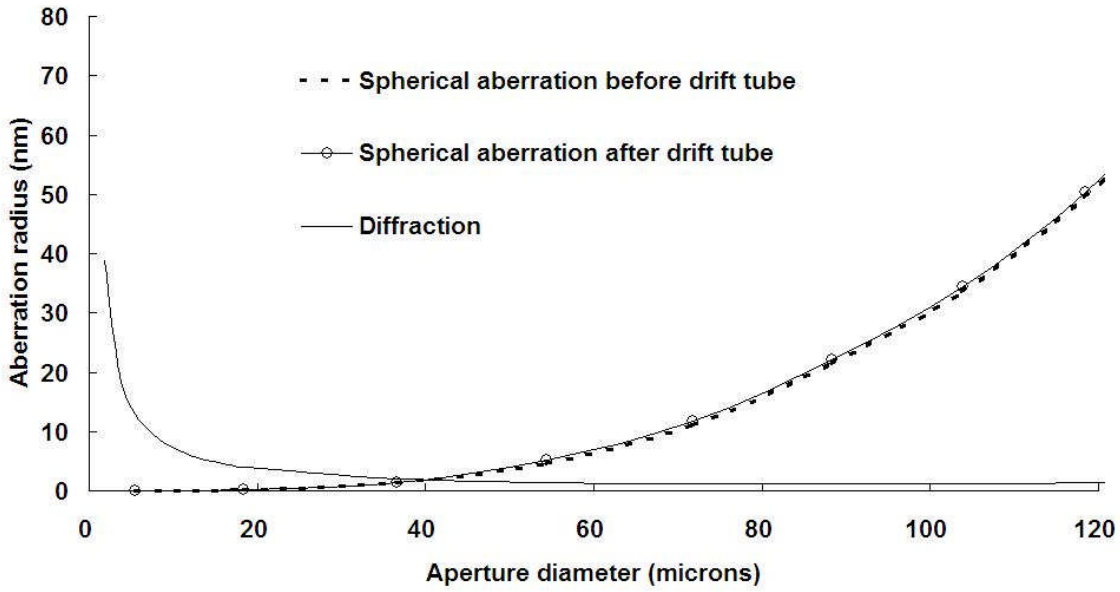

(c)

ΔE = 3 eV, V_{D2} = -14998 V

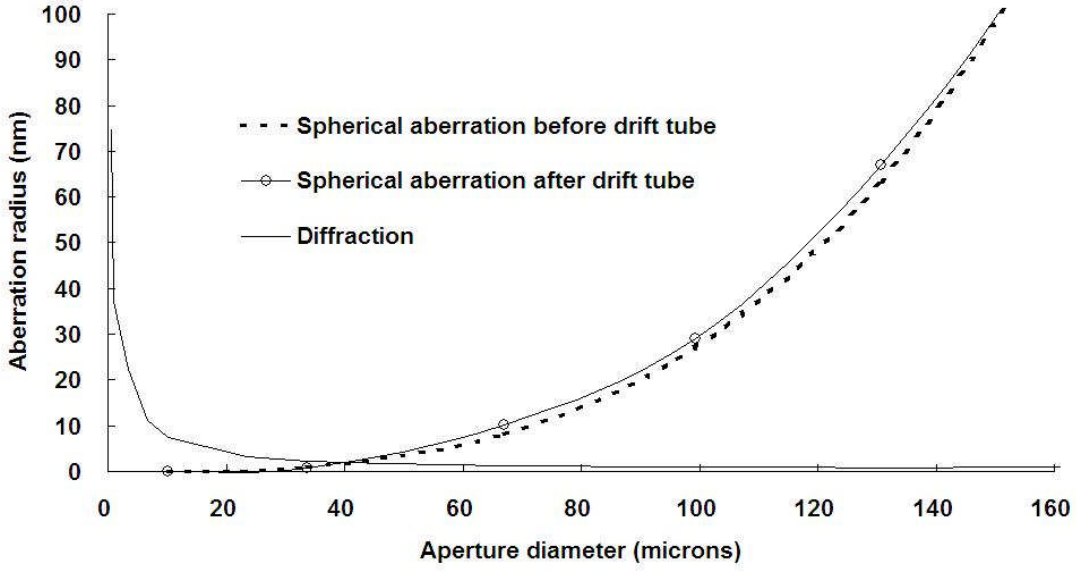

(d)

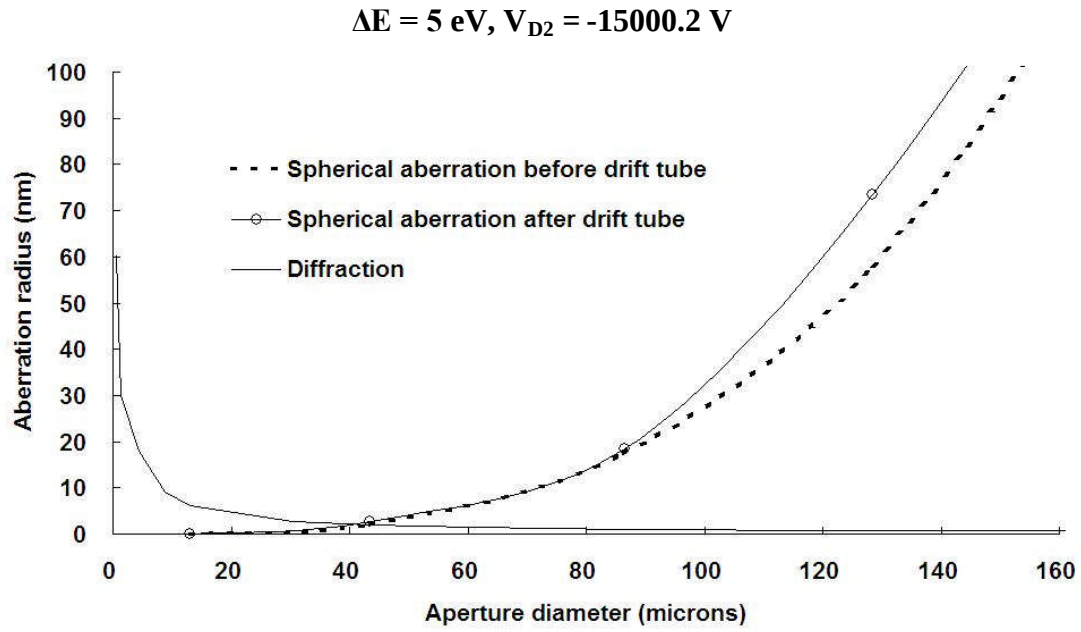

(e)

Figure 5.6: Simulated spherical aberration radius at drift-tube exit
(a) Emission energy of 0.1 eV and ΔV = 0
(b) Emission energy of 0.5 eV and ΔV = -1 V
(c) Emission energy of 0.9 eV and ΔV = -1.6 V
(d) Emission energy of 3 eV and ΔV = 4 V
(e) Emission energy of 5 eV and ΔV = 6.2 V

From Figure 5.6 we can see that a contrast aperture with diameter of 40 μm can make the total aberration radius less than 10 nm. This is a great improvement over conventional PEEM, where a 40 μm aperture provides 70 nm predicted on-axis resolution (Figure 4.11a). These results indicate that the dynamic correction of chromatic aberration is expected to improve the on-axis resolution by approximately a factor of 7, consistent with the results presented in Chapter 4. The results presented in this section have also proved the assumption made in Chapter 4 that the drift-tube spherical aberration is relatively low, and can be neglected.

5.2 Simulation of off-axis aberrations

In the previous section, reduction of on-axis aberrations through dynamic correction of chromatic aberration was analyzed. The results predict that there should be significant improvement. However, the off-axis aberrations also need to be simulated, since the field of view in the final image is limited by off-axis aberrations, which are expected to increase with introduction of the drift-tube.

In this section, direct ray tracing of electrons starting off-axis on the specimen, emitted over a range of angles is used to estimate the field of view in the final image. Emission angles ranged from 0 to 0.4 radians for 0.5 eV. The results were calculated in the form of spot diagrams in the final image. Each spot in the final image comes from point emission at the specimen.

Spot diagrams for 0.5eV on-axis electrons are shown in Figure 5.7. Both spot diagrams consist of two rings. The outer ring is defined by all electrons that pass though the contrast aperture at the back focal plane, which is 40 μm in diameter in this case. The inner ring is 50% of the current that passes through the aperture, which is taken here to represent the spot size. This method has been used by Barth and Kruit [27]. The results are consistent with Figure 5.6b. The spherical aberration before and after the drift tube are almost the same, both are around 4nm in diameter, which means the drift tube's influence for the on-axis electrons can be neglected.

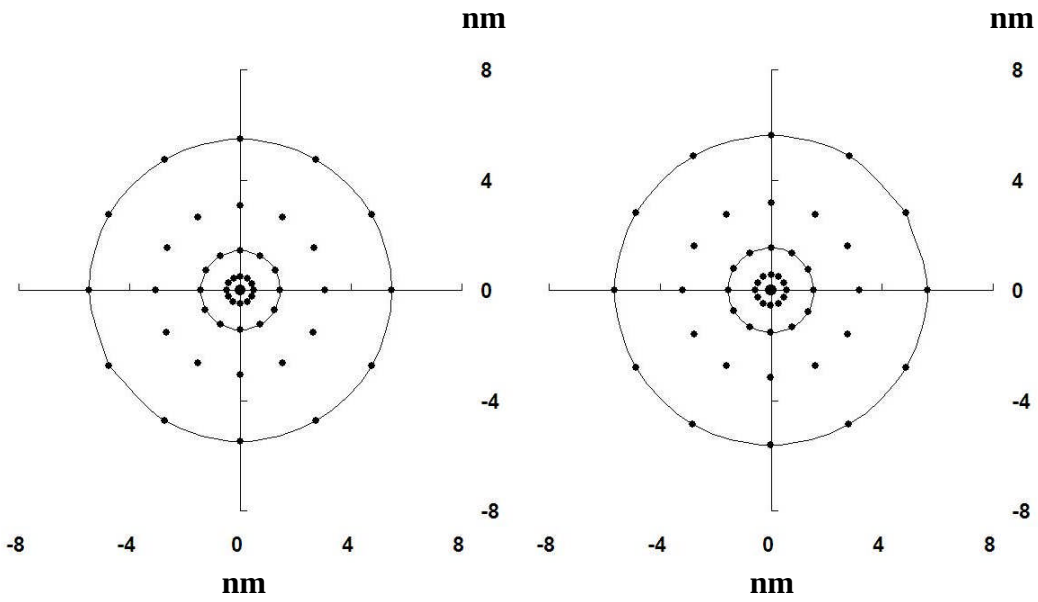

Figure 5.7: Spot diagrams for 0.5eV on-axis electrons
(a) Before the drift tube
(b) After the drift tube

The off-axis performance of the drift tube can also be checked by the spot diagram. For an aperture of 40 μm in diameter at the back focal plane, the simulated spot diagram before and after the drift tube is shown in Figure 5.8.

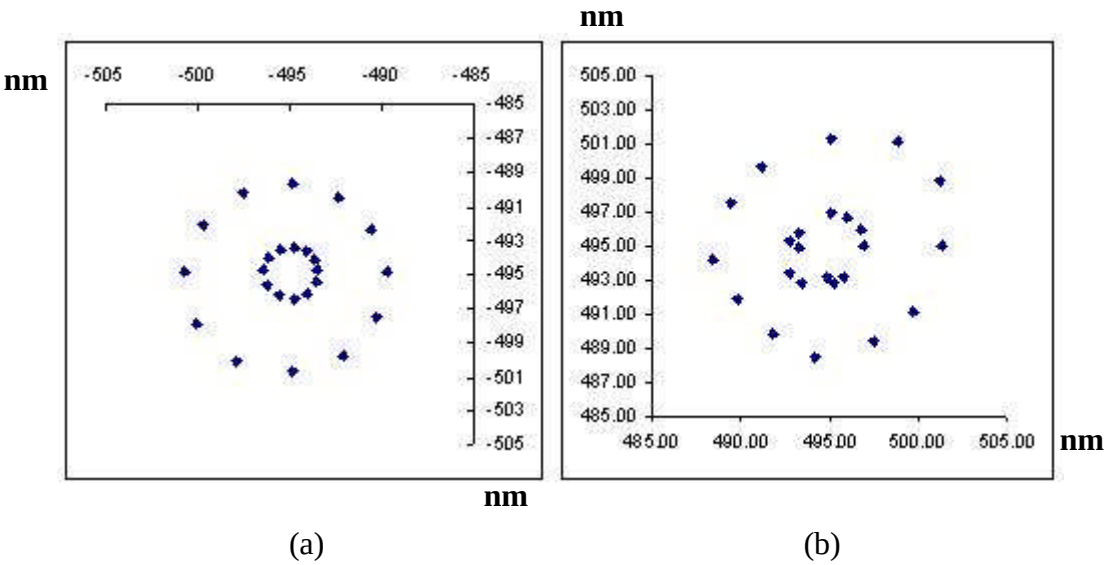

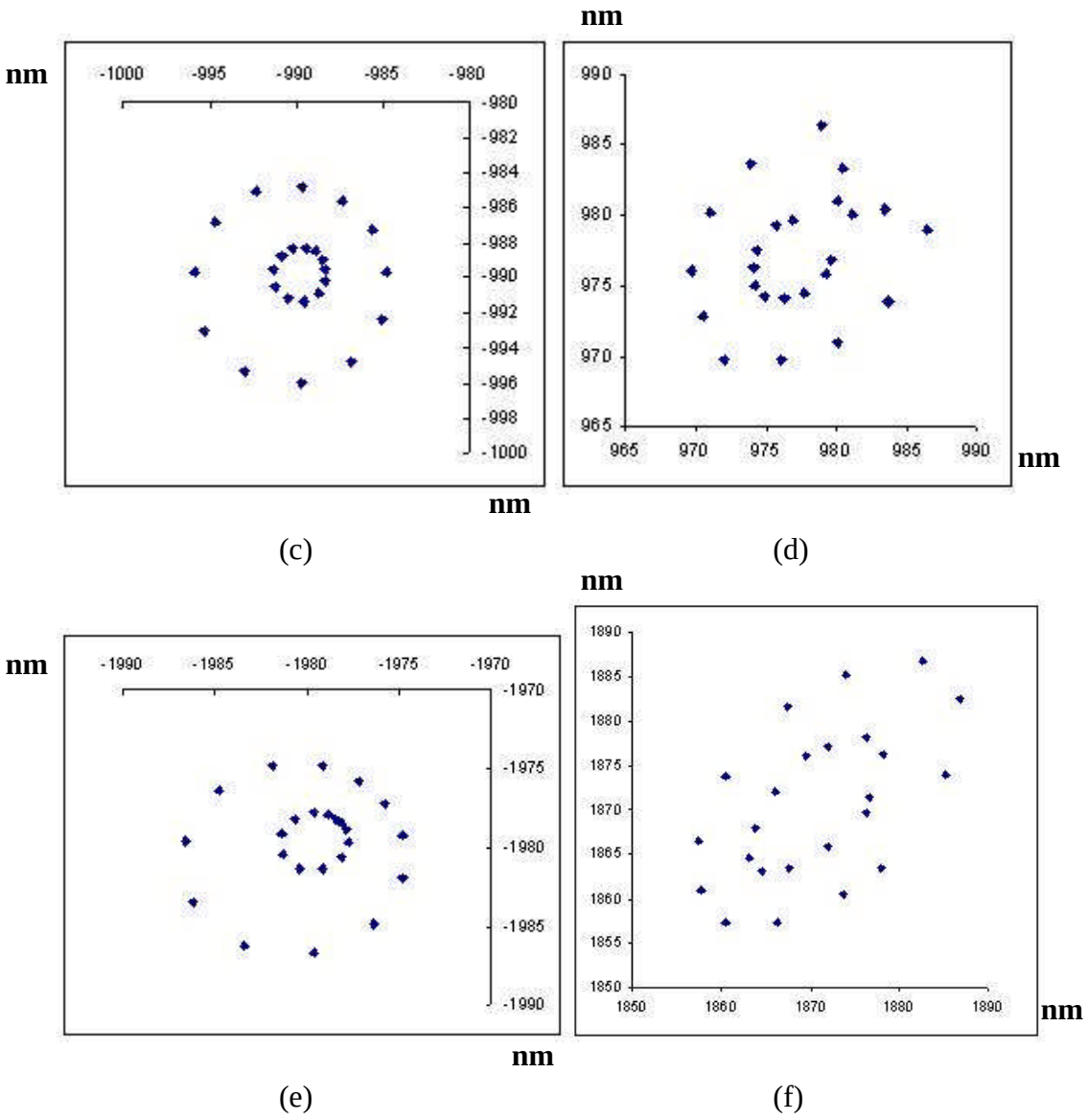

Figure 5.8: Spot diagrams of 0.5 eV off-axis electrons emitted from sample at different places for aperture diameter of 40 μm at the back focal plane.
(a) Emitted at (0.5 μm, 0.5 μm) before the drift tube
(b) Emitted at (0.5 μm, 0.5 μm) after the drift tube
(c) Emitted at (1 μm, 1 μm) before the drift tube
(d) Emitted at (1 μm, 1 μm) after the drift tube
(e) Emitted at (2 μm, 2 μm) before the drift tube
(f) Emitted at (2 μm, 2 μm) after the drift tube

Again all the spot diagrams consist of two rings. The outer ring represents all electrons that pass the contrast aperture at the back focal plane, while the inner ring

encloses 50% of the current, taken as a measure of the image resolution. Figures 5.8a and 5.8b show that the spot size before and after the drift tube are almost the same for 0.5 eV off-axis electrons leaving the sample surface at (0.5 μm , 0.5 μm), which means that the drift tube is predicted perform well at high resolution. For (1 μm , 1 μm) off-axis electrons, the spot size after the drift tube is about 1.5 times larger than the one before the drift tube, and for (2 μm , 2 μm), it is about 3 times larger. As expected, the further the emission point is off-axis, the greater the blur on the image will be. For off-axis electrons leaving sample surface at (5 μm , 5 μm), the spot position and diagrams before and after the drift tube are shown in Figure 5.9.

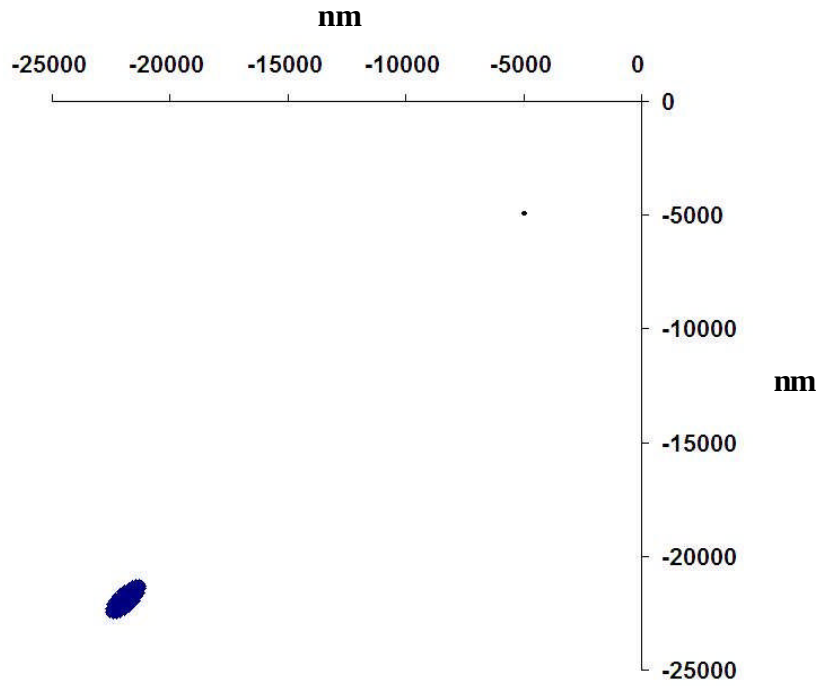

(a)

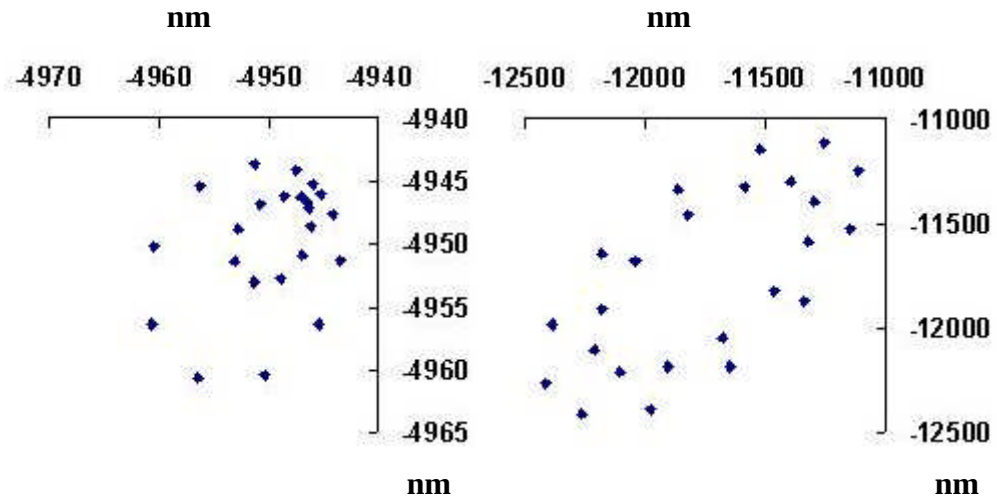

Figure 5.9: Spot diagrams of 0.5 eV off-axis electrons emitted from sample at (5 μm, 5 μm) for aperture diameter of 40 μm at the back focal plane.
(a) Spot positions before, which is the tiny spot at (-5000nm, -5000nm), and after the drift tube (the large spot)
(b) Spot diagram before the drift tube
(c) Spot diagram after the drift tube

Figure 5.9 clearly indicates that the predicted off-axis spot size grows significantly as the emission point goes up to (5 μm, 5 μm). This indicates that the drift-tube may add to the off-axis aberrations at low magnification mode. In order to understand the problem better, the trajectories for off-axis electrons are plot in Figure 5.10.

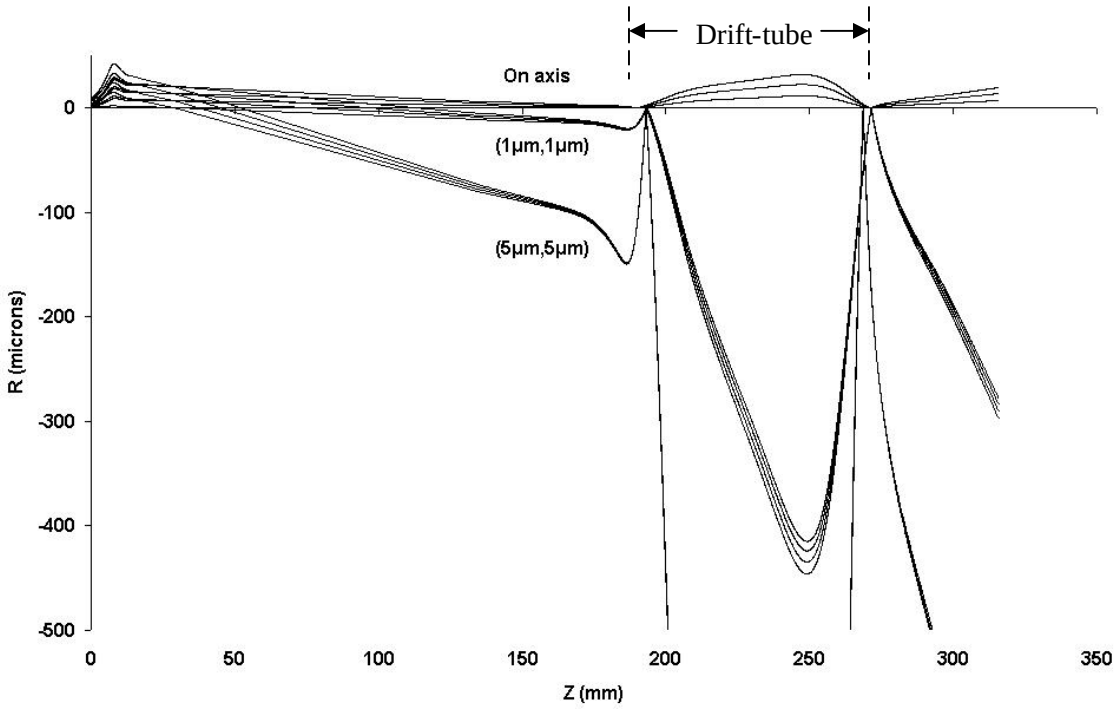

Figure 5.10: Trajectories for on-axis and off-axis electrons

Figure 5.10 shows that for off-axis electrons, there is a sharp focus at the entrance of the drift tube, which is induced by the strong electric field there. The situation is worse when the electrons go further off axis, will have large angles inside the drift tube, and therefore undergo higher aberration. One way to improve the design is to have a graded potential tube to weaken the electric field at the entrance of the drift tube. A new design is shown in Figure 5.11.

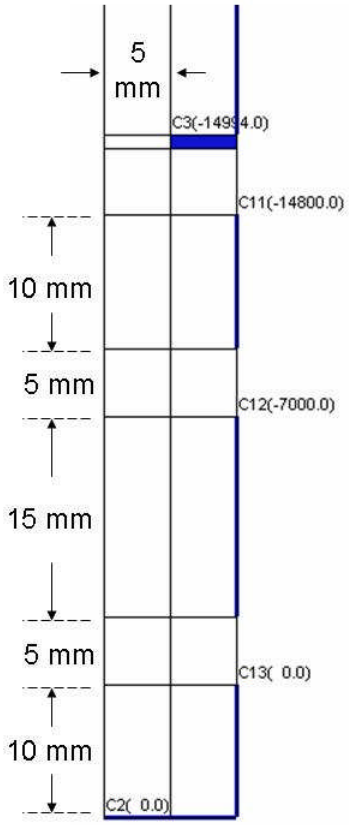

Figure 5.11: New design for drift tube to make the electric field weaker at the entrance of the drift tube

As shown in Figure 5.11, three extra electrodes are added in order to provide a graded potential before the drift tube: C11 (10 mm), C12 (15 mm) and C13 (10 mm). Each of these added electrodes are separated by a space of 5 mm. This design is intended to gradually ramp down the voltage over a longer distance, which will result in a weaker electric field at the drift tube entrance. The axial electric potential distribution is shown in Figure 5.12.

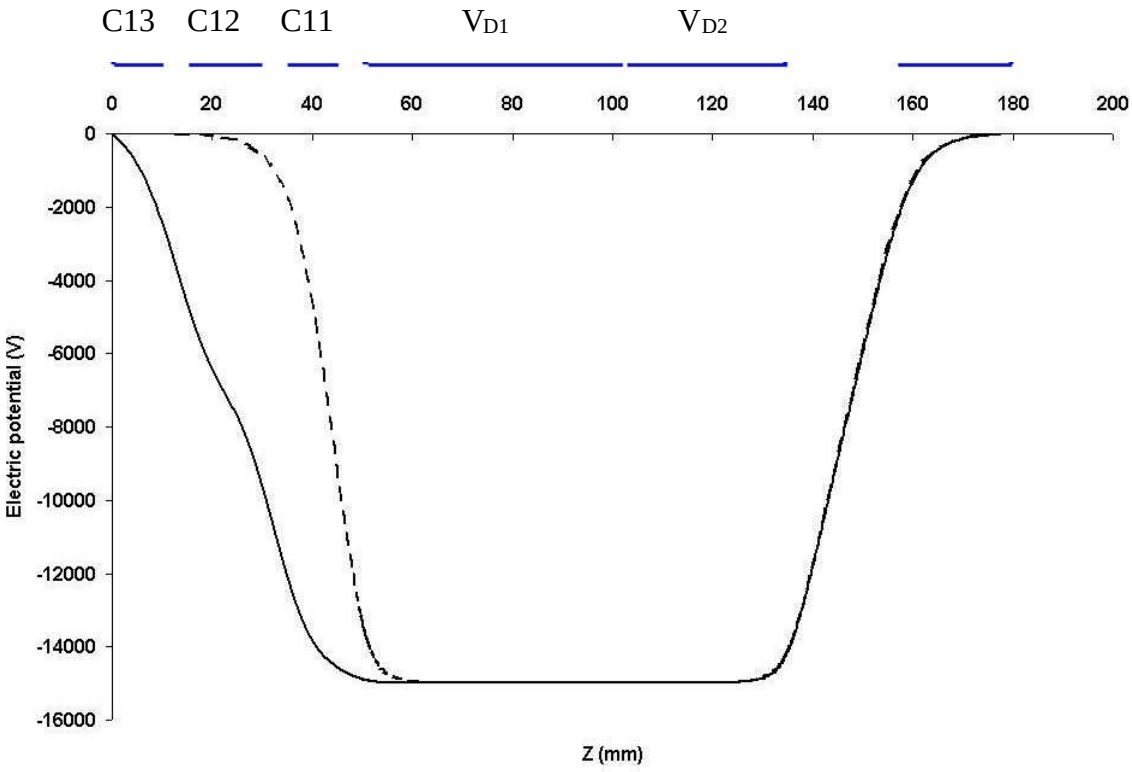

Figure 5.12: Axial electric potential distribution for the new drift tube design (solid line) and the old design (dotted line)

We can see from Figure 5.12 that the voltage drops over a longer distance as compared with the previous design. The new design has another advantage, in that it generates longer time dispersion for electrons with different energies. This in turn reduces the rate at which the correction voltage must be changed. The trajectories for 5 eV (5 μm, 5 μm) off-axis electrons for the new drift tube design are plotted in Figure 5.13.

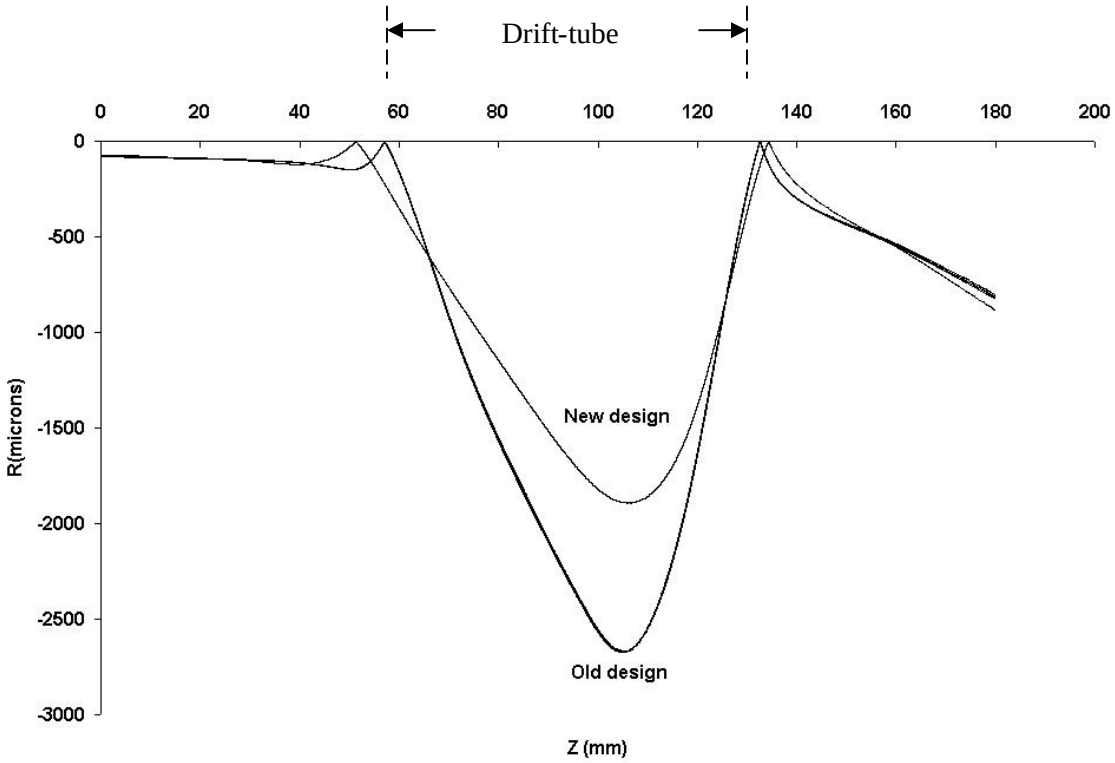

Figure 5.13: Trajectories of 5 eV (5 μm, 5 μm) off-axis electrons for both the new drift tube design and the old design.

Figure 5.13 shows that significant improvement has been achieved by reducing the electric field strength at the drift tube entrance; their angles are smaller and they travel closer to the axis. The spot diagram of the 5 eV (5 μm, 5 μm) off-axis electrons for the new drift tube design is shown in Figure 5.14.

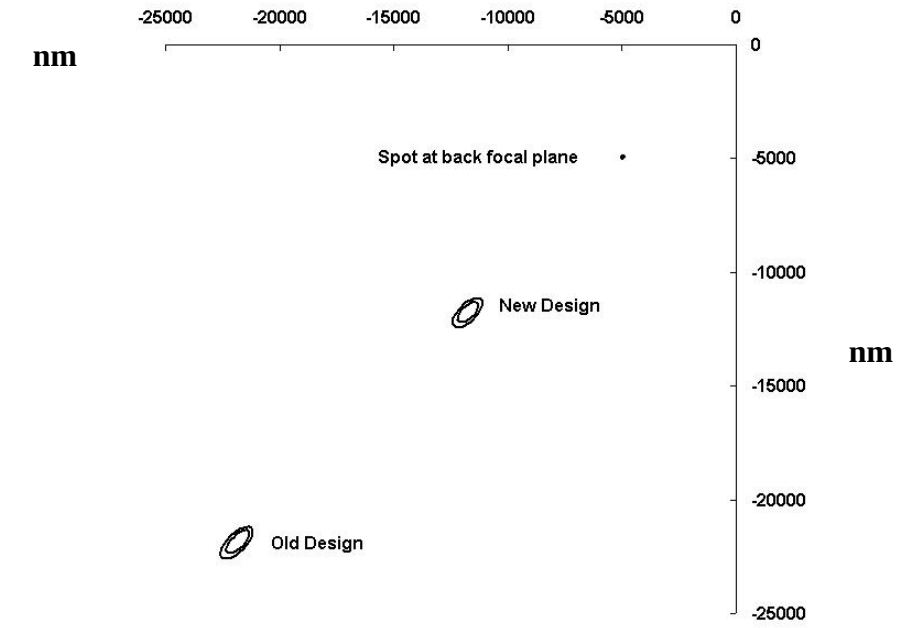

(a)

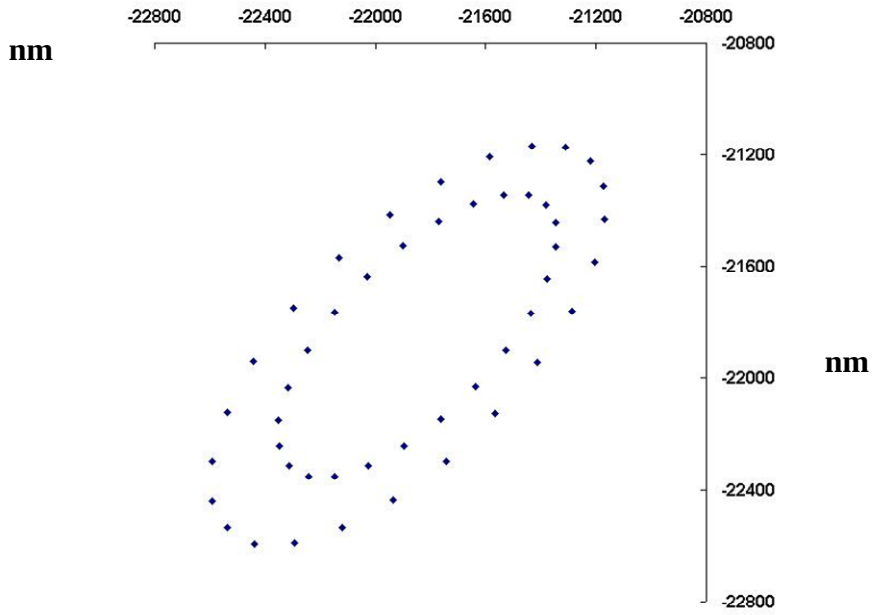

(b)

Figure 5.14: Spot diagram of the 5 eV (5 μm, 5 μm) off-axis electrons for the new drift tube design
(a) Spot positions before the drift tube and after the drift tube for both the new and old designs
(b) Spot diagram for the new drift tube design

Figure 5.14 shows that the predicted spot size is smaller for the new drift-tube design compared to the previous one shown in Figure 5.9c. But it is still too large in order to provide an acceptable resolution in low magnification mode. Some other change in the design have been tried, such as further reducing the potential of the electrode (C11) just before the drift tube (C3) to make the electric field strength even weaker, but the simulation results do not show much difference in reducing the spot size.

Since the drift tube design is predicted to perform well in the high resolution mode, a dual mode of operation can be proposed, where the drift-tube is switched on only for the high resolution mode. In the low magnification mode, the drift tube will not be turned on, and an area of interest will be identified using the electric objective lens only. When greater resolution is required, the drift tube will be turned on to correct for chromatic aberration dynamically. Some practical issues may still remain, such as column alignment of the drift tube with the electric objective lens.

CHAPTER 6

Conclusion and future work

A direct ray tracing program which employs the Cash-Karp 5^{th} order Runge-Kutta technique in combination with a Fourier-Series fit to electric/magnetic axial field distributions was developed and proven to be more accurate than the standard method of paraxial trajectory perturbation for the low energy electron optics simulations.

The performance of a mixed field objective lens for low landing energy SEM was examined. The simulation results showed that both the spherical and chromatic aberrations rise when the landing energy goes lower, which is different from those obtained by experiment on a low voltage portable SEM. Possible causes which led to the difference have been discussed.

Simulation of scattered secondary electron trajectory paths predicts that there will be considerable contrast of the low-energy spectrum at a detector plane above the objective lens due to surface specimen voltage or elemental variations. This has possible applications for quantitative material and voltage contrast.

The time-of-flight emission microscope (TOFEEM) was simulated and is expected to provide better image resolution than a conventional PEEM, predicting an improvement factor of approximately 7. The dynamic correction of chromatic aberration through

TOFEEM is expected to achieve a similar performance as that predicted for the tetrode mirror form of aberration correction, an image resolution of 4 nm at 2% transmission. The TOFEEM has the advantage of having a much simpler column design.

The design of a drift-tube for the purpose of dynamically correcting the chromatic aberration of a TOFEEM was presented. Simulations predict that the voltage of an electrode placed at the end of the drift-tube can be varied linearly in order to make the correction and that the final image resolution will be limited primarily by the spherical aberration of the objective lens. Simulation results showed that photoelectrons having emission energies up to 5 eV can be used to form the final image. The off-axis aberration performance was also simulated. Spot diagrams were calculated which show that the drift tube should perform well in high resolution mode, but suggest that further improvement for the drift tube design is needed for the low resolution mode. A dual magnification mode of operation has been proposed for the current drift tube design.

References

1. Tsuno, K., *Magnetic Lenses for Electron Microscopy*, in *Handbook of Charged Particle Optics*, J. Orloff, Editor. 1997, CRC Press LLC: Boca Raton, FL

2. Lencová, B., *Electrostatic Lenses*, in *Handbook of Charged Particle Optics*, J. Orloff, Editor. 1997, CRC Press LLC: Boca Raton, FL.

3. Khursheed, A., *Aberration characteristics of immersion lenses for LVSEM.* Ultramicroscopy, 2002. **93**(3-4): p. 331-8.

4. Munro, E., *Simulation of discrete Coulomb interactions in high-current projection and multi-beam columns.* Proceedings of SPIE - The International Society for Optical Engineering, 1999. **3777**: p. 215-227.

5. Khursheed, A. and M. Osterberg, *Developments in the design of a spectroscopic scanning electron microscope.* Nuclear Instruments & Methods in Physics Research Section a-Accelerators Spectrometers Detectors and Associated Equipment, 2006. **556**(2): p. 437-444.

6. Stohr, J. and S. Anders, *X-ray spectro-microscopy of complex materials and surfaces.* IBM Journal of Research and Development, 2000. **44**(4): p. 535-51.

7. Schonhense, G., et al. *Time-of-flight photoemission electron microscopy-a new way to chemical surface analysis.* 2001. Paris, France: Elsevier.

8. Schonhense, G. and H. Spiecker, *Correction of chromatic and spherical aberration in electron microscopy utilizing the time structure of pulsed excitation sources.* Journal of Vacuum Science & Technology B (Microelectronics and Nanometer Structures), 2002. **20**(6): p. 2526-34.

9. Khursheed, A., *A low voltage time of flight electron emission microscope.* Optik - International Journal for Light and Electron Optics, 2002. **113**(11): p. 505-509.

10. Hartel, P., et al., *Mirror corrector for low-voltage electron microscopes*, in *Advances in Imaging and Electron Physics, Vol 120.* 2002. p. 41-133.

11. Wan, W., et al. *Simulation of a mirror corrector for PEEM3.* 2004. Greenbelt, MD, USA: Elsevier.

12. Schmid, P., et al., *Correction and alignment strategies for the beam separator of the photoemission electron microscope 3 (PEEM3).* Review of Scientific Instruments, 2005. **76**(2): p. 23302-1.

13. Eric, M., et al. *Aberration analysis of wide-angle deflectors and lenses by direct ray tracing and comparison with conventional aberration theories.* 1995: SPIE.

14. Cash, J.R. and A.H. Karp, *A Variable Order Runge-Kutta Method for Initial-Value Problems with Rapidly Varying Right-Hand Sides.* Acm Transactions on Mathematical Software, 1990. **16**(3): p. 201-222.

15. William H. Press, S.A.T., William T. Vetterling, Brian P. Flannery, *Numerical Recipes in Fortran 77*. 2nd ed. 1999: Cambridge Univ. Press.

16. Yau, Y.W., et al., *Generation and applications of finely focused beams of low-energy electrons.* Journal of Vacuum Science and Technology, 1981. **19**(4): p. 1048-1052.

17. Khursheed, A., *KEOS*. 1995: Electrical Engineering Department, The National University of Singapore, 10 Kent Ridge Crescent, Singapore.

18. Khursheed, A., *The Finite Element Method in Charged Particle Optics*. 1999, Boston, USA: Kluwer Academic Publishers. Chapters 4, 7-9.

19. Herriot, J.G. and C.H. Reinsch, *Algorithm 600: translation of algorithm 507: procedures for quintic natural spline interpolation.* ACM Transactions on Mathematical Software, 1983. **9**(2): p. 258-9.

20. Khursheed, A., *The Finite Element Method in Charged Particle Optics.* 1999, Boston, USA: Kluwer Academic Publishers. 29-37.

21. Khursheed, A., K. Nelliyan, and Y. Ding, *Nanoscale imaging with a portable field emission scanning electron microscope.* Microelectronic Engineering, 2006. **83**(4-9): p. 762-766.

22. Chung, M.S. and T.E. Everhart, *Simple calculation of energy distribution of low-energy secondary electrons emitted from metals under electron bombardment.* Journal of Applied Physics, 1974. **45**(2): p. 707-9.

23. Khursheed, A., *A method of dynamic chromatic aberration correction in low-voltage scanning electron microscopes.* Ultramicroscopy, 2005. **103**(4): p. 255-260.

24. Glaser, W., *Rigorous calculation of magnetic lenses with a field form $H = H_0/[1+(z/a)^2]$.* Zeitschrift fur Physik, 1941. **117**(5-6): p. 285-315.

25. Batinic, M., D. Begert, and E. Kubalek, *Pulsed electron beam generation via laser stimulation.* Nuclear Instruments and Methods in Physics Research Section A: Accelerators, Spectrometers, Detectors and Associated Equipment, 1995. **363**(1-2): p. 43-47.

26. Khursheed, A., *Dynamic chromatic aberration correction in low energy electron microscopes.* Journal of Vacuum Science and Technology B: Microelectronics and Nanometer Structures, 2005. **23**(6): p. 2749-2753.

27. Barth, J.E. and P. Kruit, *Addition of different contributions to the charged particle probe size.* Optik (Jena), 1996. **101**(3): p. 101-109.

Appendices

Appendix A: 3D Cash Karp Runge-Kutta program

```
      OPTIONS(DREAL)
      winapp
      program TRAJCKRK
      include <windows.ins>

      PARAMETER (MAX=100000,EM=-1.7588012E11)
      REAL TOL,Sx,Sy,Sz,Vx,Vy,Vz,Xmin,Xmax,Ymin,
     * Ymax,Zmin,Zmax,X(MAX),Y(MAX),Z(MAX),E
      INTEGER NSTEP
      TOL=1.e-6
      Sx=0.
      Sy=0.
      Sz=0.
      E=5000
      Vx=0.
      Vy=-(abs(2*E*EM))**.5
      Vz=0.
      Xmin=-5.e-5
      Xmax=5.e-5
      Ymin=-5.e-5
      Ymax=5.e-5
      Zmin=-3.e-3
      Zmax=3.e-3
      CALL TRAJCK(TOL,Sx,Sy,Sz,Vx,Vy,Vz,NSTEP,Xmin,Xmax,Ymin,
     * Ymax,Zmin,Zmax,X,Y,Z)
      PRINT*,'Done!   No. of steps taken: ',NSTEP
      STOP
      END

      SUBROUTINE FLELEC(X,Y,Z,EX,EY,EZ)
C     For electric field, to be customized by user
C     Input : X,Y,Z
C     Output : EX,EY,EZ
      REAL X,Y,Z,EX,EY,EZ
      EX=0.
      EY=0.
      EZ=0.
      END

      SUBROUTINE FLMAG(X,Y,Z,BX,BY,BZ)
```

```
C     For magnetic field, to be customized by user
C     Input : X,Y,Z
C     Output : MX,MY,MZ
      REAL X,Y,Z,BX,BY,BZ
       IF(Y.Lt.3.e-5) THEN
       BX=0
       BY=0
       BZ=0.9
       ELSE
       BX=0
       BY=0
       BZ=0.
       ENDIF

      END

      SUBROUTINE TRAJCK(TOL,Sx,Sy,Sz,Vx,Vy,Vz,NSTEP,Xmin,Xmax,Ymin,
     * Ymax,Zmin,Zmax,X,Y,Z)
C     Cash Karp Runge Kutta Trajectory Integration

C     ***************** Input : ********************
C     TOL ---------- Tolerance in terms of nanometers (normally 1.E-6 nm)
C     Sx,Sy,Sz ----- Initial Position
C     Vx,Vy,Vz ----- Initial Velocity
C     Xmin,Xmax,Ymin,Ymax,Zmin,Zmax ----- Boundary for Ray Tracing

C     ***************** Output : ********************
C     NSTEP -------- Number of steps taken for ray tracing (integer)
C     X(NSTEP),Y(NSTEP),Z(NSTEP) -------- Coordinate for each point on the trajectory

      PARAMETER (MAX=100000,EM=-1.7588012E11)
      INTEGER NSTEP,nok,nbad
      REAL TOL,Sx,Sy,Sz,Vx,Vy,Vz,Xmin,Xmax,Ymin,Ymax,Zmin,Zmax,X(MAX),
     * Y(MAX),Z(MAX),yp(50,MAX),y0(3),v(3),V0,hmax
      EXTERNAL derivs,rkqs,derivs2
      y0(1)=Sx
      y0(2)=Sy
      y0(3)=Sz
      v(1)=Vx
      v(2)=Vy
      v(3)=Vz
C     INITIAL STEP SIZE
      IF(v(1).EQ.0.and.v(2).EQ.0.and.v(3).EQ.0.)THEN
      DT0=0.0001*(ABS(Zmax-Zmin)/(abs(2*(1.E10)*EM))**.5)
      ELSE
      V0=v(1)
```

```
      if(abs(V0).lt.abs(v(2)))Then
        V0=v(2)
        DT0=0.0001*(ABS(Ymax-Ymin)/ABS(V0))
      ENDIF
      if(abs(V0).lt.abs(v(3)))THEN
        V0=v(3)
        DT0=0.0001*(ABS(Zmax-Zmin)/ABS(V0))
      ENDIF
      if(V0.eq.v(1))DT0=0.0001*(ABS(Xmax-Xmin)/ABS(V0))
      ENDIF
C     MAXIMUM STEP SIZE ALLOWED
      hmax=100.*DT0
      CALL sodeint(y0,3,0.,20.,v,TOL,DT0,0.,nok,nbad,derivs
     * ,derivs2,rkqs,NSTEP,yp,Xmin,Xmax,Ymin,Ymax,Zmin,Zmax
     * ,hmax)
c     NSTEP=NSTEP-1
      OPEN(UNIT=9,FILE='TRAJCK.TXT')
      DO i=1,NSTEP
          X(i)=yp(1,i)
          Y(i)=yp(2,i)
          Z(i)=yp(3,i)
          WRITE(9,*)X(i),Y(i),Z(i)
      ENDDO
      WRITE(9,*)'  '
      return
      END


C     ******Second Order Differential Equation Intigration******
      SUBROUTINE sodeint(ystart,nvar,x1,x2,v,eps,h1,hmin,nok,nbad,
     * derivs,derivs2,rkqs,kount,yp,Xmin,Xmax,Ymin,Ymax,Zmin,Zmax
     * ,hmax)
      INTEGER nbad,nok,nvar,KMAXX,MAXSTP,NMAX
      REAL eps,h1,hmin,x1,x2,ystart(nvar),TINY,v(nvar),hmax
      EXTERNAL derivs,rkqs,derivs2
      PARAMETER (MAXSTP=100000,NMAX=50,KMAXX=100000,TINY=1.e-30)
      INTEGER i,kmax,kount,nstp
      REAL dxsav,h,hdid,hnext,x,xsav,dydx(NMAX),xp(KMAXX),y(NMAX),
     *
yp(NMAX,KMAXX),yscal(NMAX),a(NMAX),Xmin,Xmax,Ymin,Ymax,Zmin,Zmax
      x=x1
      h=sign(h1,x2-x1)
      nok=0
      nbad=0
      kount=0
      kmax=KMAXX
```

```
      do i=1,nvar
          y(i)=ystart(i)
          dydx(i)=v(i)
      enddo
      dxsav = 0.
      if (kmax.gt.0) xsav=x-2.*dxsav
      do nstp=1,MAXSTP
         call derivs2(y,dydx,a)
         do i=1,nvar
C             yscal(i)=abs(y(i))+abs(h*dydx(i))+TINY
             yscal(i)=1.E-9
         enddo
         if(kmax.gt.0)then
            if(abs(x-xsav).gt.abs(dxsav)) then
               if(kount.lt.kmax-1)then
                  kount=kount+1
                  xp(kount)=x
                  do i=1,nvar
                     yp(i,kount)=y(i)
C                      v(i)=dydx(i)
                  enddo
                  xsav=x
               endif
            endif
         endif
         if((x+h-x2)*(x+h-x1).gt.0.) h=x2-x
         call rkqs(y,dydx,a,nvar,x,h,eps,yscal,hdid,hnext,derivs
     * ,derivs2,hmax)
         if(hdid.eq.h)then
            nok=nok+1
         else
            nbad=nbad+1
         endif
         if(
     * (y(1)-Xmin)*(Xmax-y(1)).lt.0.
     * .OR.(y(2)-Ymin)*(Ymax-y(2)).lt.0.
     * .OR.(y(3)-Zmin)*(Zmax-y(3)).lt.0.
     * )THEN
            do i=1,nvar
               ystart(i)=y(i)
               v(i)=dydx(i)
            enddo
            if(kmax.ne.0)then
               kount=kount+1
               xp(kount)=x
               do i=1,nvar
```

```
                yp(i,kount)=y(i)
              enddo
            endif
            return
          endif
          if(abs(hnext).lt.hmin) pause
          h=hnext
        enddo
        pause
        return
        END

        SUBROUTINE derivs2(y,dydx,dydx2)
        REAL ELX,ELY,ELZ,BX,BY,BZ,EM
C       x:time(T),y:distance,dydx:velocity(V),dydx2:acceleration(a)
        REAL y(3),dydx(3),dydx2(3)
        PARAMETER (EM=-1.7588012E11)
C       ******Initialize the Field Values******
        ELX=0.
        ELY=0.
        ELZ=0.
        BX=0.
        BY=0.
        BZ=0.
        CALL FLELEC(y(1),y(2),y(3),ELX,ELY,ELZ)
        CALL FLMAG(y(1),y(2),y(3),BX,BY,BZ)
C       ******Acceleration******
        dydx2(1)=EM*(dydx(2)*BZ-dydx(3)*BY+ELX)
        dydx2(2)=EM*(dydx(3)*BX-dydx(1)*BZ+ELY)
        dydx2(3)=EM*(dydx(1)*BY-dydx(2)*BX+ELZ)
        END


        SUBROUTINE derivs(x,dydx,dydx2,v)
C       x:delta time(DT),v:initial velocity,dydx:velocity(V),dydx2:acceleration(a)
        REAL x,dydx(3),dydx2(3),v(3)
        do i=1,3
C         ******Velocity******
          dydx(i)=v(i)+dydx2(i)*x
        enddo
        END


c       ****** Runge Kutta Error Control Step******
        SUBROUTINE rkqs(y,dydx,a,n,x,htry,eps,yscal,hdid,hnext,derivs,
       * derivs2,hmax)
```

```
      INTEGER n,NMAX
      REAL eps,hdid,hnext,htry,x,dydx(n),a(n),y(n),yscal(n),hmax
      EXTERNAL derivs,derivs2
      PARAMETER (NMAX=50)
      INTEGER i
      REAL errmax,h,htemp,xnew,yerr(NMAX),dydxtemp(NMAX),ytemp(NMAX),
     * SAFETY,PGROW,PSHRNK,ERRCON
      PARAMETER (SAFETY=0.9,PGROW=-.2,PSHRNK=-.25,ERRCON=1.89e-4)
      h=htry
    1 call rkck(y,dydx,a,n,x,h,dydxtemp,ytemp,yerr,derivs,derivs2)
      errmax=0.
      do i=1,n
      errmax=max(errmax,abs(yerr(i)/yscal(i)))
      enddo
      errmax=errmax/eps
      if(errmax.gt.1.)then
        htemp=SAFETY*h*(errmax**PSHRNK)
        h=sign(max(abs(htemp),0.1*abs(h)),h)
        xnew=x+h
        if(xnew.eq.x)pause
        goto 1
      else
        if(errmax.gt.ERRCON)then
          hnext=SAFETY*h*(errmax**PGROW)
        else
          hnext=5.*h
        endif
        if(hnext.gt.hmax)hnext=hmax
        hdid=h
        x=x+h
        do i=1,n
          y(i)=ytemp(i)
          dydx(i)=dydxtemp(i)
        enddo
        return
      endif
      END

c     ******Cash Karp Runge Kutta******
      SUBROUTINE rkck(y,dydx,a,n,x,h,dydxout,yout,yerr,derivs,derivs2)
      INTEGER n,NMAX
      REAL h,x,a(n),dydx(n),y(n),yerr(n),yout(n),dydxout(n)
c     ,dydxerr(n)
      EXTERNAL derivs,derivs2
      PARAMETER (NMAX=50)
      INTEGER i
```

```
 REAL ak2(NMAX),ak3(NMAX),ak4(NMAX),ak5(NMAX),ak6(NMAX),
* ytemp(NMAX),A2,A3,A4,A5,A6,B21,B31,B32,B41,B42,B43,B51,
* B52,B53,B54,B61,B62,B63,B64,B65,C1,C3,C4,C6,DC1,DC3,
* DC4,DC5,DC6,aj2(NMAX),aj3(NMAX),aj4(NMAX),aj5(NMAX),aj6(NMAX),
* dydxtemp(NMAX)
 PARAMETER (A2=.2,A3=.3,A4=.6,A5=1.,A6=.875,B21=.2,B31=3./40.,
* B32=9./40.,B41=.3,B42=-.9,B43=1.2,B51=-11./54.,B52=2.5,
* B53=-70./27.,B54=35./27.,B61=1631./55296.,B62=175./512.,
* B63=575./13824.,B64=44275./110592.,B65=253./4096.,
* C1=37./378.,C3=250./621.,C4=125./594.,C6=512./1771.,
* DC1=C1-2825./27648.,DC3=C3-18575./48384.,
* DC4=C4-13525./55296.,DC5=-277./14336.,DC6=C6-.25)
 do i=1,n
     dydxtemp(i)=dydx(i)+B21*h*a(i)
     ytemp(i)=y(i)+B21*h*dydx(i)
 enddo
 call derivs2(ytemp,dydxtemp,aj2)
 call derivs(A2*h,ak2,a,dydx)
 do i=1,n
     dydxtemp(i)=dydx(i)+h*(B31*a(i)+B32*aj2(i))
     ytemp(i)=y(i)+h*(B31*dydx(i)+B32*ak2(i))
 enddo
 call derivs2(ytemp,dydxtemp,aj3)
 call derivs(A3*h,ak3,aj2,dydx)
 do i=1,n
     dydxtemp(i)=dydx(i)+h*(B41*a(i)+B42*aj2(i)+B43*aj3(i))
     ytemp(i)=y(i)+h*(B41*dydx(i)+B42*ak2(i)+B43*ak3(i))
 enddo
 call derivs2(ytemp,dydxtemp,aj4)
 call derivs(A4*h,ak4,aj3,dydx)
 do i=1,n
     dydxtemp(i)=dydx(i)+h*(B51*a(i)+B52*aj2(i)+B53*aj3(i)+
* B54*aj4(i))
     ytemp(i)=y(i)+h*(B51*dydx(i)+B52*ak2(i)+B53*ak3(i)+
* B54*ak4(i))
 enddo
 call derivs2(ytemp,dydxtemp,aj5)
 call derivs(h,ak5,aj4,dydx)
 do i=1,n
     dydxtemp(i)=dydx(i)+h*(B61*a(i)+B62*aj2(i)+B63*aj3(i)+
* B64*aj4(i)+B65*aj5(i))
     ytemp(i)=y(i)+h*(B61*dydx(i)+B62*ak2(i)+B63*ak3(i)+
* B64*ak4(i)+B65*ak5(i))
 enddo
 call derivs2(ytemp,dydxtemp,aj6)
 call derivs(A6*h,ak6,aj5,dydx)
```

```
      do i=1,n
          dydxout(i)=dydx(i)+h*(C1*a(i)+C3*aj3(i)+C4*aj4(i)+
     * C6*aj6(i))
          yout(i)=y(i)+h*(C1*dydx(i)+C3*ak3(i)+C4*ak4(i)+
     * C6*ak6(i))
      enddo
      do i=1,n
c          dydxerr(i)=h*(DC1*a(i)+DC3*aj3(i)+DC4*aj4(i)+DC5*aj5(i)
c     * +DC6*aj6(i))
          yerr(i)=h*(DC1*dydx(i)+DC3*ak3(i)+DC4*ak4(i)+DC5*ak5(i)
     * +DC6*ak6(i))
      enddo
      return
      END
```

Appendix B: Fourier series expansion for axial field distribution

```
      OPTIONS(DREAL)
      winapp
      program DRT
      include <windows.ins>

      CHARACTER*15 INNAME
      DOUBLE PRECISION INPUTX(10000),INPUTY(10000)
c     INTEGER M,N
      PARAMETER(M=2**15,N=128)
      REAL B(10000),C(10000),D(10000),E(10000), F(10000),a0,b0,yf(M)
     * ,F0(M),F1(M),F2(M),F3(M),F4(M),F5(M),F6(M),x(M),y(M)
     * ,F7(M)
      INTEGER STEP
      STEP=8000
      PRINT*, 'PLEASE INPUT THE AXIAL ELECTRICAL POTENTIAL FILE NAME'
      READ(*,*)INNAME
      OPEN(UNIT=99,FILE=INNAME)
      READ(99,*)NUMDATA
      DO  I=1,NUMDATA
      READ(99,*)INPUTX(I),INPUTY(I)
      ENDDO
      CALL boundary2(INPUTX,INPUTY,NUMDATA,a0,b0)
      OPEN(UNIT=96,FILE='Original.txt')
      DO I=1,NUMDATA
      WRITE(96,*)INPUTX(I),INPUTY(I)
      ENDDO
C     CALL boundary(INPUTY,NUMDATA,a0,b0)
      CALL QUINAT(NUMDATA, INPUTX, INPUTY, B, C, D, E, F)
      OPEN(UNIT=98,FILE='fit.txt')
      OPEN(UNIT=97,FILE='Fourier.txt')
c     M=2048
      h=(INPUTX(NUMDATA)-INPUTX(1))/M
      x(1)=INPUTX(1)
      DO I=1,M
        x(I)=x(1)+h*(I-1)
        CALL splint(INPUTX,INPUTY,B,C,D,E,F,NUMDATA,x(I),y(I))
        WRITE(98,*)x(I),y(I)
      ENDDO
      CLOSE(UNIT=98)
      CALL sinft(y,M)
c     CALL realft(y,2048,1)
c     CALL sinft(y,2048)
      PI=DACOS(-1.)
```

```
      DO I=1,M
        y(I)=y(I)*2/M
      ENDDO
c     N=1024
      h=(INPUTX(NUMDATA)-INPUTX(1))/STEP
      x(1)=INPUTX(1)
      DO I=1,STEP
        x(I)=x(1)+h*(I-1)
      ENDDO
      DO I=1,STEP
        yf(I)=0.
        DO J=1,N
        yf(I)=yf(I)+y(J+1)*sin((I-1)*PI*J/STEP)
        ENDDO
        F0(I)=yf(I)+a0*x(I)+b0
C************************
        yf(I)=0.
        DO J=1,N
        yf(I)=yf(I)+y(J+1)*cos((I-1)*PI*J/STEP)*(PI*J/(x(STEP)-x(1)))
        ENDDO
        F1(I)=yf(I)+a0
C************************
        yf(I)=0.
        DO J=1,N
        yf(I)=yf(I)-y(J+1)*sin((I-1)*PI*J/STEP)*(PI*J/(x(STEP)-x(1)))**2
        ENDDO
        F2(I)=yf(I)
C************************
        yf(I)=0.
        DO J=1,N
        yf(I)=yf(I)-y(J+1)*cos((I-1)*PI*J/STEP)*(PI*J/(x(STEP)-x(1)))**3
        ENDDO
        F3(I)=yf(I)
C************************
        yf(I)=0.
        DO J=1,N
        yf(I)=yf(I)+y(J+1)*sin((I-1)*PI*J/STEP)*(PI*J/(x(STEP)-x(1)))**4
        ENDDO
        F4(I)=yf(I)
C************************
        yf(I)=0.
        DO J=1,N
        yf(I)=yf(I)+y(J+1)*cos((I-1)*PI*J/STEP)*(PI*J/(x(STEP)-x(1)))**5
        ENDDO
        F5(I)=yf(I)
C************************
```

```
      yf(I)=0.
      DO J=1,N
      yf(I)=yf(I)-y(J+1)*sin((I-1)*PI*J/STEP)*(PI*J/(x(STEP)-x(1)))**6
      ENDDO
      F6(I)=yf(I)
C*************************
      yf(I)=0.
      DO J=1,N
      yf(I)=yf(I)-y(J+1)*cos((I-1)*PI*J/STEP)*(PI*J/(x(STEP)-x(1)))**7
      ENDDO
      F7(I)=yf(I)
C*********************************************************************
    ENDDO
    OPEN(UNIT=10,FILE='0.txt')
    DO I=1,STEP
    WRITE(10,*)x(I),F0(I)
    ENDDO
    OPEN(UNIT=11,FILE='1.txt')
    DO I=1,STEP
    WRITE(11,*)x(I),F1(I)
    ENDDO
    OPEN(UNIT=12,FILE='2.txt')
    DO I=1,STEP
    WRITE(12,*)x(I),F2(I)
    ENDDO
    OPEN(UNIT=13,FILE='3.txt')
    DO I=1,STEP
    WRITE(13,*)x(I),F3(I)
    ENDDO
    OPEN(UNIT=14,FILE='4.txt')
    DO I=1,STEP
    WRITE(14,*)x(I),F4(I)
    ENDDO
    OPEN(UNIT=15,FILE='5.txt')
    DO I=1,STEP
    WRITE(15,*)x(I),F5(I)
    ENDDO
    OPEN(UNIT=16,FILE='6.txt')
    DO I=1,STEP
    WRITE(16,*)x(I),F6(I)
    ENDDO
    OPEN(UNIT=17,FILE='7.txt')
    DO I=1,STEP
    WRITE(17,*)x(I),F7(I)
    ENDDO
    PRINT*,'Done!'
```

```
      STOP
      END

      SUBROUTINE boundary2(x,y,n,a,b)
      integer n
      real x(n),y(n),a,b
      a=(y(n)-y(1))/(x(n)-x(1))
      b=y(n)-a*x(n)
      DO I=1,n
        y(I)=y(I)-(a*x(I)+b)
      ENDDO
c     y(1)=0.
c     y(n)=0.
c     a=a*((x(n)-x(1))/n)
c     b=y(n)-a*n
      return
      end

      SUBROUTINE boundary(y,n,a,b)
      integer n
      real y(n),a,b
      a=(y(n)-y(1))/(n-1)
      b=y(n)-a*n
      DO I=1,n
        y(I)=y(I)-(a*I+b)
      ENDDO
c     y(1)=0.
c     y(n)=0.
      return
      end

      SUBROUTINE splint(xa,ya,B,C,D,E,F,n,x,y)
         INTEGER n
      REAL x,y,xa(n),B(n),C(n),D(n),E(n),F(n),ya(n)
      INTEGER k,khi,klo
      klo=1
      khi=n
1     if(khi-klo.gt.1)then
            k=(khi+klo)/2
        if(xa(k).gt.x)then
          khi=k
        else
          klo=k
        endif
      goto 1
      endif
```

```
      if((xa(khi)-xa(klo)).eq.0.)pause
      I=klo
      P = x - xa(I)
      y= ((((F(I)*P+E(I))*P+D(I))*P+C(I))*P+B(I))*P+ya(I)
         return
      end


      SUBROUTINE QUINAT(N, X, Y, B, C, D, E, F)                    QUI   10
C
      INTEGER N
      REAL X(N), Y(N), B(N), C(N), D(N), E(N), F(N)
C
C
C
C     QUINAT COMPUTES THE COEFFICIENTS OF A QUINTIC NATURAL
QUINTIC SPLI
C     S(X) WITH KNOTS X(I) INTERPOLATING THERE TO GIVEN FUNCTION
VALUES:
C             S(X(I)) = Y(I)  FOR I = 1,2, ..., N.
C     IN EACH INTERVAL (X(I),X(I+1)) THE SPLINE FUNCTION S(XX) IS A
C     POLYNOMIAL OF FIFTH DEGREE:
C     S(XX) = ((((F(I)*P+E(I))*P+D(I))*P+C(I))*P+B(I))*P+Y(I)    (*)
C           = ((((-F(I)*Q+E(I+1))*Q-D(I+1))*Q+C(I+1))*Q-B(I+1))*Q+Y(I+1)
C     WHERE  P = XX - X(I)  AND  Q = X(I+1) - XX.
C     (NOTE THE FIRST SUBSCRIPT IN THE SECOND EXPRESSION.)
C     THE DIFFERENT POLYNOMIALS ARE PIECED TOGETHER SO THAT S(X)
AND
C     ITS DERIVATIVES UP TO S"" ARE CONTINUOUS.
C
C       INPUT:
C
C     N         NUMBER OF DATA POINTS, (AT LEAST THREE, I.E. N > 2)
C     X(1:N)    THE STRICTLY INCREASING OR DECREASING SEQUENCE OF
C               KNOTS.  THE SPACING MUST BE SUCH THAT THE FIFTH POWER
C               OF X(I+1) - X(I) CAN BE FORMED WITHOUT OVERFLOW OR
C               UNDERFLOW OF EXPONENTS.
C     Y(1:N)    THE PRESCRIBED FUNCTION VALUES AT THE KNOTS.
C
C       OUTPUT:
C
C     B,C,D,E,F  THE COMPUTED SPLINE COEFFICIENTS AS IN (*).
C        (1:N)  SPECIFICALLY
C               B(I) = S'(X(I)), C(I) = S''(X(I))/2, D(I) = S'''(X(I))/6,
C               E(I) = S""(X(I))/24,  F(I) = S""(X(I))/120.
C               F(N) IS NEITHER USED NOR ALTERED.  THE FIVE ARRAYS
```

```
C              B,C,D,E,F MUST ALWAYS BE DISTINCT.
C
C       OPTION:
C
C     IT IS POSSIBLE TO SPECIFY VALUES FOR THE FIRST AND SECOND
C     DERIVATIVES OF THE SPLINE FUNCTION AT ARBITRARILY MANY
KNOTS.
C     THIS IS DONE BY RELAXING THE REQUIREMENT THAT THE SEQUENCE
OF
C     KNOTS BE STRICTLY INCREASING OR DECREASING.  SPECIFICALLY:
C
C     IF X(J) = X(J+1) THEN S(X(J)) = Y(J) AND S'(X(J)) = Y(J+1),
C     IF X(J) = X(J+1) = X(J+2) THEN IN ADDITION S''(X(J)) = Y(J+2).
C
C     NOTE THAT S'''(X) IS DISCONTINUOUS AT A DOUBLE KNOT AND, IN
C     ADDITION, S'''(X) IS DISCONTINUOUS AT A TRIPLE KNOT.  THE
C     SUBROUTINE ASSIGNS Y(I) TO Y(I+1) IN THESE CASES AND ALSO TO
C     Y(I+2) AT A TRIPLE KNOT.  THE REPRESENTATION (*) REMAINS
C     VALID IN EACH OPEN INTERVAL (X(I),X(I+1)).  AT A DOUBLE KNOT,
C     X(J) = X(J+1), THE OUTPUT COEFFICIENTS HAVE THE FOLLOWING
VALUES:
C       Y(J) = S(X(J))          = Y(J+1)
C       B(J) = S'(X(J))         = B(J+1)
C       C(J) = S''(X(J))/2      = C(J+1)
C       D(J) = S'''(X(J))/6     = D(J+1)
C       E(J) = S''''(X(J)-0)/24     E(J+1) = S''''(X(J)+0)/24
C       F(J) = S'''''(X(J)-0)/120   F(J+1) = S'''''(X(J)+0)/120
C     AT A TRIPLE KNOT, X(J) = X(J+1) = X(J+2), THE OUTPUT
C     COEFFICIENTS HAVE THE FOLLOWING VALUES:
C       Y(J) = S(X(J))          = Y(J+1)    = Y(J+2)
C       B(J) = S'(X(J))         = B(J+1)    = B(J+2)
C       C(J) = S''(X(J))/2      = C(J+1)    = C(J+2)
C       D(J) = S'''((X(J)-0)/6    D(J+1) = 0  D(J+2) = S'''(X(J)+0)/6
C       E(J) = S''''(X(J)-0)/24    E(J+1) = 0  E(J+2) = S''''(X(J)+0)/24
C       F(J) = S'''''(X(J)-0)/120  F(J+1) = 0  F(J+2) = S'''''(X(J)+0)/120
C
      INTEGER I, M
      REAL B1, P, PQ, PQQR, PR, P2, P3, Q, QR, Q2, Q3, R, R2, S, T, U, V
C
      IF (N.LE.2) GO TO 190
C
C     COEFFICIENTS OF A POSITIVE DEFINITE, PENTADIAGONAL MATRIX,
C     STORED IN D,E,F FROM 2 TO N-2.
C
      M = N - 2
      Q = X(2) - X(1)
```

```
      R = X(3) - X(2)
      Q2 = Q*Q
      R2 = R*R
      QR = Q + R
      D(1) = 0.
      E(1) = 0.
      D(2) = 0.
      IF (Q.NE.0.) D(2) = 6.*Q*Q2/(QR*QR)
C
      IF (M.LT.2) GO TO 40
      DO 30 I=2,M
        P = Q
        Q = R
        R = X(I+2) - X(I+1)
        P2 = Q2
        Q2 = R2
        R2 = R*R
        PQ = QR
        QR = Q + R
        IF (Q) 20, 10, 20
   10   D(I+1) = 0.
        E(I) = 0.
        F(I-1) = 0.
        GO TO 30
   20   Q3 = Q2*Q
        PR = P*R
        PQQR = PQ*QR
        D(I+1) = 6.*Q3/(QR*QR)
        D(I) = D(I) + (Q+Q)*(15.*PR*PR+(P+R)*Q*(20.*PR+7.*Q2)+Q2*(8.*
     *    (P2+R2)+21.*PR+Q2+Q2))/(PQQR*PQQR)
        D(I-1) = D(I-1) + 6.*Q3/(PQ*PQ)
        E(I) = Q2*(P*QR+3.*PQ*(QR+R+R))/(PQQR*QR)
        E(I-1) = E(I-1) + Q2*(R*PQ+3.*QR*(PQ+P+P))/(PQQR*PQ)
        F(I-1) = Q3/PQQR
   30 CONTINUE
C
   40 IF (R.NE.0.) D(M) = D(M) + 6.*R*R2/(QR*QR)
C
C     FIRST AND SECOND ORDER DIVIDED DIFFERENCES OF THE GIVEN
FUNCTION
C     VALUES, STORED IN B FROM 2 TO N AND IN C FROM 3 TO N
C     RESPECTIVELY. CARE IS TAKEN OF DOUBLE AND TRIPLE KNOTS.
C
      DO 60 I=2,N
        IF (X(I).NE.X(I-1)) GO TO 50
        B(I) = Y(I)
```

```
      Y(I) = Y(I-1)
      GO TO 60
   50   B(I) = (Y(I)-Y(I-1))/(X(I)-X(I-1))
   60 CONTINUE
     DO 80 I=3,N
      IF (X(I).NE.X(I-2)) GO TO 70
      C(I) = B(I)*0.5
      B(I) = B(I-1)
      GO TO 80
   70   C(I) = (B(I)-B(I-1))/(X(I)-X(I-2))
   80 CONTINUE
C
C     SOLVE THE LINEAR SYSTEM WITH C(I+2) - C(I+1) AS RIGHT-HAND SIDE.
C
     IF (M.LT.2) GO TO 100
     P = 0.
     C(1) = 0.
     E(M) = 0.
     F(1) = 0.
     F(M-1) = 0.
     F(M) = 0.
     C(2) = C(4) - C(3)
     D(2) = 1./D(2)
C
     IF (M.LT.3) GO TO 100
     DO 90 I=3,M
      Q = D(I-1)*E(I-1)
      D(I) = 1./(D(I)-P*F(I-2)-Q*E(I-1))
      E(I) = E(I) - Q*F(I-1)
      C(I) = C(I+2) - C(I+1) - P*C(I-2) - Q*C(I-1)
      P = D(I-1)*F(I-1)
   90 CONTINUE
C
  100 I = N - 1
     C(N-1) = 0.
     C(N) = 0.
     IF (N.LT.4) GO TO 120
     DO 110 M=4,N
C       I = N-2, ..., 2
      I = I - 1
      C(I) = (C(I)-E(I)*C(I+1)-F(I)*C(I+2))*D(I)
  110 CONTINUE
C
C     INTEGRATE THE THIRD DERIVATIVE OF S(X).
C
  120 M = N - 1
```

```
      Q = X(2) - X(1)
      R = X(3) - X(2)
      B1 = B(2)
      Q3 = Q*Q*Q
      QR = Q + R
      IF (QR) 140, 130, 140
  130 V = 0.
      T = 0.
      GO TO 150
  140 V = C(2)/QR
      T = V
  150 F(1) = 0.
      IF (Q.NE.0.) F(1) = V/Q
      DO 180 I=2,M
        P = Q
        Q = R
        R = 0.
        IF (I.NE.M) R = X(I+2) - X(I+1)
        P3 = Q3
        Q3 = Q*Q*Q
        PQ = QR
        QR = Q + R
        S = T
        T = 0.
        IF (QR.NE.0.) T = (C(I+1)-C(I))/QR
        U = V
        V = T - S
        IF (PQ) 170, 160, 170
  160   C(I) = C(I-1)
        D(I) = 0.
        E(I) = 0.
        F(I) = 0.
        GO TO 180
  170   F(I) = F(I-1)
        IF (Q.NE.0.) F(I) = V/Q
        E(I) = 5.*S
        D(I) = 10.*(C(I)-Q*S)
        C(I) = D(I)*(P-Q) + (B(I+1)-B(I)+(U-E(I))*P3-(V+E(I))*Q3)/PQ
        B(I) = (P*(B(I+1)-V*Q3)+Q*(B(I)-U*P3))/PQ -
     *   P*Q*(D(I)+E(I)*(Q-P))
  180 CONTINUE
C
C     END POINTS X(1) AND X(N).
C
      P = X(2) - X(1)
      S = F(1)*P*P*P
```

```
      E(1) = 0.
      D(1) = 0.
      C(1) = C(2) - 10.*S
      B(1) = B1 - (C(1)+S)*P
C
      Q = X(N) - X(N-1)
      T = F(N-1)*Q*Q*Q
      E(N) = 0.
      D(N) = 0.
      C(N) = C(N-1) + 10.*T
      B(N) = B(N) + (C(N)-T)*Q
  190 RETURN
      END


      SUBROUTINE sinft(y,n)
      INTEGER n
      REAL y(n)
C USES realft
c     Calculates the sine transform of a set of n real-valued data points stored in array
y(1:n).
c     The number n must be a power of 2. On exit y is replaced by its transform. This
program,
c     without changes, also calculates the inverse sine transform, but in this case the
output array
c     should be multiplied by 2/n.
      INTEGER j
      REAL sum,y1,y2
      DOUBLE PRECISION theta,wi,wpi,wpr,
     * wr,wtemp
c     Double precision in the trigonometric recurrences.
      theta=3.141592653589793d0/dble(n)
c     Initialize the recurrence.
      wr=1.0d0
      wi=0.0d0
      wpr=-2.0d0*sin(0.5d0*theta)**2
      wpi=sin(theta)
      y(1)=0.0
      do  j=1,n/2
      wtemp=wr
      wr=wr*wpr-wi*wpi+wr
c     Calculate the sine for the auxiliary array.
      wi=wi*wpr+wtemp*wpi+wi
c     The cosine is needed to continue the recurrence.
      y1=wi*(y(j+1)+y(n-j+1))
c     Construct the auxiliary array.
```

```
      y2=0.5*(y(j+1)-y(n-j+1))
      y(j+1)=y1+y2
c     Terms j and N . j are related.
      y(n-j+1)=y1-y2
      enddo
      call realft(y,n,+1)
c     Transform the auxiliary array.
      sum=0.0
      y(1)=0.5*y(1)
c     Initialize the sum used for odd terms below.
      y(2)=0.0
      do  j=1,n-1,2
      sum=sum+y(j)
      y(j)=y(j+1)
c     Even terms in the transform are determined directly.
      y(j+1)=sum
c     Odd terms are determined by this running sum.
      enddo
      return
      END

      SUBROUTINE realft(data,n,isign)
      INTEGER isign,n
      REAL data(n)
C USES four1
c     Calculates the Fourier transform of a set of n real-valued data points. Replaces this
data
c     (which is stored in array data(1:n)) by the positive frequency half of its complex
Fourier
c     transform. The real-valued first and last components of the complex transform are
returned
c     as elements data(1) and data(2), respectively. n must be a power of 2. This routine
c     also calculates the inverse transform of a complex data array if it is the transform of
real
c     data. (Result in this case must be multiplied by 2/n.)
      INTEGER i,i1,i2,i3,i4,n2p3
      REAL c1,c2,h1i,h1r,h2i,h2r,wis,wrs
      DOUBLE PRECISION theta,wi,wpi,wpr,
     * wr,wtemp
c     Double precision for the trigonometric recurrences.
      theta=3.141592653589793d0/dble(n/2)
c     Initialize the recurrence.
      c1=0.5
      if (isign.eq.1) then
      c2=-0.5
      call four1(data,n/2,+1)
```

```
c     The forward transform is here.
      else
      c2=0.5
c     Otherwise set up for an inverse transform.
      theta=-theta
      endif
      wpr=-2.0d0*sin(0.5d0*theta)**2
      wpi=sin(theta)
      wr=1.0d0+wpr
      wi=wpi
      n2p3=n+3
      do  i=2,n/4
c     Case i=1 done separately below.
      i1=2*i-1
      i2=i1+1
      i3=n2p3-i2
      i4=i3+1
      wrs=sngl(wr)
      wis=sngl(wi)
      h1r=c1*(data(i1)+data(i3))
c     The two separate transforms are separated out of
c     data.
      h1i=c1*(data(i2)-data(i4))
      h2r=-c2*(data(i2)+data(i4))
      h2i=c2*(data(i1)-data(i3))
      data(i1)=h1r+wrs*h2r-wis*h2i
c     Here they are recombined to form the true transform
c     of the original real data.
      data(i2)=h1i+wrs*h2i+wis*h2r
      data(i3)=h1r-wrs*h2r+wis*h2i
      data(i4)=-h1i+wrs*h2i+wis*h2r
      wtemp=wr
c     The recurrence.
      wr=wr*wpr-wi*wpi+wr
      wi=wi*wpr+wtemp*wpi+wi
      enddo
      if (isign.eq.1) then
      h1r=data(1)
      data(1)=h1r+data(2)
      data(2)=h1r-data(2)
c     Squeeze the first and last data together to get
c     them all within the original array.
      else
      h1r=data(1)
      data(1)=c1*(h1r+data(2))
      data(2)=c1*(h1r-data(2))
```

```
      call four1(data,n/2,-1)
c     This is the inverse transform for the case isign=-1.
      endif
      return
      END

      SUBROUTINE four1(data,nn,isign)
      INTEGER isign,nn
      REAL data(2*nn)
c     Replaces data(1:2*nn) by its discrete Fourier transform, if isign is input as 1; or
replaces
c     data(1:2*nn) by nn times its inverse discrete Fourier transform, if isign is input as .1.
c     data is a complex array of length nn or, equivalently, a real array of length 2*nn. nn
c     MUST be an integer power of 2 (this is not checked for!).
      INTEGER i,istep,j,m,mmax,n
      REAL tempi,tempr
      DOUBLE PRECISION theta,wi,wpi,wpr,wr,wtemp
c     Double precision for the trigonometric
c     recurrences.
      n=2*nn
      j=1
      do  i=1,n,2
c     This is the bit-reversal section of the routine.
      if(j.gt.i)then
      tempr=data(j)
c     Exchange the two complex numbers.
      tempi=data(j+1)
      data(j)=data(i)
      data(j+1)=data(i+1)
      data(i)=tempr
      data(i+1)=tempi
      endif
      m=nn
1     if ((m.ge.2).and.(j.gt.m)) then
      j=j-m
      m=m/2
      goto 1
      endif
      j=j+m
      enddo
      mmax=2
c     Here begins the Danielson-Lanczos section of the routine.
2     if (n.gt.mmax) then
c     Outer loop executed log2 nn times.
      istep=2*mmax
      theta=6.28318530717959d0/(isign*mmax)
```

```
c     Initialize for the trigonometric recurrence.
      wpr=-2.d0*sin(0.5d0*theta)**2
      wpi=sin(theta)
      wr=1.d0
      wi=0.d0
      do  m=1,mmax,2
c     Here are the two nested inner loops.
      do  i=m,n,istep
      j=i+mmax
c     This is the Danielson-Lanczos formula:
      tempr=sngl(wr)*data(j)-sngl(wi)*data(j+1)
      tempi=sngl(wr)*data(j+1)+sngl(wi)*data(j)
      data(j)=data(i)-tempr
      data(j+1)=data(i+1)-tempi
      data(i)=data(i)+tempr
      data(i+1)=data(i+1)+tempi
      enddo
      wtemp=wr
c     Trigonometric recurrence.
      wr=wr*wpr-wi*wpi+wr
      wi=wi*wpr+wtemp*wpi+wi
      enddo
      mmax=istep
      goto 2
c     Not yet done.
      endif
c     All done.
      return
      END
```

Publication list

Journal Papers

1. A. Khursheed, K. Nellilyan and **Y. Ding**, "Nanoscale imaging with a portable field emission scanning electron microscope", *Microelectronic Engineering* **83**, pp 762-766**,** 2006

Conference Papers

2. A. Khursheed and **D. Yu**, "Simulation of a time-of-flight electron emission microscope (TOFEEM)", Seventh International Conference on Charged Particle Optics, CPO-7, Trinity College, Cambridge, England, July 25th-28th, 2006

3. A. Khursheed and **D. Yu**, "Simulated performance of a time-of-flight electron emission microscope", edited by I. Mullerova, pp 39-40, Brno, Czech Republic: Institute of Scientific Instruments, Academy of Sciences of the Czech Republic, July 2006. Paper presented at the: 10th seminar on the Recent Trends in Charged Particle Optics and Surface Physics Instrumentation, July 2006, Skalsky, Brno, Czech Republic.

Available online at www.sciencedirect.com
SCIENCE DIRECT®
Microelectronic Engineering 83 (2006) 762–766
MICROELECTRONIC ENGINEERING
www.elsevier.com/locate/mee

Nanoscale imaging with a portable field emission scanning electron microscope

Anjam Khursheed [a,*], Karuppiah Nelliyan [b], Yu Ding [a]

[a] National University of Singapore, Department of Electrical and Computer Engineering, 4 Engineering Drive 3, Singapore 117576, Singapore
[b] Mini Electron Beam Instruments, 247A Pasir Panjang Road, Singapore 118607, Singapore

Available online 2 February 2006

Abstract

Secondary electron images at low landing energies (below 50 eV) are presented by a portable field emission scanning electron microscope. The results show that nanoscale images of resolution better than 20 nm can be obtained on a nylon-fibre specimen at landing energies as low as 1 eV. Preliminary simulation results predict that the image resolution should be much higher.

Keywords: Immersion electron lens; SEM; Landing energy

1. Introduction

This paper examines the performance of a portable field emission SEM operating at low landing energies (<50 eV). The MEBI-DELONG FMS100 FEG Mini SEM was developed at the National University of Singapore in collaboration with Delong Instruments and is now commercialized through the company MEBI, Mini Electron Beam Instruments [1]. The MEBI-DELONG FMS100 SEM is designed to achieve nanoscale image resolution at low landing energies, while at the same time being mobile. The entire SEM system, including turbo and ion pumps, supply and control electronics, computer and monitor, is fitted on to a small trolley. The trolley can be wheeled through narrow doorways, placed into small elevators, and rolled on to a mini-van. The advantages of having a high resolution SEM mobile are numerous: it can be used out in the field, for say early virus detection or geological mineral identification, or moved from floor to floor within a semi-conductor fabrication plant. Fig. 1 shows that the MEBI-DELONG FMS100 SEM column is comparable in size to its 17 in. LCD display monitor. Fig. 2 depicts a projection drawing of the Mini FEG SEM mounted on its trolley, measuring 60 by 80 by 80 cm.

A schematic drawing of the MEBI-DELONG FMS100 portable SEM is shown in Fig. 3. It uses a permanent magnet objective lens and an electromagnet condenser lens that is integrated into a Schottky field emission gun unit. The gun assembly, including ion pumps, is miniaturized. A motor driven aperture can be automatically aligned and provides aperture diameters of 50, 75 and 100 μm. A miniature 2 stage electrostatic octupole unit provides scanning of the primary beam as well acts as a stigmator. A miniature scintillator detector/PMT tube, and BSE detector are placed below the movable aperture unit.

The objective lens unit, contains the specimen chamber and specimen stage, and is detachable from the rest of the chamber, as shown in Fig. 4. The top plate of the objective lens (upper pole piece) is removed in order to replace the specimen. The objective lens uses a combined electric retarding field and magnetic immersion action, which gives the highest possible image resolution possible without aberration correction [2].

The maximum primary beam voltage of the FMS100 portable SEM is 6 kV, while the specimen can be biased to −6 kV in fine steps. Coarse focusing is achieved through moving the specimen height, while fine focusing adjustments are made via varying the condenser lens coil current.

* Corresponding author. Tel.: +65 68742295/67798415; fax: +65 67791103.
E-mail address: eleka@nus.edu.sg (A. Khursheed).

0167-9317/$ - see front matter © 2006 Elsevier B.V. All rights reserved.
doi:10.1016/j.mee.2006.01.003

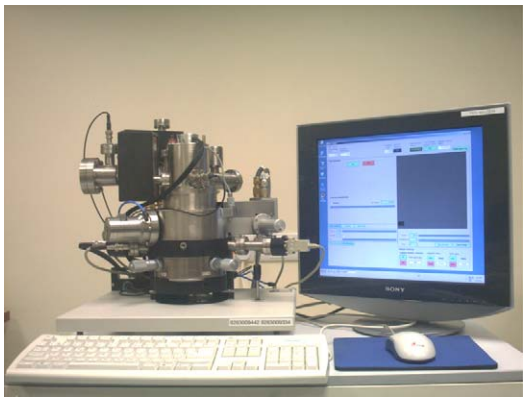

Fig. 1. Photograph of MEBI-DELONG FMS100 Mini SEM column and its 17 in. LCD monitor.

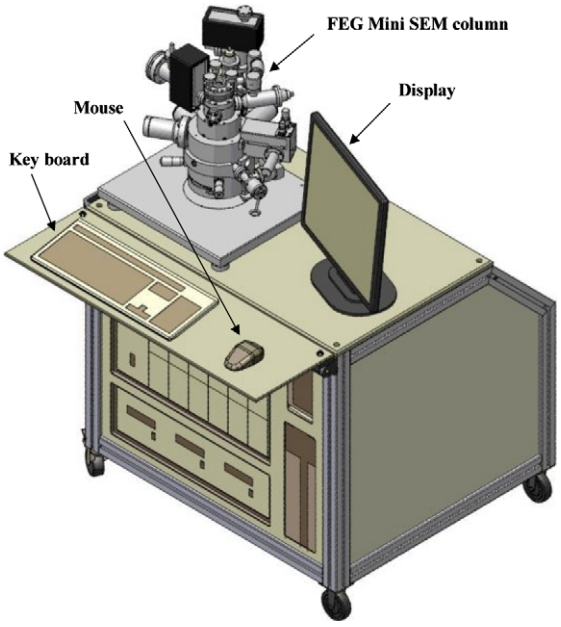

Fig. 2. Projection drawing of the MEBI-DELONG FMS100 Mini SEM on its trolley measuring $60 \times 80 \times 80$ cm.

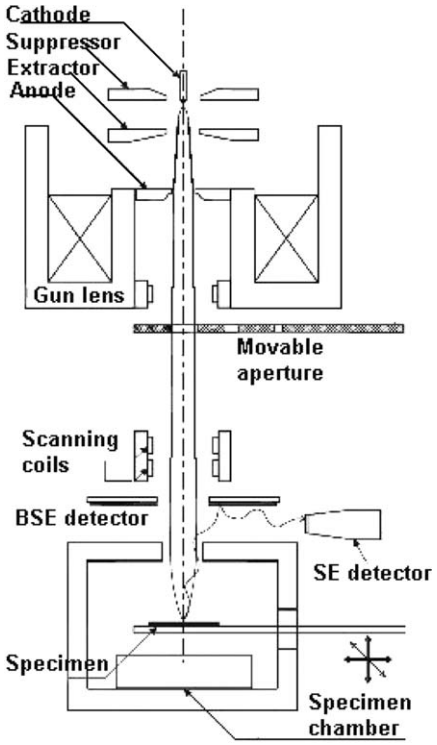

Fig. 3. Schematic drawing of the MEBI-DELONG FMS100 Mini SEM column.

Fig. 4. The detachable specimen chamber/stage/objective lens unit with the top plate (upper pole piece) removed.

In order to achieve high resolution, it is critical to move the specimen to an optimum position, this position is given in the software display window.

2. Experimental images at moderate landing energies

Secondary electron images for different nanostructure samples at moderate beam landing energies are shown in Fig. 5. These images show that the portable FSM100 is capable of obtaining nanoscale resolution for different types of samples, including con-conductive ones. Fig. 6 shows a performance comparison of the portable FSM100 SEM at low landing voltages with a conventional Field Emission SEM (Philips XL 30) using a sample composed of 500 nm polystyrene spheres. The results are taken for a landing energy of 1 keV and 700 eV, while leaving the specimen biased to -5 kV. As seen from these figures, the portable SEM lens provides sharper pictures at these landing energies, and indicates much more surface detail on the nanospheres. At higher beam landing energies in a conventional SEM, images of this specimen suffer from severe charging problems.

3. Experimental images at ultra-low landing energies

Fig. 7 shows secondary electron images of nylon fibres (ranging from 50 to 300 nm in diameter) taken at very low landing energies. The landing energy is reduced from 50 to 1 eV, through to mirror mode. The beam energy is kept at 6 keV and the specimen voltage is varied for positive landing energies, while in mirror mode, the specimen

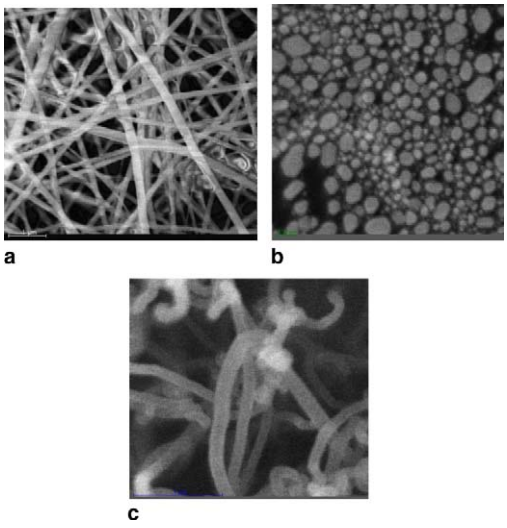

Fig. 5. FSM100 SEM secondary images at moderate beam landing energies: (a) nylon nanofibres measuring 50–300 nm at 6 keV; (b) gold particles of 100 nm or smaller at 3.6 keV; (c) carbon nanotubes of 100 nm diameter at 5.6 keV.

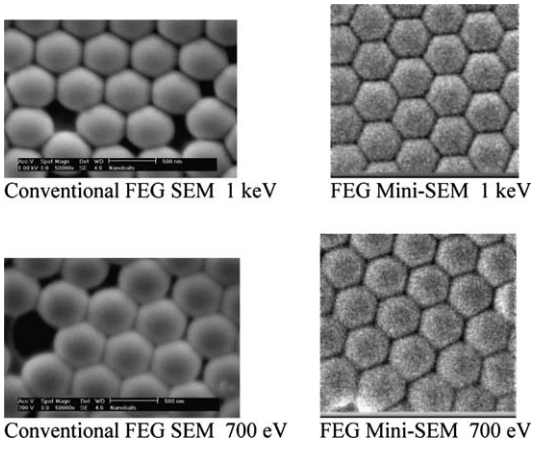

Fig. 6. Comparison of conventional FEG SEM SE images with Mini FSM100 SEM at landing energies of 1 keV and 700 eV on 500 nm polystyrene nanospheres.

voltage is fixed at −6 kV, and the primary beam voltage is varied. The image sharpness is of course, better for higher landing energies. The significant feature of these results is that the image resolution for such ultra-low landing energies is relatively high, typically around 20 nm or less. Note also, that non-uniform brightness in the image occurs as mirror mode is approached. This can obviously be explained by the fact the SE detector lies off-axis.

Confirmation that relatively high resolution can be obtained at very low landing energies is shown in Fig. 8. Here, a secondary electron image of the nylon-fibre specimen is taken at a higher magnification, shown in Fig. 8a, and a line-scan is made across it, so that the signal edge rise across a fibre can be measured. The 25–75% rise gives an approximate estimate of the resolution. As shown in Fig. 8b, the resolution is approximately 16 nm.

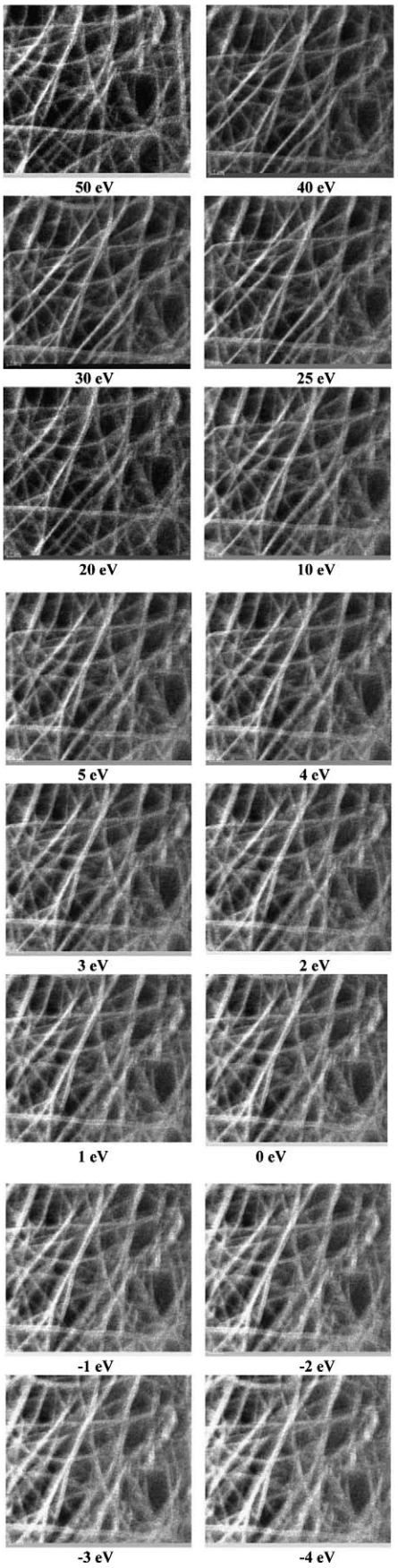

Fig. 7. Images of nylon nanofibres (50–300 nm diameter) with low landing energies. The negative energies represent mirror mode.

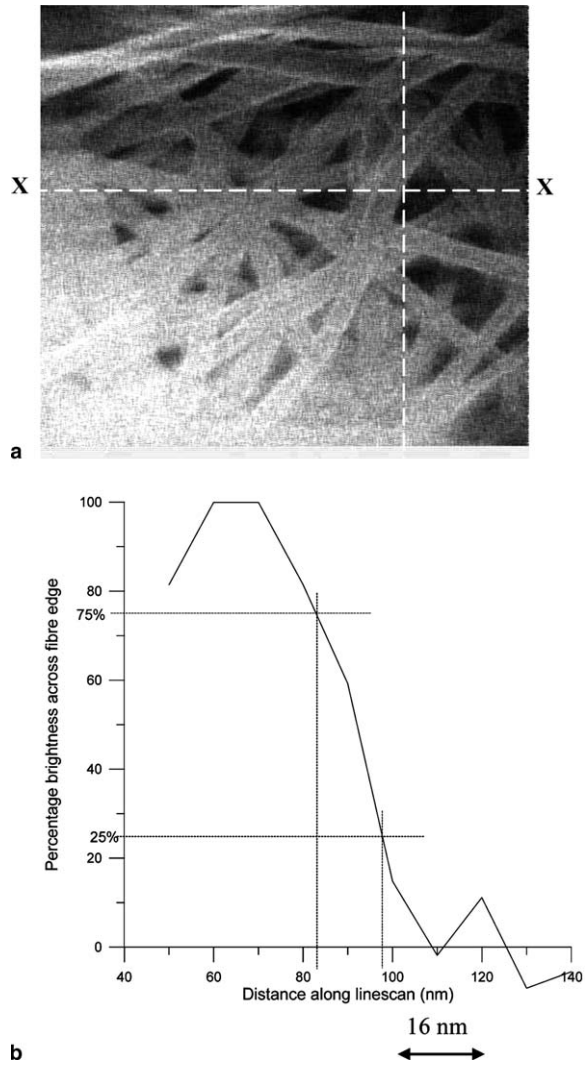

Fig. 8. Resolution estimate at 1 eV landing energy: (a) image indicating line-scan X–X; (b) graph of line-scan giving a resolution estimate of 16 nm.

4. Simulation of objective lens

To gain a better understanding of the very low landing energy experimental results, simulations of the objective lens were carried out. Finite element programs were used to calculate the axial potential and magnetic field distributions of the lens, while direct ray tracing of the primary beam provided an estimate of the probe radius at the specimen due to chromatic and spherical aberration. The finite element programs were written by the author [3]. Direct ray tracing employed the Cash–Karp 5th-order Runge–Kutta technique in combination with a Fourier fit to the axial field distribution so that smooth higher derivatives could be calculated in a series expansion method to obtain off-axis field values [4]. The simulated axial potential and magnetic field distribution above the specimen is shown in Fig. 9. The graph depicts a 6 keV primary beam being decelerated down to an energy of 50 eV at the specimen.

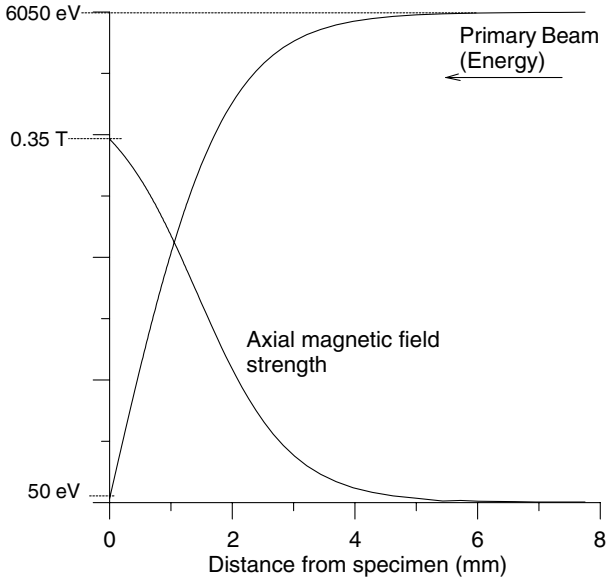

Fig. 9. Simulated axial potential and magnetic field distributions for the objective lens.

Only parallel rays were simulated. The magnetic field strength was automatically scaled to focus the primary beam on to the specimen for different landing energies. At a primary beam energy of 6 keV, shifts of the focal position between landing energies of 1–50 eV were relatively small, and roughly equivalent to the kind of small specimen height adjustments used to achieve focusing of the permanent magnet lens in practice. The aperture radius was varied up to 25 μm, and the beam energy spread of 0.5 eV was assumed (corresponding to a Schottky field emitter source). In order to estimate the on-axis third-order spherical aberration coefficient, C_s, 10 parallel trajectories were plot for radii varying up to 2.5 μm, and the subsequent focal positions and image semi-angles were noted. To estimate the on-axis chromatic aberration coefficient, C_c, different initial energies were used. Fig. 10 shows the variation of the

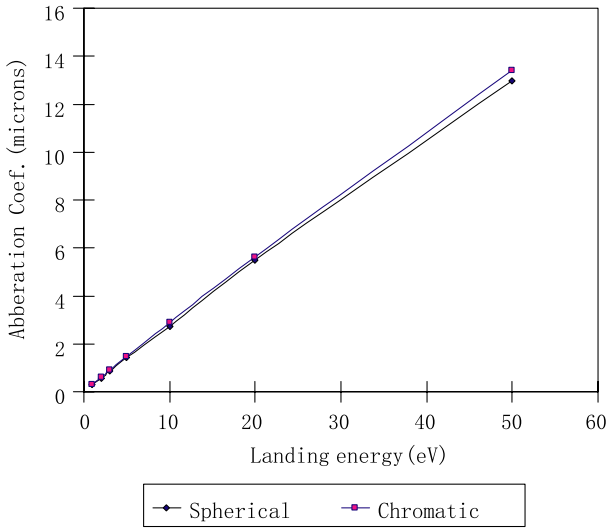

Fig. 10. Variation of on-axis aberration coefficients with landing energy.

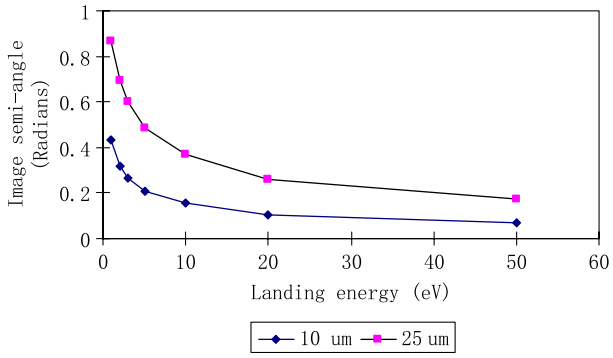

Fig. 11. Simulated variation of image semi-angle with landing energy.

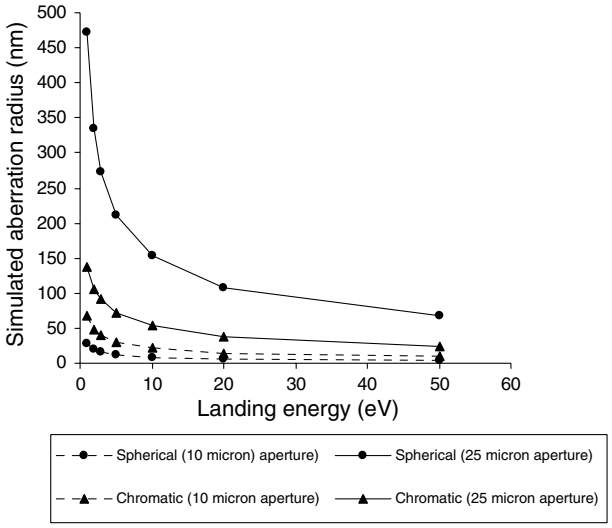

Fig. 12. Simulated aberration radius at the specimen as a function of landing energy.

simulated on-axis aberration coefficients with landing energy. As a cross-check on these values, they were compared with the standard method of paraxial trajectory perturbation for 10, 20 and 50 eV landing energies. The values agreed to within 4% for 50 eV, and around 10% for 20 and 10 eV.

Fig. 10 shows that C_c and C_s fall linearly with landing energy and are approximately the same magnitude. In addition to this variation, it is important to analyze the increase in image semi-angle, which rises sharply as the landing energy decreases. This variation is depicted in Fig. 11 for aperture radii 10 and 25 μm. The large non-linear rise in semi-angle also clearly indicates why direct ray tracing is more suited to analyzing the objective lens characteristics for very low landing energies, as opposed to using paraxial trajectories, which are only valid for relatively small apertures (less than 2.5 μm).

Despite the falling aberration coefficients trend shown in Fig. 10, the sharp rise in semi-angle, over 45° at 1 eV for the 25 μm aperture, naturally leads to a rise in the effect of spherical aberration on the image probe size. The chromatic aberration effect is also expected to increase, since in addition to the rise in image semi-angle, the relative energy spread also increases. These effects can be seen in the simulated aberration radii shown in Fig. 12, calculated for 10 and 25 μm apertures. The spherical aberration spot clearly rises more steeply than the chromatic one, and there is a significant improvement as the aperture size is decreased.

The aberration predictions on the final probe size shown in Fig. 12, are significantly higher than the experimental resolution results, which were under 20 nm for a 1 eV landing energy. There are several important factors that may account for this difference. Firstly, the correct effect of a given aperture size can only be made when the source position, as well as the effect of the gun lens is taken into account. The gun lens magnetic field is likely to collimate the electrons, effectively shifting the current distribution closer to the axis, this means the effect of the aperture in the present simulations may be overestimated. Secondly, the nylon specimen used for resolution estimates may have been charging positively. Thirdly, electron–electron interaction effects may become significant as the primary beam slows down to very low energies above the specimen, these effects may reduce the image semi-angle in practice. Fourthly, the relatively poor vacuum in the SEM specimen chamber, typically between 10^{-6} and 10^{-5} Torr, means that there will be a carbon layer deposited on the specimen surface and ions will also be generated near the surface, these effects are also likely to reduce the final image semi-angle.

In the present context, it is sufficient to note that the experimental resolution estimate is much better than that predicted by simulation, and that there is thus much more analysis required to adequately understand secondary image formation at very low landing energies by a field emission SEM.

Acknowledgments

The authors thank Vladimir Kolarik and Robert Kolarik of Delong Instruments, Brno, Czech Republic, for their support and collaboration.

References

[1] Mini Electron Beam Instruments (MEBI), 247A Pasir Panjang Road, Chuville, Singapore 118607.
[2] A. Khursheed, Aberration characteristics of immersion lenses for LVSEM, Ultramicroscopy 93 (2002) 331–338.
[3] A. Khursheed, The Finite Element Method in Charged Particle Optics, Kluwer Academic Publishers, Boston, USA, 1999 (Chapters 4, 7–9).
[4] E. Munro, Simulation of discrete coulomb interactions in high-current projection and multi-beam columns, in: Charged Particle Optics IV, Proceedings of SPE 1999, vol. 3777, pp. 215–227.